ABSTRACT

Title of Dissertation:	ENERGY TRANSFER DYNAMICS OF HIGH ENERGY MOLECULES
	Christopher R. Lukowski, Doctor of Philosophy, 2023
Dissertation directed by:	Professor Amy S. Mullin, Department of Chemistry and Biochemistry

This dissertation investigates the energy transfer dynamics of high-energy molecules excited electronically, vibrationally, and rotationally. The molecules studied in this thesis were excited electronically and vibrationally with UV photon absorption and rotationally with an optical centrifuge. The excited molecules are relaxed either by collisions or a chemical process. The products of the relaxation process are measured using high-resolution transient IR absorption spectroscopy to determine the state-resolved products and the energy partitioning.

In the first study the collisional relaxation of highly vibrationally excited collidine with bath CO_2 is investigated. The collidine was excited to an E_{vib}=38,552 cm^{-1} after absorption of a λ=266 nm photon and the full state-resolved distribution of the scattered CO_2 is reported. The results are compared to previous studies done on methylated pyridines. The translational energy and rotational energy gain of the scattered CO_2 is similar for the methylated pyridines, however, the integrated appearance rate constant for collidine-CO_2 collisions is higher then the other

methylated pyridine molecules. The effect that the donor complexity has on collisional relaxation is explored.

For the second study, SO_2 is electronically excited to the predissociative metastable $\tilde{C}$ electronic state. The SO product quantum yields, rotational distributions, and product energy partitioning show that translational energy is preferred by a 4:1 ratio over rotational energy for the photoproducts. The preference for translational energy is evidence that a linear transition state could be involved in the dissociation process. Theoretical calculations of the SO_2 potential energy surfaces for the ground state and the excited state show that for SO_2 photodissociation to occur near the dissociation threshold the SO_2 in the $\tilde{C}$ state becomes linear and that coupling to the repulsive triplet state lowers the height of the energy barrier so dissociation can proceed.

The third study used a tunable optical centrifuge to rotationally excite N_2O into extreme rotational states. The optical centrifuge was tuned to selectively populate rotational states between J=100-200. N_2O IR transitions for the (00^01-00^00) band are known up to J=100 for the R-branch. Line center profiles were collected over each IR transition between J=100-200 to identify the IR transition frequencies. The newly identified N_2O transitions and the tunable optical centrifuge were used to maximize the population in N_2O J=140 and J=165, using two different optical traps, to determine the relaxation dynamics in this region. Doppler-broadened line profiles show that rotational states below the maximized population have higher translational temperatures than rotational states near the peak of the distribution. From the near nascent distributions, the relaxation rate of the N_2O was measured to be 65 % of the gas kinetic collision rate for both optical traps. This result is compared with a previous study on CO relaxation dynamics.

ENERGY TRANSFER DYNAMICS OF HIGH-ENERGY MOLECULES

by

Christopher R. Lukowski

Dissertation submitted to the Faculty of the Graduate School of the
University of Maryland, College Park, in partial fulfillment
of the requirements for the degree of
Doctor of Philosophy
2023

Advisory Committee:
Professor Amy Mullin, Chair
Professor Millard Alexander
Professor Leah Dodson
Professor Daniel Falvey
Professor Lee Mundy

Dedication

To my family

Acknowledgements

First and foremost, I would like to acknowledge my advisor Dr. Amy Mullin. Since joining her research group in December 2017, she has pushed me to become a better scientist. She has always been there whenever I needed anything, and she has prepared me to be a scientist moving forward. I would also like to thank my committee for taking the time to read and provide feedback on this thesis, Dr. Millard Alexander, Dr. Daniel Falvey, Dr. Leah Dodson, and Dr. Lee Mundy.

Second, I would like to acknowledge everyone who has helped me during my time in the Mullin group. When I first started Dr. Hannah Ogden, Dr. Tara Michael, and Dr. Paul Diss fully accepted me into the group. I wouldn't have survived without Paul taking me under his wing for the first couple of years. Hannah and Tara have both been a tremendous resource whenever needed and I'm so glad we got to spend time together. For the last 3 years, Mike Ritter, Pierce van Mulbregt, and Eric Crump have provided great discussions as well as becoming some of my closest friends. Simone DeSouza has worked with me for the past 2 years and is more than willing to do anything to help out. I also would not have made it here without my roommate for the last 4 years David King.

Finally, I could not have done this without the support of my family and my wonderful fiancée, Lauren who has been a constant support for the last 9 years even as we have had to spend more time apart while I completed graduate school.

Table of Contents

List of Tables

List of Figures

List of Abbreviations

IR	Infrared
UV	Ultraviolet
IVR	Intramolecular vibrational redistribution
LIF	Laser Induced Fluorescence
IC	Internal conversion
CW	Continuous Wave
FWHM	Full width at Half Maximum
COM	Center of Mass
Nd:YAG	Neodymium-doped yttrium-aluminum garnet
BBO	β-barium borate
THG	Third Harmonic Generation
OPO	Optical Parametric Oscillator
OC	Optical Centrifuge
FHG	Fourth Harmonic Generation
PPLN	Periodically poled lithium niobate
FSR	Free Spectral Range
PBC	Polarizing beam cube
MPA	Multi-pass amplifier
SFG	Sum frequency generation
QCL	Quantum Cascade Laser
IP	In-plane

OOP	Out-of-plane
UVA	Ultraviolet Absorption
KCSI	Kinetically controlled selective ionization
IRF	Infrared fluorescence
GRETCHEN	Golden Rule Excitation Transfer in Collisions of High Energy Molecules

Chapter 1: Introduction

How energy is dissipated from energetic molecules is fundamental to understanding the dynamics and mechanisms of chemical processes. The development of pulsed lasers enabled new tools for investigations of high-energy molecules. Once molecules are photo-excited, the competition between chemical processes, collisional deactivation, and photodissociation can be investigated. The three studies presented in this thesis investigate the quantum state-resolved dynamics of photodissociation and collisional energy transfer. In each study, reaction or collision products are detected with high-resolution transient IR absorption spectroscopy.

In quantum mechanics, the Hamiltonian operator describes the total energy of the system. The Hamiltonian for molecules is often separated into electronic, vibrational, and rotational operators, and the solution of the Schrodinger equation yields the electronic, vibrational, and rotational energies of the molecule. However, a separable Hamiltonian does not account for coupling between the molecular degrees of freedom and therefore does not account for the dynamical processes that result from such couplings. The research presented in this thesis investigates the dynamics of photo-activated molecules with energy in the electronic, vibrational, or rotational degrees of freedom.

The first study investigates how bimolecular collisions transform vibrational energy in methylated pyridine molecules to rotational and translational energy in CO_2. The second study investigates how electronic energy in SO_2 transforms into rotational and translational energy of photodissociation products. The third study investigates

how highly rotationally excited N_2O molecules are relaxed by collisions with ambient N_2O molecules at 300 K, where large energy mismatches exist between the rotationally excited molecules and bath molecules.

1.1 Electronic and Vibrational Excitation on Molecules

The first working laser was demonstrated in 1960 and opened a new set of tools for studying excited states of molecules.[1] Many experiments focused on reactions and energy transfer dynamics of molecules that were electronically excited. Under collision-free conditions, the electronically excited molecules can undergo dissociation, fluorescence, and/or non-radiative decay to the ground electronic state, depending on the excitation wavelength.

A major discovery was the importance of intramolecular vibrational redistribution (IVR) in the excited electronic state of molecules.[2] Laser-induced fluorescence (LIF) on cold naphthalene showed that when the energy in the electronic state was greater than 3,000 cm^{-1} the vibrational bands were broadened.[3–5] The broadening of vibronic bands is direct evidence of IVR following electronic excitation. The presence of IVR led to the discovery of "channel 3" in benzene, where the electronic excitation leads to the formation of highly vibrationally excited molecules in the ground electronic state by way of internal conversion (IC).[6–8] The fluorescence quantum yields when benzene was excited at $\lambda \leq 248$ nm ranged was near 0. The quantum yield for IC to the ground electronic state is as high as 0.6, leading to a mechanism to generate highly vibrationally excited molecules by absorption of UV light.[6,8] In the "channel 3" region there is also fast intersystem crossing to the triplet state.(ref) Additional experimental

techniques exist for the vibrational excitation of molecules with varying state-selectivity and complexity.[9]

In chapter 3 of this thesis, the energy transfer dynamics of highly vibrationally excited collidine (2,4,6-trimethylpyridine) with ambient 300 K CO_2 is studied by measuring the state-resolved energy gain of the CO_2. Collidine has a near unity quantum yield for internal conversion to the ground electronic state when excited with λ=266 nm light. Previous work on a series of methylated pyridines initially excited with λ=266 nm light showed that as the number of vibrational modes increased, the probability of the large energy transfer events decreased, and the energy transfer distribution function was compressed to smaller ΔE values.[10–12] Additionally, the slope of the energy transfer distribution function and the slope of the vibrational state density decay were found to be correlated. Collidine has 54 vibrational modes and the highest state density relative to the series of previously studied methylated pyridines. This project was designed to answer a number of questions. How does the average energy per mode affect the efficiency of collisional relaxation by impulsive collisions? Does the correlation between the energy transfer distribution function and the vibrational state density persist as the donor molecules increase in complexity?

Dissociation competes with fluorescence, internal conversion, and intersystem crossing in electronically excited molecules. Photodissociation of polyatomic molecules depends on the nature of the excited electronic state, coupling with other electronic states, and the coupling of the vibrational modes.[13] Polyatomic molecules have at least three vibrational modes that can couple, so a two-dimensional description of the potential energy surface is incomplete. If the lifetime of the excited electronic

state is longer than the lifetime of IVR, then the photodissociation process occurs via a predissociative, or metastable, state. Predissociation can occur in two different ways. The first is a slow unimolecular reaction in the upper state, where the dissociation occurs by vibrational or rotational predissociation. The second way is spin-orbit coupling between electronic states leading to nonadiabatic relaxation resulting in dissociation. The latter has been observed for molecules such as N_2O, N_2O^+, and H_2S^+.[14–16]

In Chapter 4 of this thesis, the photodissociation dynamics of SO_2 are investigated to determine the mechanism by which SO_2 dissociates from a predissociative excited electronic state. Prior to this study, the photodissociation threshold was observed to be at λ=220 nm, but direct dissociation from a repulsive state is predicated by ab initio calculations to require light with λ=182 nm.[17–20] In the work reported here, SO product state energy distributions were measured as a function of photolysis wavelength using λ=220-212 nm, near the dissociation threshold. The experimental results are compared with new ab initio calculations by Dr. Jacek Klos and Dr. Millard Alexander that allow for spin-orbit coupling and bond angle opening. The calculations were done with multireference configuration interaction and the new potential energy curves are shown in Chapter 4 as well. This comparison explains the mechanism by which the dissociation occurs.

1.2 Rotational Excitation of Molecules

In addition to electronic and vibrational excitation, techniques have been developed to study energy transfer with highly rotationally excited molecules. Early techniques for generating molecules in high rotational states were by flame, collisions, and

chemical reactions. In emission from a flame at 1800 K, CO_2 rotational states up to J=146 were observed.[21] However, when the CO_2 gas is heated the states populated at room temperature are broadened leading to loss of spectral resolution. Highly rotationally excited HF was formed by first vibrationally exciting HF to ν=1, which relaxed via collisions and moved energy to rotation and translation, populating HF(ν=0) in the J=13 rotational state with a rotational energy of E_{rot} =3673 cm^{-1}.[22,23]

In the few decades, a new technique using a strong field approach called an optical centrifuge was developed. The optical centrifuge was first proposed and developed by Karczmareck et al. in 1999 and uses two ultrafast laser pulses that are spatially and temporally overlapped, each with opposite chirp and circular polarization.[24] The overlap of these pulses generates a linearly polarized optical field that undergoes angular acceleration over the duration of the pulse. Molecules interact with the field through an induced dipole interaction. The trapped molecules are thereby driven into extreme rotational states with orientated angular momentum. The excitation process has been described both classically and quantum mechanically. In the classical description, molecules self-adjust their rotation continuously with the rotation of the accelerating optical field, thus increasing their rotational energy levels. In the quantum description, the molecules are excited into the high-energy rotational states by a stimulated Raman ladder of successive states.[25]

The Mullin group has made advances in studying the relaxation dynamics of highly rotationally excited molecules. Yuan et al. reported new IR R-branch transition frequencies for $N_2O(00^01\text{-}00^00)$ up to R99.[26] Prior studies had reported IR transitions only up to J=92 for N_2O ν_3 absorption. Ogden et al. expanded on N_2O and reported

new IR lines for N_2O R140-R205.[27] Michael et al. reported the nascent distribution of optically centrifuged CO molecules and the rate constant for collisions was about 20% that of the gas-kinetic collision rate.[28] Ogden and Michael. also developed a tunable optical centrifuge and demonstrated that by limiting the spectrum of one of the pulses, the rotational excitation of molecules can be reduced.

The third study presented in this thesis uses the optical centrifuge to excite N_2O molecules into extreme rotational states with J=100-200 in the ground electronic and vibrational state. The rotational states were probed using R-branch transitions of the ($00^0$1-$00^0$0) absorption band. Chapter 5 identifies the IR transitions for J=100-200 for the R-branch using a tunable optical centrifuge. In Chapter 6, the relaxation dynamics of optically centrifuged N_2O is reported and compared to the previously reported work on collisions of rotationally excited CO.

1.3 Outline

- Chapter 2: A description of the high-resolution transient IR absorption experimental instruments used in this thesis is presented, including the theory of transient IR absorption, the generation of UV pulses, and the optical centrifuge.
- Chapter 3: The collisional deactivation of highly vibrationally excited collidine (E_{vib}=385000 cm^{-1}) with a bath CO_2 is studied. The results are compared to dynamic studies on other methyl derivatives of pyridine. The full state-resolved distribution of scattered CO_2 was measured to determine the relative role of strong and weak collisions in the relaxation process. Absolute rate constants

show that vibrationally excited collidine undergoes faster collisional quenching than the other methyl derivatives of pyridine.

- Chapter 4: The photodissociation of SO_2 near the dissociation threshold of λ=220 nm is investigated by an energy-dependent study with tunable UV excitation. The nascent SO product distributions, energy partitioning, and theoretical calculations are used to determine the photodissociation mechanism.
- Chapter 5: The observation of new IR spectral lines of the N_2O (00^01-00^00) absorption band are reported for the R-branch. A bandhead in the R-branch is observed around J=116 allowing for spectral fingerprinting of the higher rotational states using known IR transitions from lower rotational states. The IR transitions are compared to model calculations and used as probe transitions for the study in Chapter 6.
- Chapter 6: The relaxation dynamics of rotationally excited N_2O with J=100-180 are reported. For these experiments, the optical trap was controlled such that the population in the J=140 and J=165 state was maximized. Doppler-broadened line profiles show that rotational states below the maximized state are populated by collisions. The relaxation rate of the optically centrifuged N_2O are about 65% that of the gas kinetic collision rate.

Chapter 2: Experimental Instrumentation and Methods

This Chapter describes the experimental techniques and instrumentation used to prepare and study highly excited molecules and their dynamics. All experiments in this thesis used high-resolution transient IR spectroscopy to probe the outcome of photoactivated molecular processes. In high-resolution transient IR absorption spectroscopy, a pump laser excites the molecules in a specific way, then a continuous-wave (CW) IR laser probes the molecules that result from collisions, photodissociation, or optical excitation. The IR probe sources have extremely high resolution so that individual rovibrational states are detected. A general experimental approach is shown in Figure 2.1a for collinear pump and probe beams and Figure 2.1b for orthogonal pump and probe beams.

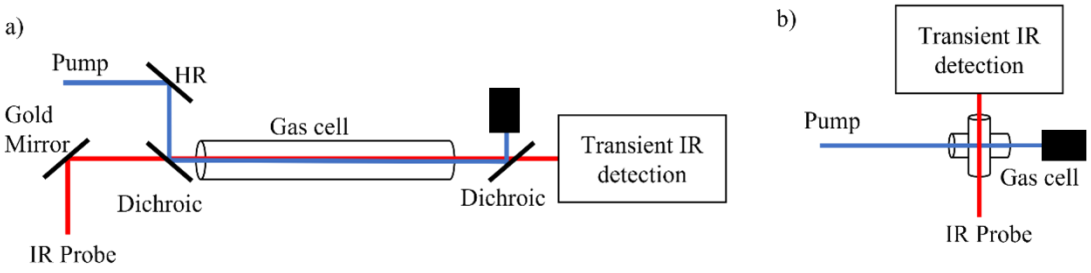

Figure 2.1 Pump-probe experimental apparatus with a) collinear beams and b) orthogonal beams. Here HR denotes a high-reflector mirror.

2.1 High-Resolution Transient IR Spectroscopy

2.1.1 Theory

Rovibrational transitions occur when the IR light frequency is resonant with the energy gap between two rovibrational states. The selection rules for rovibrational transitions are $\Delta J = \pm 1$ and $\Delta \nu = +1$, where J is the rotational quantum number and ν

is the vibrational quantum number. Figure 2.2 shows two representative transitions to probe for the CO_2 (00^00, J = 76,ν = 0). The notation for CO_2 vibration is (mn^lp) where *m*, *n*, and *p* are the quantum number for the symmetric stretch, bend, and asymmetric stretch respectively; and *l* is the vibrational angular momentum quantum number. P-branch transitions have a $\Delta J = -1$ and R-branch transitions have $\Delta J = +1$.

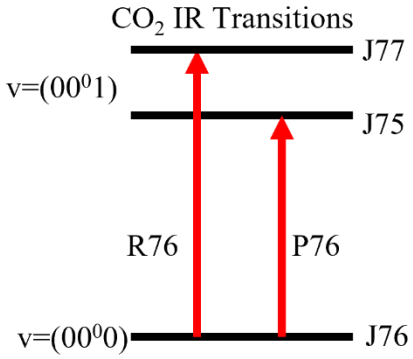

Figure 2.2: Schematic of the P76 and R76 IR transitions in the (00^01-00^00) band of CO_2.

The fractional IR absorption intensity of rovibronic states is proportional to the population of molecules in that rovibronic state. Beer's Law for IR absorption is

$$I_t = I_o e^{-\alpha p l} \tag{2.1}$$

where I_t is the transmitted IR intensity, I_o is the initial intensity, α is the absorption coefficient, p is the pressure of the gas, and l is the path length for absorption. The absorption coefficient, α, is the product of the absorption strength S, the lineshape factor $f(0)$, and the number density of molecules N, as shown in Equation 2.2.

$$\alpha = Sf(0)N \tag{2.2}$$

The number density of molecules N is determined by the ideal gas law at 296 K, the temperature for which S is determined, using Equation 2.3.

$$N = \frac{n}{V} = \frac{P}{RT} \tag{2.3}$$

Here n is the number of molecules, V is the volume, P is the pressure, R is the universal gas constant, and T is the temperature. The lineshape factor $f(0)$ is given by Equation 2.4.

$$f(0) = \frac{2}{\Delta\nu_{Dop}}\sqrt{\frac{\ln 2}{\pi}} \tag{2.4}$$

Here, $\Delta\nu_{Dop}$ is the full width at half maximum (FWHM) of the Doppler-broadened absorption line profile. The absorption strength S is defined by Equation 2.5.

$$S = \int_0^\infty \sigma(\nu)d\nu \tag{2.5}$$

Here, ν is the optical frequency, and $\sigma(\nu)$ is the frequency-dependent cross-section for absorption.

2.1.2 Doppler-Broadened Line Profiles

Doppler-broadened line profiles are used to determine the translational energy distribution of product molecules in individual vibrational states. A Doppler profile measures the velocity distribution of molecules in a given product state. Molecules in motion relative to the IR light source absorb at slightly different frequencies depending on their relative velocity based on the Doppler effect, given in Equation 2.6.

$$\nu = \nu_o\left(1 \pm \frac{\mathrm{v}}{\mathrm{c}}\right) \tag{2.6}$$

Here, ν is the IR frequency, ν_o is the line center IR frequency, v is the velocity, and c is the speed of light. Molecules with higher velocities absorb light further from ν_o. The integrated line intensities and, therefore, the population of rovibrational states must take the velocity distribution into account. The line shape factor $f(0)$ in Equation 2.4 accounts for the velocity distribution in Gaussian-shaped Doppler profiles.

Two different methods are used to determine Doppler widths, depending on how the product states were generated. The first method is used for product states populated via collisions. These Doppler-broadened line profiles yield the translational temperature of the rovibrational product state. The FWHM of these profiles $\Delta\nu_{obs}$ depends on the translational temperature of products, as shown in Equation 2.7.

$$\Delta\nu_{obs} = \sqrt{\frac{8k_B T \ln 2}{mc^2}}\nu_o \tag{2.7}$$

Here, k_B is Boltzmann's constant, T is the translational temperature, and m is the molecular mass.

The second method for measuring Doppler profiles was used for products from SO_2 photodissociation. Photodissociation introduces anisotropy in the angular distribution of products and the velocities in the center-of-mass (COM) frame affecting the line shapes of the observed Doppler profiles. The analysis of these Doppler profiles was based on the work by Zare and Herschbach.[95] The angular distribution of the photodissociation products for linearly polarized light is given by Equation 2.8.

$$W(\theta) = \frac{1}{4\pi}[1 + \beta \mathrm{P}_2(\cos\theta')P_2(\cos\theta)] \tag{2.8}$$

Here θ is the angle between the photolysis polarization and the product recoil, θ' is the angle between the UV photolysis polarization and the IR probe propagation, β is the anisotropy parameter, and P_2 is the second Legendre polynomial. For these experiments, the UV pump and IR probe beams were passed collinearly through the cell which simplifies Equation 2.8 because the $\cos(\theta') = 1$.

$$W(\theta) = \frac{1}{4\pi}[1 + \beta \mathrm{P}_2(\cos\theta)] \tag{2.9}$$

The anisotropy parameter, β, has two limiting cases. In one limiting case, $\beta = -1$ for products that recoil orthogonal to the IR beam propagation. In the other limiting case, and $\beta = 2$ for products that recoil along $\vec{k}_{IR}$. If the angular distribution is isotropic the anisotropy parameter is $\beta = 0$. The angular distribution of Doppler profiles for photodissociation products is described by Equation 2.10.

$$F(\zeta,\eta) = \left[1 + \frac{1}{2}\left(\frac{\beta}{\eta^2}\right)\left(3\zeta^2 - \eta^2 + \frac{3}{2}\right)\right][\mathrm{erf}(\zeta+\eta) - \mathrm{erf}(\zeta-\eta)]$$

$$\left[\frac{3}{4}\frac{\beta}{\eta^2}\frac{2}{\sqrt{\pi}}(\zeta-\eta)e^{-(\zeta-\eta)^2} - \frac{2}{\sqrt{\pi}}(\zeta+\eta)e^{-(\zeta-\eta)^2}\right] \quad (2.10)$$

Both ζ and η are dimensionless quantities and represent the recoil and laboratory velocities, respectively. and erf is the error function. The error function in this case is the normalized integral of $e^{-(x)^2}$ when the bounds are 0 to x. The η value is determined by conversation of energy. When the distribution is isotropic and $\beta = 0$, Equation 2.10 reduces to simply Equation 2.11.

$$F(\zeta,\eta) = A'[\mathrm{erf}(\zeta+\eta) - \mathrm{erf}(\zeta-\eta)] \quad (2.11)$$

Here A' is a scaling parameter at the line center. The fitting process will be discussed further in chapter 3.

2.1.3 State-Specific Number Densities

When there is no pump beam present, the cell is under equilibrium conditions and the gas pressure in the cell is determined by an absorption measurement of an IR transition. Beer's law is rearranged to solve for the static pressure as shown in Equation 2.12.

$$p = -\frac{\ln\left(\frac{I_t}{I_o}\right)}{Sf(0)Nl} \tag{2.12}$$

To determine the partial pressure of a single state J, it is necessary to remove the fractional rotational (f_j) and vibrational (f_v) populations from the absorption strength S by dividing by f_j and f_v of that state at 296 K.

$$p_j = -\frac{\ln\left(\frac{I_t}{I_o}\right)}{Sf(0)Nl} f_j f_v \tag{2.13}$$

State-specific number densities from transient IR absorption signals are determined from the ideal gas law and Eq. 2.13

$$\frac{N_j}{V} = \frac{p_j}{RT} = -\frac{\ln\left(\frac{I_t}{I_o}\right)}{Sf(0)l} f_j f_v \tag{2.14}$$

With N_j/V is the number density in the specific rovibrational state probed. Equation 2.14 is valid if the temperature is T = 296 K, the reference temperature for the HITRAN database used for the S values. The products of collisions and reactions have translational temperatures that are generally not the same as the equilibrium temperature. To account for the observed Doppler broadening Eq. 2.14 must be multiplied by the ratio of $\Delta\nu_{obs}/\Delta\nu_{Dop}$ where $\Delta\nu_{Dop}$ is the FWHM of a 296 K Doppler-broadened line profile.

$$\frac{N_j}{V} = -\frac{\ln\left(\frac{I_t}{I_o}\right)}{Sf(0)l} f_j f_v \frac{\Delta\nu_{obs}}{\Delta\nu_{Dop}} \tag{2.15}$$

2.1.4 Obtaining Transient IR absorption Signals

Absorption measurements of Doppler-broadened line profiles and state-specific populations depend on measuring the fractional transmitted IR intensity that is

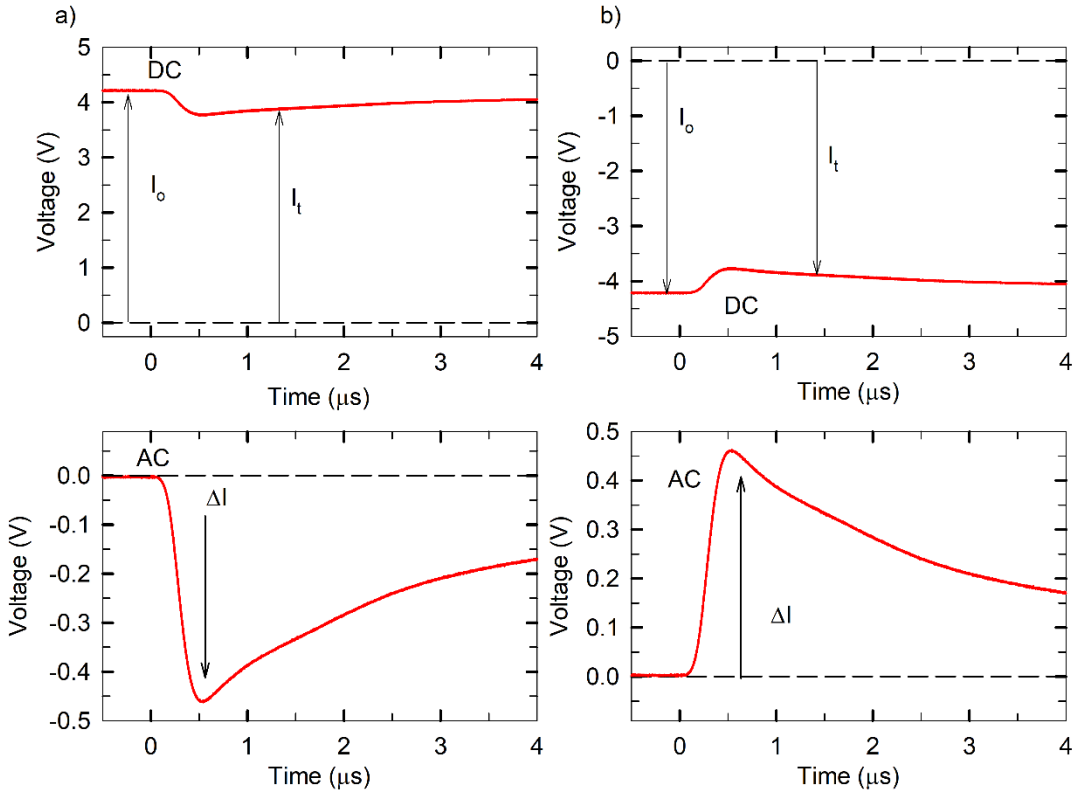

Figure 2.3 Traces for the AC and DC voltages of a transient IR absorption signal for a) Positively biased detector and b) a negatively biased detector.

absorbed, $\frac{\Delta I}{I_o}$, as a function of time. Transient IR absorption signals are measured by monitoring IR intensity on two channels of a digital oscilloscope with one channel DC-coupled and the other channel AC-coupled. Figure 2.3 shows an example of both the DC and AC-coupled channels collected for the CO_2 (00^00, P76) rotational state.

From the transient IR absorption signals the $\frac{\Delta I}{I_o}$ can be determined by Equation 2.16.

$$\frac{\Delta I}{I_o} = \frac{-\frac{AC}{DC}}{1 \pm \frac{AC}{DC}} \tag{2.16}$$

IR detectors were used with either a positive or negative bias. The numerator of Equation 2.15 does not depend on the bias of the detector, the negative sign is derived from the AC voltage being a measure of how much of the IR probe has been absorbed by the sample. The loss of IR light represents an appearance of population in the rovibronic state, and the negative ensures that the $\frac{\Delta I}{I_o}$ is positive for these appearance signals. In Equation 2.15 the denominator is dependent on the bias of the detector, for a positively biased detector the denominator would be $1 + AC/DC$. For a negatively biased detector, the denominator would be $1 - AC/DC$. The bias of the detector does not affect the $\frac{\Delta I}{I_O}$ that is measured.

2.2 Experimental Instrumentation for Studying Molecules in Electronically or Vibrationally Excited States

The first set of experiments that are described in Chapters 3 and 4 were performed with collinear pump and probe beams as in Figure 2.1a. In Chapter 3 pulsed UV light was used to photodissociate SO_2 via electronic excitation to a metastable state. In Chapter 4 pulsed UV light was used to vibrationally excite methylated pyridine. The experiments were performed in the single collision regime because the sample cell path length is 3 meters, enabling lower pressure conditions.

2.2.1 Generating UV Pulses for Electronic and Vibronic Excitation

The UV wavelengths studied here were generated in two ways. Both methods used a 10 Hz Nd:YAG and then underwent sum frequency generation to generate $\lambda = 355$ nm or $\lambda = 266$ nm. Table 2.1 shows the nonlinear BBO crystals used to generate each of the wavelengths in the Nd:YAG laser.

Table 2.1: Summary of wavelengths generated in the Nd:YAG laser.

Wavelength (nm)	Type	Process
532	BBO Type 1	Doubling 1064
355	BBO Type II	Mixing 532 and 1064
266	BBO Type II	Doubling 532

When using the THG crystal the λ=355 nm beam was used to pump an optical parametric oscillator (OPO, Continuum Lasers). The OPO has tunable output from λ=193-2700 nm. For the visible and IR portion of the wavelength range (400-2700 nm), the λ=355 pump beam undergoes spontaneous parametric down-conversion (SPDC) via a pair of BBO crystals. With SPDC the single pump photon is split into 2 photons of lower energy with subsequent energies that sum to the pump photon energy. The 2 photons are called the signal and the idler. In the case of the OPO, the signal beam will be the visible wavelengths, and the idler beam will be the IR wavelengths.

When the OPO is pumped with 250 mJ per pulse of λ=355 nm the output power of the visible light is 80 mJ per pulse at λ=425 nm. The output power is dependent on the wavelength of visible light and has a range of 10-80 mJ per pulse between λ=400-709.4 nm. For this dissertation, the OPO was used to generate λ=212-224 nm and λ=266 nm UV light. For UV generation, the visible output is doubled again and for some UV

wavelengths mixed with residual λ=1064 nm from the Nd:YAG. When using λ=266 nm excitation for Chapter 4 the FHG was placed in the Nd:YAG instead of the THG and the resulting λ=266 nm beam was used directly.

2.2.2 High-Resolution Transient IR Probe Scheme and Sources

Modulated IR light sources were used to probe the rovibrational transitions of the gas molecules after photodissociation or collisions. The IR modulation is synced with the Nd:YAG laser timing so the excitation pulse occurs in the middle of the IR modulation cycle, as shown in Figure 2.4. The synchronization is realized by externally triggering the Nd:YAG laser with a delay generator so the Q-switch of the Nd:YAG is triggered with a 10 Hz pulse train from the IR source. A time delay is used to center the UV pulse in the modulation cycle.

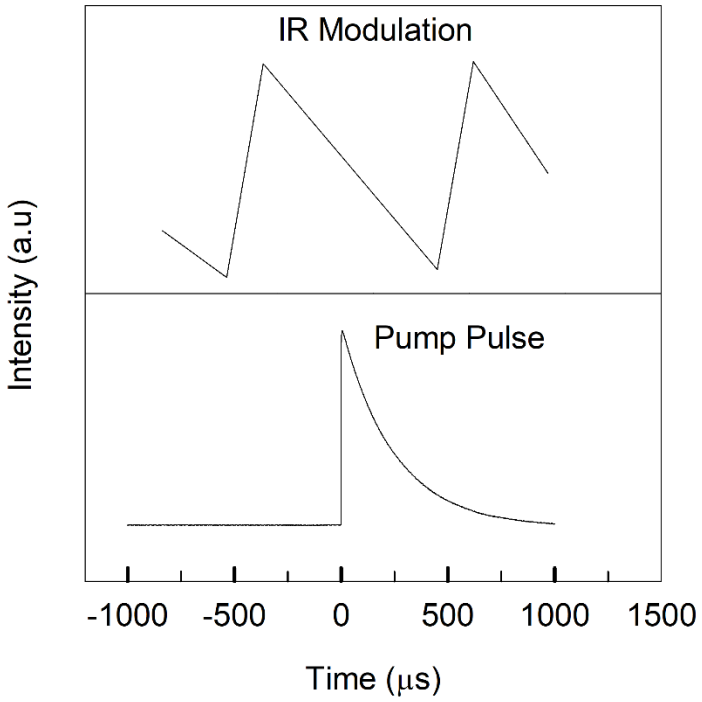

Figure 2.4 The IR modulation of the Pb-salt diode, and the pump pulse as measured on the photodiode just prior to the sample cell. The pump pulse is centered in the IR modulation cycle.

One of the IR probe sources was a CW Pb-salt diode laser with output at $\lambda = 4.4 - 4.5$ μm. The Pb-salt diode is a semiconductor laser and has a spectral resolution of $\Delta\nu_{diode}$=3×10^{-4} cm^{-1} and is modulated internally at 1 kHz. The other IR probe source was a CW mid-IR OPO. The mid-IR OPO generates IR light by a periodically poled lithium niobate (PPLN) crystal that is pumped by a fiber laser. The output of the mid-IR OPO ranges from λ=2.5-3.2 μm and has a spectral resolution of $\Delta\nu_{IR-OPO}$=3×10^{-5} cm^{-1}. The mid-IR is modulated externally at 100 Hz. For both IR sources, prior to passing through the 3 m sample cell, roughly 5% of the beam is directed down a reference cell of either CO_2 or N_2O and another 5% of the beam is directed to a confocal Fabry-Perot etalon.

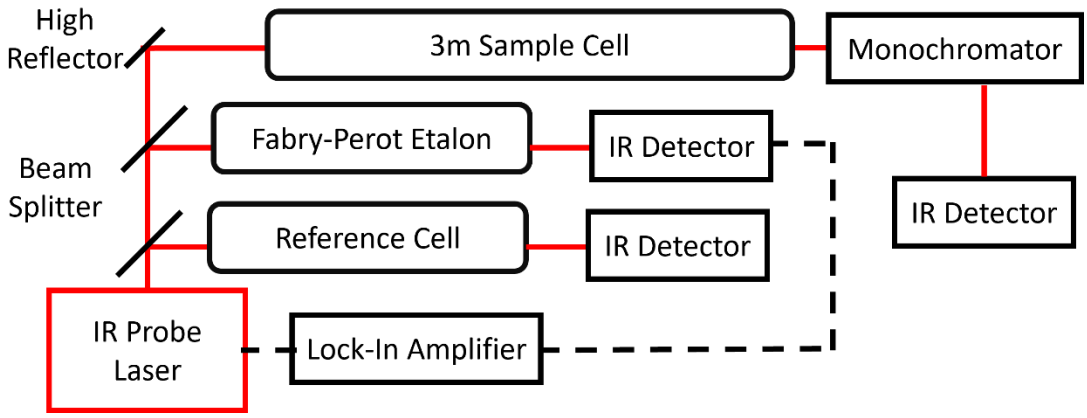

Figure 2.5 IR beam path for both the Pb-salt diode and the CW mid-IR OPO. Each IR detector is an indium antimonide (InSb). The wavelength is controlled by the Fabry-Perot etalon.

The confocal Fabry-Perot etalon is used to wavelength stabilize the IR light. A beam splitter directs part of the IR beam towards 2 curved mirrors and the beam is passed through in a bow-tie configuration, shown in Figure 2.6a. The length of the etalon path is controlled by a rotating CaF_2 optic. The distance that the IR beam travels determines which wavelengths will have an integral number of quarter wavelengths causing constructive interference. The constructive interference leads to IR peaks

called fringes that are evenly spaced. The spacing between the fringes is the free spectral range (FSR) and is calculated by Equation 2.17.

$$FSR = \frac{c}{4l} \tag{2.17}$$

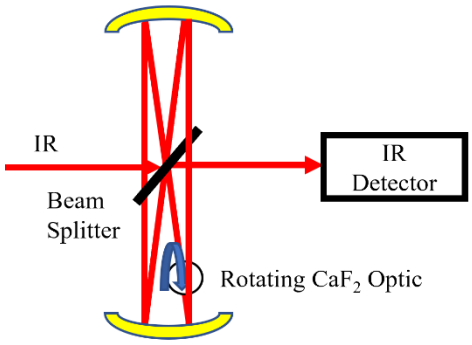

Figure 2.6 Schematic of the Fabry-Perot Etalon with a CaF_2 optic that can is tuned to control the IR wavelength.

2.2.3 Experimental Pressure

A flowing-gas vacuum system is used to maintain a constant pressure in the sample cell. The flowing-gas system is built to be able to have one or two gases flowing simultaneously. For experiments with SO_2 photodissociation, a needle valve was used to control the flow rate, and the pressure in the sample cell was kept near 20 mTorr as measured on a baratron. For the experiments investigating collisional energy transfer, two gases were flowed simultaneously through the cell. The donor gas (collidine) had a pressure of 2-2.5 mTorr as measured on a baratron, and the total pressure in the cell was kept between 5-10 mTorr after the addition of CO_2. Each gas flow was maintained by an electronic flow controller. The partial pressure of CO_2 was determined by measuring the spectroscopic pressure of the CO_2 in the sample cell using Equation 2.11.

2.3 Optical Centrifuge for Exciting Molecules in Extreme Rotational States

The second experimental apparatus that was used in the research reported here was an optical centrifuge spectrometer. This section describes the optical centrifuge spectrometer and provides the background theory of the optical centrifuge.

2.3.1 Theory of the Optical Centrifuge

Fundamental to the optical centrifuge is the interaction between the molecule and the optical field of the pulse. The optical field induces a dipole moment in the molecule. A molecule with an electron cloud interacts with the linearly polarized field that has a potential energy curve that is defined by Equation 2.18

$$U = -\frac{1}{4}\Delta\alpha E^2 \cos^2(\theta) \tag{2.18}$$

Here, $\Delta\alpha$ is the anisotropic polarizability of the molecule, E is the amplitude of the optical field, and θ is the angle between the molecular axis and the electric field. The $\Delta\alpha$ is defined by $\Delta\alpha = \alpha_{\parallel} - \alpha_{\perp}$, with $\alpha_{\parallel}$ being the polarizability parallel to the molecular axis, and $\alpha_{\perp}$ is the polarizability perpendicular to the molecular axis. Linear molecules like CO_2 or N_2O have a $\alpha_{\parallel} > \alpha_{\perp}$ and the molecules will align with the optical field. Molecules are more efficiently trapped as θ approaches 0, as shown in equation 2.18.

The optical centrifuge pulse is designed to have linear polarization that undergoes angular acceleration over time of the pulse. The molecules will rotate at the same angular frequency as the field. By angularly accelerating the polarization rotation, the molecules will angularly accelerate as well and increase their angular momentum in a controlled manner.

The angularly accelerating field is formed by the combination of two counter-rotating circular polarized pulses in both space and time. The two pulses are linearly chirped, meaning that the optical frequency changes linearly as a function of time. One of the pulses is positively chirped and the other is negatively chirped. The polarization rotates with a constant acceleration equal to β, creating a steadily accelerating optical trap to rotationally excite the molecules. The positive (ω_1) and negatively (ω_2) chirped pulses are as shown in Equations 2.19 and 2.20 respectively, where ω_o is the initial frequency of the optical centrifuge pulse.

$$\omega_1 = \omega_o + \beta t \tag{2.19}$$

$$\omega_2 = \omega_o - \beta t \tag{2.20}$$

The optical centrifuge has an angular frequency Ω_{OC} that is defined by the instantaneous frequency difference between the pair of pulses as in Eqs. 2.19 and 2.20. The maximum value of Ω_{OC} is dependent on the pulse bandwidth $\Delta\omega$ with $\Omega_{max} = \Delta\omega/2$. The instantaneous frequency difference between the pair of pulses is shown in Equation 2.21.

$$\Omega_{OC} = \frac{1}{2}\Delta\omega = \frac{1}{2}\big(\omega_1(t) - \omega_2(t)\big) \tag{2.21}$$

Figure 2.7a shows the spectral profiles for the pair of oppositely chirped pulses and Figure 2.7b shows the spectral profile of the optical centrifuge.

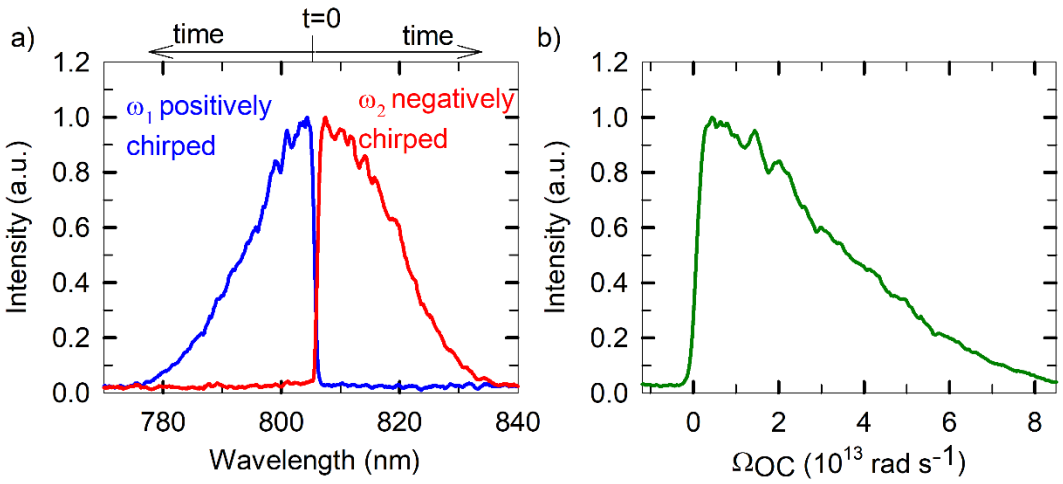

Figure 2.7 a) Spectral profile of the positively and negatively chirped pulses used to create the optical centrifuge. b) Spectral profile of the angular frequency of the optical centrifuge (Ω_{OC}).

The optical centrifuge traps and angularly accelerates molecules at the same frequency as Ω_{OC}. By relating the classical energy to the quantum energy for a rigid rotor the angular frequency of specific rotational states can be calculated. The classical rotational energy is given in Equation 2.22 where I is the moment of inertia and Ω_j is the angular frequency.

$$E_{rot} = \frac{1}{2} I \Omega_J^2 \tag{2.22}$$

The quantum description of rotational energy comes from an expansion of the rigid rotor model, where $B=\frac{\hbar}{2I}$ being the rotational constant, D is the centrifugal distortion constant, and J is the rotational quantum number.

$$E_{rot} = BJ(J+1) - D(J(J+1))^2 + H(J(J+1))^3 \tag{2.23}$$

Equating Equation 2.22 and the first term of Equation 2.23 and solving for Ω_J the angular frequency of rotational states is given in Equation 2.24.

$$\Omega_J = \frac{\hbar}{I}\sqrt{J(J+1)} \tag{2.24}$$

2.3.2 Generating the Optical Centrifuge Pulses

As described in the previous section, the optical centrifuge is formed using a pair of pulses that are overlapped in space and time, with opposite linear chirps and circular polarization. A schematic of the optical centrifuge is shown in Figure 2.8. The key components are an ultrafast Ti:Sapphire oscillator, a pulse stretcher/amplifier, a custom-built pulse shaper, a multi-pass amplifier, and a polarizing beam cube (PBC).

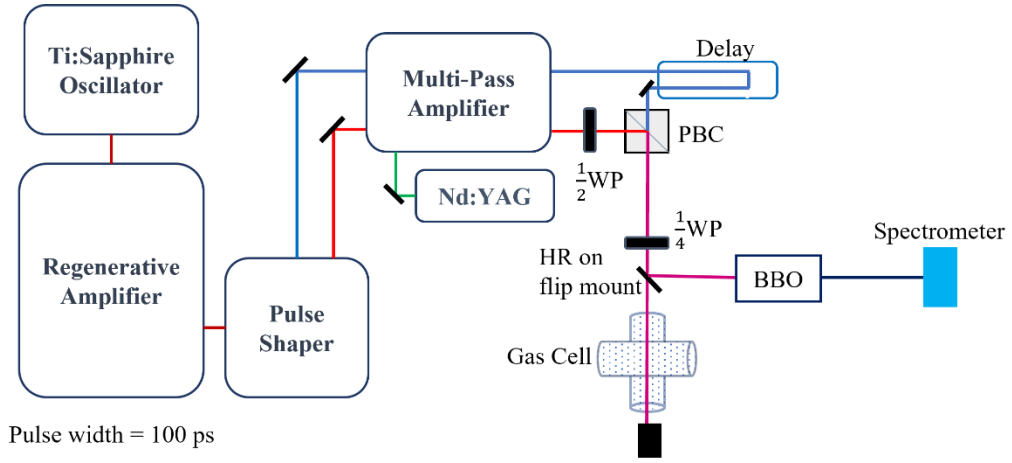

Figure 2.8 The optical centrifuge experimental setup. A Ti:Sapphire oscillator generates a mode-locked pulse centered at λ=806 nm. The pulse is stretched in time, given a positive chirp, amplified in a regenerative amplifier, and then spectral split in a pulse shaper. Each pulse is amplified to 20 mJ per pulse, then recombined in space and time by a delay stage and a PBC. The $\frac{1}{4}$ waveplate induces opposite circular polarization in the pair of pulses.

The ultrafast Ti:Sapphire oscillator generates a 40 fs, mode-locked pulse centered around λ=806 nm with a repetition rate of 80 MHz. The power output of the Ti: Sapphire oscillator ranges from 330-430 mW. The mode-locked pulses are stretched in time to 100 ps in the pulse stretcher. A positive chirp is introduced in the stretching process. The pulse is amplified in a regenerative amplifier with a repetition rate of 10 Hz. The power of the pulse after the regenerative amplifier is 8-10 mW. In the custom-

built pulse shaper, the pulse is dispersed off a grating, then spectral cut in half with a knife-edge mirror at the central wavelength. The positively chirped pulse, ω_1, is refocused by a series of gratings then exits the pulse shaper, while the pulse containing wavelengths $\lambda >$806 nm, ω_2, the chirp becomes negative through a series of gratings prior to exiting the pulse shaper.

Each pulse is then amplified further to approximately 200 mW in the multi-pass amplifier (MPA). The MPA has two Ti:Sapphire crystals that are pumped with λ=532 nm from an Nd:YAG. The positively chirped pulse ω_1 goes through a delay stage after the MPA to overlap the pulses in time. The PBC is used to overlap the pulses in space. The circular polarization of the pulses is achieved by the quarter waveplate after the PBC. The pulses are focused to a beam waist of 53 μm at the center of the cell using a 50 cm focal length lens.

Cross-correlation is used to ensure that the pulses are spatially and temporally overlapped. The optical centrifuge beam is directed towards a nonlinear BBO Type 1 crystal to measure the sum frequency generation(SFG) of the pulses. SFG is a second-order nonlinear process where the frequencies of ω_1 and ω_2 are combined to give output light of ω_1+ω_2. In this way, the 800 nm pulses are combined to give 400 nm light. The intensity of the 400 nm light is monitored on an Ocean Optics USB 2000 Spectrometer. When the pulses are spatial and temporal overlapped the intensity of the combined pulses is 10 times that of the individual pulses, shown in Figure 2.9.

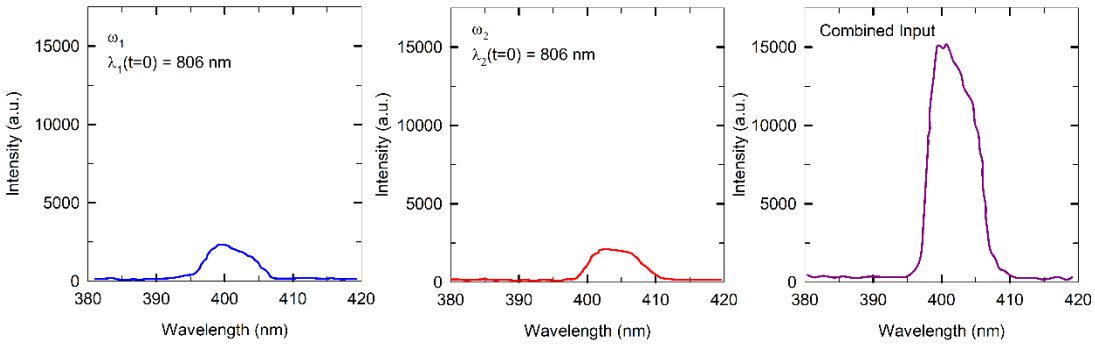

Figure 2.9 Spectra of each pulse of the optical centrifuge, ω_1 in blue, ω_2 in red, and the combined pulses where then the pulses are spatially and temporally overlapped.

2.3.3 Controlling the Rotational Excitation with a Tunable Optical Centrifuge

A tunable optical centrifuge was used in the experiments described in Chapters 5 and 6. "Tuning" the optical centrifuge controls the amount of rotational energy to which molecules are excited. Tunability is achieved by reducing the spectral bandwidth of the ω_1 pulse. As shown in Figure 2.10, an adjustable beam block in the pulse shaper removes selected short wavelengths of ω_1, thereby reducing the spectral bandwidth and Ω_{max}.

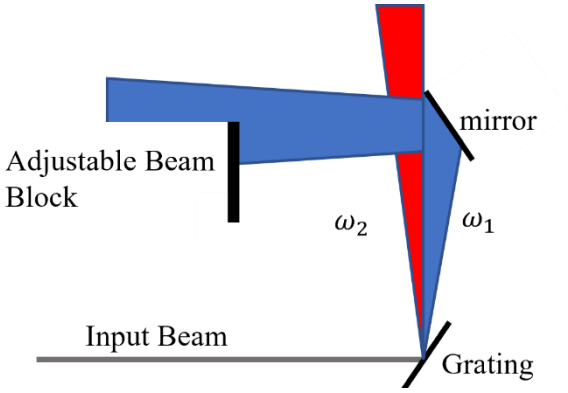

Figure 2.10 Schematic diagram showing how the optical centrifuge can be tuned by blocking the part of the positively chirped pulse, ω_1.

By removing the high frequency components of the positively chirped pulse, the angular acceleration of the optical trap is reduced since the angular acceleration depends on the instantaneous difference between the pair of pulses. Reducing the

spectral bandwidth can lead to damage to the MPA. To avoid such damage, the pump power is reduced by an amount proportional to the reduction in bandwidth. Figure 2.11 shows the spectral profile of the optical centrifuge at full bandwidth and a reduced bandwidth. The adjustable beam block is controlled with a micrometer.

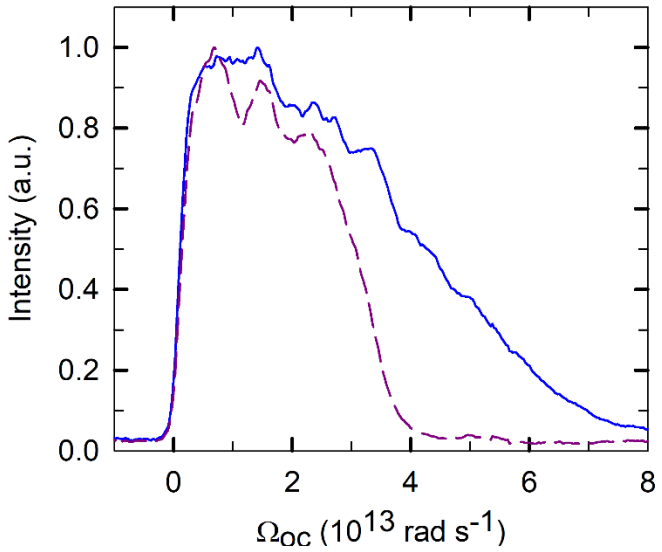

Figure 2.11 Spectral profile of the optical trap. At full bandwidth (solid blue line) the optical centrifuge can excite molecules up to $\Omega_{OC} = 6\times10^{13}$ rad s^{-1}. When the bandwidth is reduced the optical centrifuge will only excite to roughly $\Omega_{J140} = 3\times10^{13}$ rad s^{-1}. The reduced bandwidth lowers the distribution of rotationally excited molecules

2.3.4 Transient IR Spectroscopy of Optically Centrifuged Molecules

The optical centrifuge creates an ensemble of molecules with an inverted rotational distribution and oriented angular momentum vectors. The optically centrifuged molecules were detected with high-resolution transient IR absorption using a quantum cascade laser (QCL) operating at 4.3 μm. The QCL has tunable output between 2240-2380 cm^{-1} with a resolution of $\Delta\nu_{QCL}$=0.0003 cm^{-1}. The high-resolution QCL allows for individual rotational states to be detected and for Doppler-broadened line profiles to be measured. The IR wavelength is monitored on a wavemeter that is calibrated daily with a known CO_2 IR transition(P76). The IR wavelength is controlled by an active

feedback loop with a scanning Fabry-Perot etalon. The IR detectors are indium antimonide (InSb) cooled with liquid nitrogen. The sample detector has a rise time of 200 ns and the etalon detector has a rise time of 300 ns. The IR setup is shown in Figure 2.12.

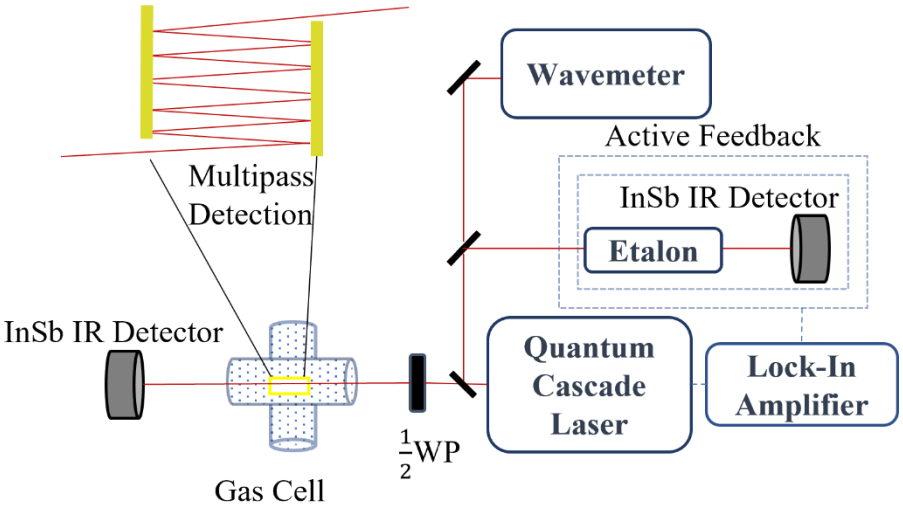

Figure 2.12 Setup for transient IR absorption spectroscopy of optically centrifuged molecules. Two gold mirrors inside the sample cell are arranged for 11-fold multi-pass IR detection. The IR wavelength is monitored on a wavemeter and is controlled by a Fabry-Perot etalon.

These experiments used a flat-flat tunable Fabry-Perot etalon with a cavity length l. The IR wavelength is tuned by applying a voltage to a piezoelectric transducer that is attached to one of the mirrors, as shown in figure 2.13.

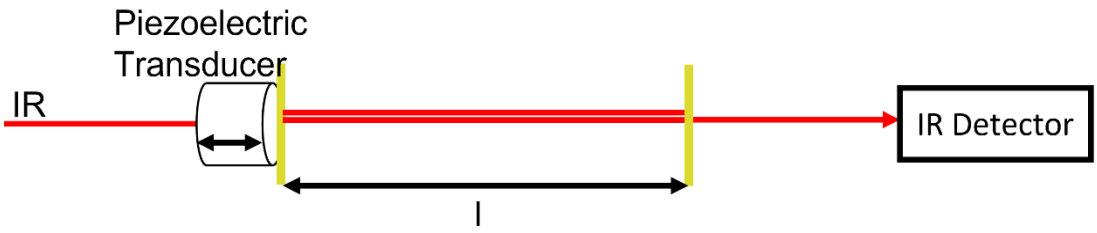

Figure 2.13 Flat-flat Fabry-Perot Etalon with two parallel gold mirrors. The wavelength is tuned by a piezoelectric transducer that is controlled by a voltage. When the voltage is applied the transducer will expand or contract.

The voltage has the transducer expand or contract to change the distance l of the cavity. The change in distance will change what wavelength will have an integral number of half cycles causing constructive interference and fringes. The FSR for a flat-flat is given by Equation 2.25.

$$FSR = \frac{c}{2l} \tag{2.25}$$

The modulated QCL output is locked to a fringe of the etalon and the IR wavelength is controlled by tuning the etalon spacing.

2.3.5 Polarization Sensitive Measurements

The polarization of the QCL light is controlled with a half-waveplate. Both vertical (s-polarized) and horizontal (p-polarized) polarization were used to detect optically centrifuged molecules in order to measure the orientational anisotropy. The optically centrifuged molecules rotate in the x-y plane and with angular momentum orientated along the z-axis. Figure 2.14 shows the geometry of the optical centrifuge interaction region. The optical centrifuge pulse propagates along the z-direction. S-polarized IR detection measures molecules with an angular momentum component along the x or z axis. P-polarized IR detection measures molecules with an angular momentum component along the x or y-axis.

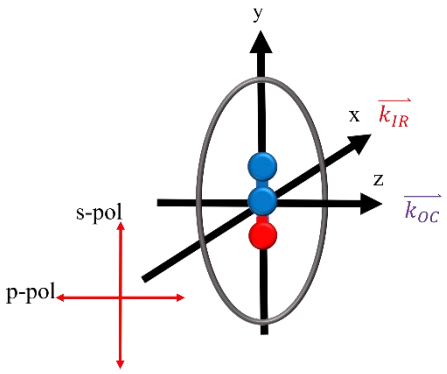

Figure 2.14 Polarization of the IR probe beam. When the IR configuration is s-polarized the IR beam has vertical polarization and horizontal polarization when the IR probe is p=polarized. The gray circle represents a molecule rotating in the xy-plane with angular momentum in the z axis.

Transient absorption signals collected with s and p-polarization are used to determine the orientational anisotropy of the centrifuged molecules. The optical centrifuge has cylindrical symmetry about the z-axis. The in-plane transient absorption signals are molecules with angular momentum in the z-axis. Optically centrifuged molecules with a component of their angular momentum along the z-axis are considered in-plane (IP) rotors. The IP component is determined by Equation 2.26.

Molecules with a component of the angular momentum along the x- or y-axis are considered out-of-plane (OOP) rotors. The OOP component is determined by Equation 2.27.

$$\mathrm{IP} = 2\mathrm{s} - \mathrm{p} \tag{2.26}$$

$$\mathrm{OOP} = 2\mathrm{p} \tag{2.27}$$

The orientational anisotropy, r, is given by Equation 2.28.

$$r = \frac{IP}{IP+OOP} = \frac{2s-p}{2s+p} \tag{2.28}$$

The orientational anisotropy of these high-energy extreme rotational states as they relax through collisions becomes isotropic with r = 0.33.

Chapter 3: Collisional Energy Transfer of Highly Vibrational Excited Collidine($E_{vib} = 38552\ cm^{-1}$) via Collisions with CO_2: Correlation with State Density

3.1 Introduction

Unimolecular reactions require internal energy to overcome the reaction barrier. Collisions that deactivate highly vibrationally excited molecules compete with unimolecular reactions. A century ago, Lindemann identified the importance of activating and deactivating collisions on the observed pressure dependence of unimolecular reaction rate constants. Furthermore, Hinshelwood recognized the role of the vibrational degrees of freedom in the rates for unimolecular reactions.[29] Understanding the dynamics of deactivating collisions and the effect of donor vibrational modes is important for characterizing high temperature environments found in the atmosphere, plasmas, and combustion. This paper reports experiments that investigate how the structure of highly vibrationally excited donor molecules affects the relaxation dynamics.

A number of experimental techniques have been used to study the deactivation of large aromatic molecules including ultra-violet absorption (UVA)[30–35], kinetically controlled selective ionization (KCSI)[36–38], infrared fluorescence (IRF)[32,12,39–42], and high-resolution transient IR aborption.[10,11,48–51,34,41–47] These techniques prepare highly vibrationally excited molecules using pulsed UV absorption followed by non-radiative decay. IRF studies on a variety of bath gases with toluene as the excited donor molecule, showed that the average energy transfer step size, $\langle\langle \Delta E \rangle\rangle$, increases as the

size of the bath molecule increases. The $\langle\langle \Delta E \rangle\rangle$ is a bulk property measure and includes vibrational energy in the determination. As the number of vibrational modes in the energy donor molecule increases, the $\langle\langle \Delta E \rangle\rangle$ should increase as well. KCSI experiments also using toluene as the excited donor observed the same trend for the average amount of energy transferred per collision, $\langle \Delta E \rangle$.[36,37,52]The $\langle \Delta E \rangle$ for c-propane was 784 cm^{-1}, while for c-hexane the $\langle \Delta E \rangle$ was 1147 cm^{-1}. This increase was also observed for methane, ethane, and n-propane. As the number of vibrational modes increases in the energy donor molecule more energy is transferred per collision. IRF has also looked at the methylation of the donor molecule using pyridine. The trend of $\langle \Delta E \rangle$ increasing with increasing number of vibrational modes is seen with $\langle \Delta E \rangle$=180 cm^{-1} for pyridine, $\langle \Delta E \rangle$=303 cm^{-1} for methylpyridine, and $\langle \Delta E \rangle$=340 cm^{-1} for dimethylpyridine and trimethylpyridine.[53]

Besides studying different bath molecules, experiments have also been conducted on systems that increase the size of the donor molecule to investigate what effect it has on the energy characteristics of the collisions. A transient IR absorption study showed that for pyrazine and methylpyrazine if fitting the data to a single exponential the average energy of downward collisions, $\langle \Delta E \rangle_d$, increases from 536 cm^{-1} for pyrazine/CO_2 collisions to 682 cm^{-1} for methylpyrazine/CO_2 collisions.[43] However, the data does not fit well to a single exponential, using a biexponential function provides improves the fit and provides information about both weak and strong collisions. Using these parameters, the $\langle \Delta E \rangle_d$ for the pyrazine system is 990 cm^{-1} and the methylpyrazine has a $\langle \Delta E \rangle_d$ of 608 cm^{-1}.[43] Interestingly the parameter for strong collisions, γ, decreases from pyrazine to methylpyrazine while the weak collision parameter, α, increases. As

methyl groups are added to the donor molecules, the collisions that have lower changes in energy are dominant. The decrease in the strong collisions was observed for pyridine, methylpyridine and dimethylpyridine as well.[10,53,54]

Beyond determining the energy characteristics of the system, it is possible to measure the energy transfer distribution function (P(ΔE)) using KCSI and IR absorption. KCSI with toluene as a donor molecule showed that the P(ΔE) function could be well approximated by an exponential function and that the $\langle E \rangle_d$ is linearly dependent on $\langle E \rangle$.[36] High-resolution transient IR absorption measures state-specific product distribution and characterizes the rotational, translational, and vibrational energy of the scattered molecules. From these data, the P(ΔE) curves are determined for the vibrationally energy loss from the highly vibrationally excited donor.

Here we investigate the collision dynamics of highly vibrationally excited 2,4,6-trimethylpyridine (collidine) with a bath of 300 K CO_2 molecules. We use high-resolution transient IR absorption to probe the energy transfer. Collidine was chosen for this study because it expands on the previous experiments on highly vibrationally excited pyridine, 2-methylpyridine (picoline) and its isomers, and 2,6-dimethylpyridine (lutidine). Table 3.1 lists the properties of these vibrationally excited donors considered here, following λ=266 nm light. The addition of a third methyl group increases the number of vibrational modes, the initial energy, and the vibrational state density.

Table 3.1: Properties of highly vibrationally excited species compared in this study

Species	Pyridine	Picoline	Lutidine	Collidine
Structure		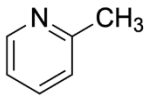	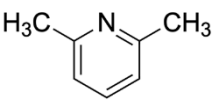	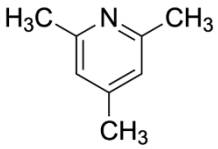
k_{LJ}[a]	7.0	7.4	7.9	8.8
Number of Modes	27	36	45	54
E_{vib} (cm^{-1})[b]	37930	38268	38354	38552
Effective T_{vib} (K)[c]	2875	2325	2080	1870
State Density	6×10^{13}	3×10^{17}	9×10^{19}	3×10^{20}

a) Lennard-Jones rates calculated the constants for collidine of $\sigma = 0.754$ nm and $\frac{\epsilon}{k_b} = 553\ K$ and CO_2 of $\sigma = 0.450$ nm and $\frac{\epsilon}{k_b} = 190$ K.
b) Vibrational energy is the sum of the thermal energy and the photon energy
c) Effective temperature at which the average energy equals the initial energy of the photoexcited molecules.

Highly vibrationally excited donor molecules with more vibrational modes have larger state densities. These experiments operate at internal energies where the vibrational state density is in a quasi-continuum, $\geq 10^7$ states per cm^{-1}, leading to nearly continuous ΔE values, figure 1a. Previous experiments from the Mullin group have identified a correlation between the energy dependence of the vibrational state

density and the P(ΔE). When the highly vibrationally excited donor molecule undergoes a collision, the molecule changes its vibrational state. Fermi's golden rule describes the transition rate from an initial state to a final state because of a perturbation. In the case of highly vibrationally excited molecules with a quasi-continuum there is a continuous distribution of vibrational states that are available for the donor molecule to enter and the collision itself can be considered a perturbation to the system. This is the basis for the Golden Rule Excitation Transfer in Collisions of High ENergy molecules (GRETCHEN) model.[10] In the GRETCHEN model for collisions where the $\Delta E >$3000 cm^{-1} the P(ΔE) and the vibrational state density decays are exponential. These can be fit to an exponential decay and then the slope of each decay,β, are correlated to each other. For CO_2 as a collider gas a linear relationship between the molecules of varying initial state density and P(ΔE) has been observed, shown in figure 3.1b.[54]

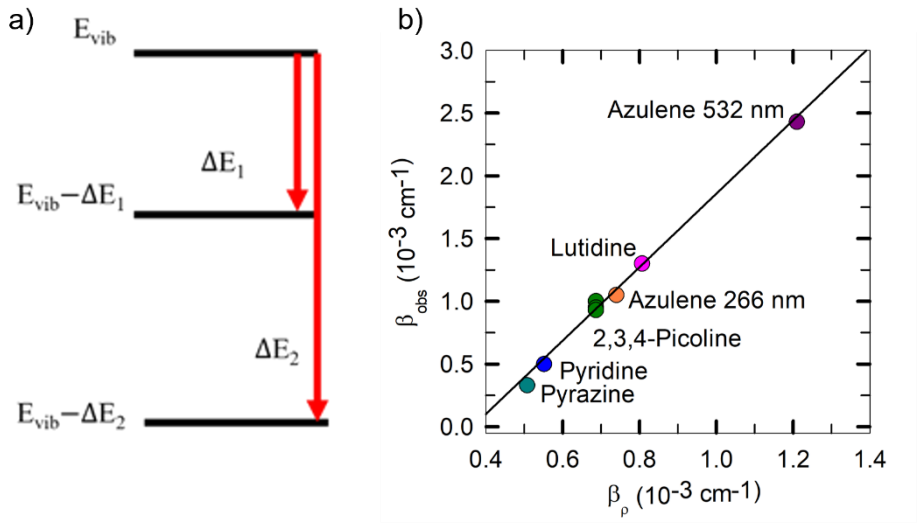

Figure 3.1: a) Schematic for collision induced relaxation of highly vibrationally excited molecules at an initial vibrational energy. b) Correlation of β-parameters for P(ΔE) and the state densities for a series of highly vibrationally excited molecules with a CO_2 bath.

To characterize the P(ΔE) and to further test the GRETCHEN model, translational and rotational energy gains of CO_2 after collisions with collidine are collected. The integrated appearance rate of scattered CO_2 and the depletion rate of thermally populated CO_2 are reported.

3.2 Experimental

3.2.1 Excitation of the Collidine Donor

The experiments were performed using a high-resolution transient IR absorption spectrometer described in chapter 2. The key aspects are described here. A 10 Hz Nd:YAG laser system (Continuum) was used to optically excite gas-phase collidine with λ=266 nm light. High-resolution, continuous wave (cw) IR light was used to measure the transient absorption of individual CO_2 rotational states. A (1:1) mixture of collidine and CO_2 was introduced to a 3-m flowing-gas collision cell and the total pressure was kept at 5-10 mTorr. The UV excitation and IR probe beams were propagated collinearly through the cell.

Photoexcitation of collidine with λ=266 nm light is followed by radiationless decay to the ground electronic state with a quantum yield near unity. The internal conversion lifetime is than 10 ps, based on the photophysics of pyridine and its methyl derivatives.[55,56,65–67,57–64] The vibrationally excited collidine has an energy of $E_{vib} = 38552\ cm^{-1}$ based on the photon energy and the thermal vibrational energy, shown in Equation 3.1.

$$Collidine(300\ K) + h\nu(266\ nm) \rightarrow Collidine(E_{vib} = 38552\ cm^{-1}) \qquad (3.1)$$

The repetition rate of the excitation pulses was reduced to 1 Hz using an external mechanical shutter, the beam diameter was 7 mm, and the UV power was kept below 1.5 mW/cm^2 to avoid multiphoton excitation and limit the fractional concentration of excited collidine to less than 10% of the total concentration.

3.2.2 Detection of CO_2 Collision Products

The excited collidine undergoes deactivating collisions with CO_2, as shown in Equation 3.2.

$$Collidine + CO_2(296\ K) \rightarrow Collidine(E'_{vib}) + CO_2(00^00, J, v) \qquad (3.2)$$

Here, E'_{vib} is the vibrational energy of collidine following the collision, J is the rotational state of CO_2, and v is the velocity vector component parallel to the IR probe laser propagation axis.

Two different IR probe lasers were used to measure transient IR absorption for individual rotational states of CO_2. The first method used A Pb-salt diode laser with output at $\lambda = 4.4\ \mu$m to probe one-quantum absorption using the ν_3 mode, as shown in Equation 3.3.

$$CO_2(00^00, J, V) + h\nu(\lambda{\sim}4.4\ \mu m) \rightarrow CO_2(00^01, J-1, V)\ for\ J \geq 58 \qquad (3.3)$$

The diode was used to probe CO_2 states with $J \geq 58$. The spectral resolution of the diode laser is $\Delta\nu_{IR} = 4 \times 10^{-4}$ cm^{-1}. There were transitions probed with a mid-IR OPO (Aculight) and a spectral resolution of $\Delta\nu_{IR} = 3 \times 10^{-5}$ cm^{-1}. The combination band at $\lambda = 2.8\ \mu$m was used to probe thermally populated CO_2 rotational states with $J \leq 50$, as shown in Equation 3.4.

$$CO_2(00^00, J, V) + h\nu(\lambda{\sim}2.8\ \mu m) \rightarrow CO_2(10^01, J \pm 1, V)\ for\ J \leq 50 \qquad (3.4)$$

After passing through the collision cell, the IR probe beam was sent through a monochromator (Laser Photonics) and to a liquid-nitrogen cooled InSb detector (Teledyne Judson Technologies) with a 300 ns rise time amplifier (Perry Amplifier). Transient absorption signals were typically averaged for 60-100 laser pulses on a 400 MHz oscilloscope (LeCroy) and transferred to a computer using LabVIEW code.

The IR probe laser wavelength was controlled through active feedback. A small portion of the IR beam was directed through either a CO_2 reference cell or a Fabry-Perot etalon and then detected with a second InSb detector and amplifier. The reference signal was sent to a lock-in amplifier and the error signal corrected deviations in the IR output wavelength. Line-center measurements were performed with the IR probe laser locked to line center of a CO_2 transition. Doppler-broadened line profiles were collected by measuring transient absorption signals at ~30 discrete IR frequencies. For these measurements, the IR wavelength was locked to an etalon fringe and the etalon was sequentially tuned across a line profile with an external voltage.

The time between collisions was 6-8 μs for the pressures used in these experiments. Nascent CO_2 populations were measured by collecting transient signals at 2 μs (or less) after the UV excitation pulse which is in the single collision regime. Prior to use, collidine was purified through multiple freeze, pump, thaw cycles. Research grade CO_2 (Airgas >99%) was used directly.

3.3 Results and Discussion

3.3.1 Translational and Rotational Energy Gains of Scattered CO_2 Products

Figure 3.2a shows the transient absorption signals for $CO_2(00^00)$, $J = 2$) at line center. The negative going signal shows net population loss from the CO_2 J=2 state after collisions with the highly vibrationally excited collidine. Figure 3.2b shows the transient absorption signals for $CO_2(00^00)$, $J = 74$) at line center. The positive going signal shows net population gain for CO_2 J=74 state after collisions with the highly vibrationally collidine. The Doppler-broadened line profile is shown at $t = 2\mu s$ for CO_2 $J = 2$ in figure 3.2c. The Doppler-broadened line profile is shown at $t = 1\ \mu s$ for CO_2 $J = 74$ in figure 3.2d. The time for the Doppler profiles was determined by when the transient absorption signals begin to curve. For the appearance of CO_2 $J = 74$ state the curvature starts much earlier than the depletion of the CO_2 $J = 2$ state. The time reported is half the time where curvature is seen to ensure that scattered CO_2 were from a single collision with highly vibrationally excited collidine.

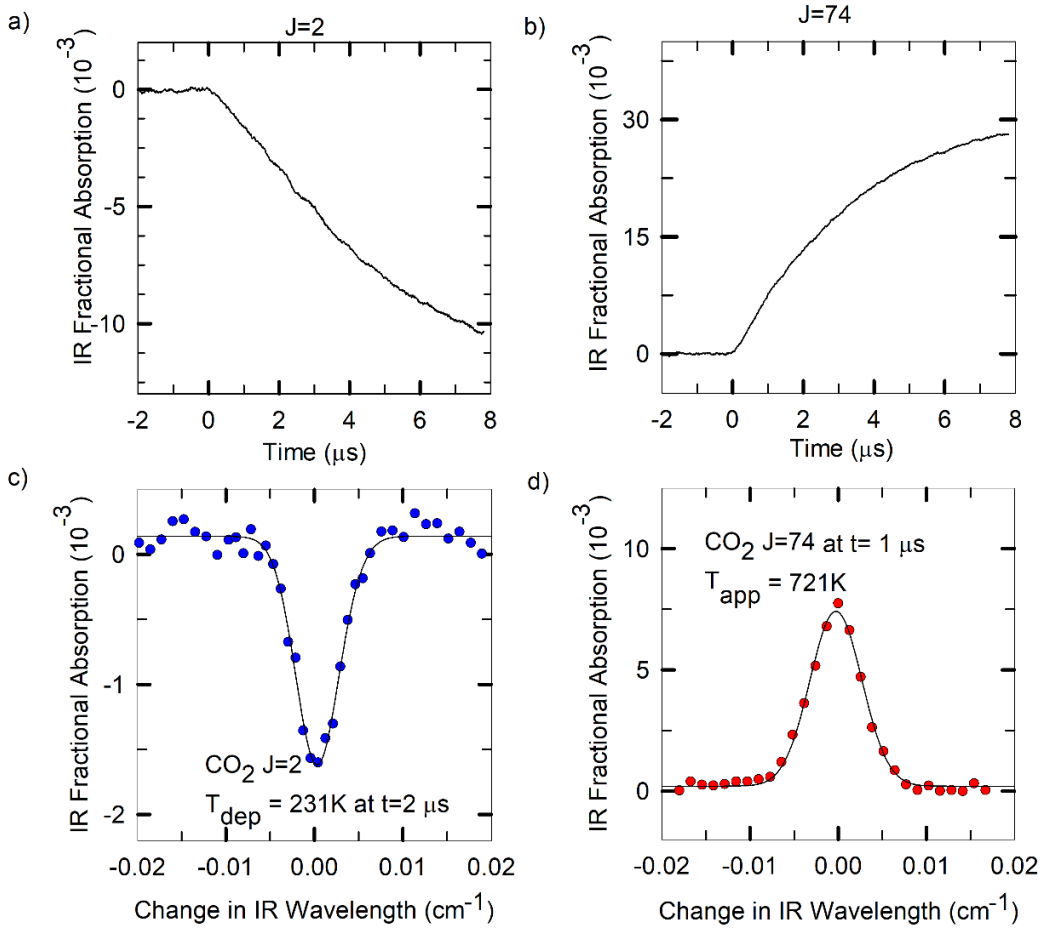

Figure 3.2 Transient absorption signal and Doppler-broadened line profiles for both appearance and depletion. a) Depletion from the CO_2 J=2 at $t = 2\,\mu s$. b) Appearance of the CO_2 J=74 state at $t = 1\,\mu s$. c) Doppler-broadened line profile of J=2 with a depletion temperature of 231 K. d) Doppler-broadened line profile of J=74 with an appearance temperature 721 K.

The translational temperatures of scattered CO_2 molecules was determined by fitting to a 4-parameter single Gaussian. From the Gaussian fits, the appearance and depletion translational temperatures were determined using $T_{trans} = \frac{m_{CO_2}c^2}{8k_B \ln(2)}\left(\frac{\Delta\nu_{obs}}{\nu_o}\right)^2$. Where m_{CO_2} is the mass of CO_2, c is the speed of light, k_B is the Boltzmann constant, $\Delta\nu_{obs}$ is the full-width at half-maximum of the Gaussian fit, and ν_o is the line center IR transition frequency. The CO_2 rotational states with J<8 show net depletion across

their Doppler-broadened line profiles. The depletion temperatures were T_{dep}= 231±25 K for J=2, 211±25 K for J=6, and 198±24 K for J=8. The CO_2 rotational states with J=50-78 show net appearance of across their Doppler-broadened line profiles.

For CO_2 rotational states $J = 22 - 40$ both appearance and depletion were observed. Figure 3.3a shows the transient absorption signal at line center for CO_2 J=22. Net depletion is observed at line center. Figure 3.3b shows the Doppler-broadened line profile of J=22 at $t = 4\ \mu s$, where appearance is seen in the wings of the profile. The low signal to noise levels results from comparable number densities of molecules leaving the $J = 22$ state and those entering as collision products. A similar fitting procedure was followed for these Doppler-broadened line profiles. The only difference was that to fit both the appearance and depletion portions of the profile a sum of two Gaussians was used. The fitting was done with a constrained fit where the depletion temperature was set to T_{dep}=250 K and the appearance temperature was varied between T_{app}=350-575, leading to an appearance temperature of T_{app}=440±100 K.

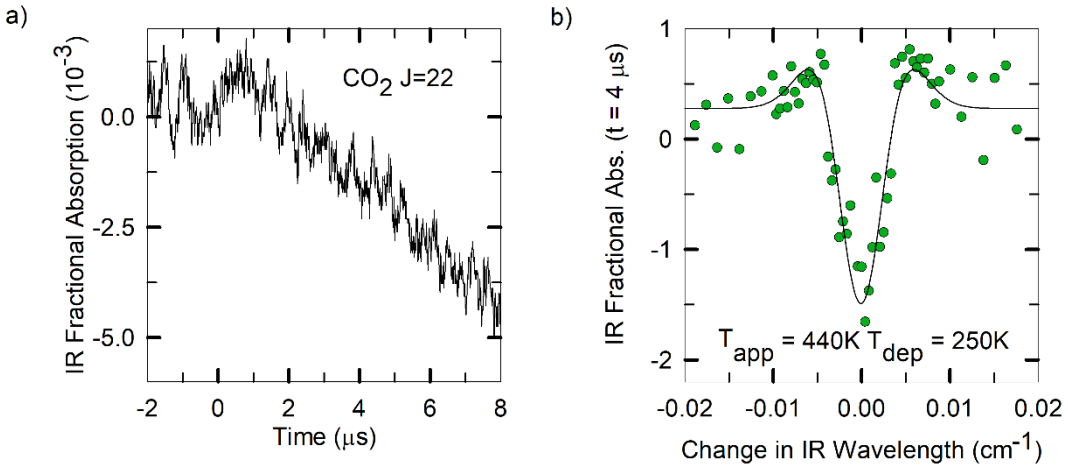

Figure 3.3 a) Depletion transient at linecenter for CO_2 J=22. b) Doppler-broadened line profile where both appearance and depletion are present. The appearance and depletion temperatures are similar leading to lower transient IR signals.

Figure 3.4 shows the measured nascent translational temperatures for CO_2 rotational states J=2-78. The appearance temperatures start CO_2 $J = 22 - 40$ are near 350 K where both appearance and depletion present in the profiles. The appearance translational temperatures increase monotonically up to an appearance translational temperature near T_{app}=900 for $J = 78$. The increase in appearance translational temperature is correlated to the recoil velocity that the scattered CO_2 molecules have. When the thermal CO_2 molecule collides with the highly vibrationally excited collidine the energy transferred involves a large ΔE and the collision is impulsive. The appearance translational temperatures are shown in table 3.2 for both lab frame and center-of-mass frame.

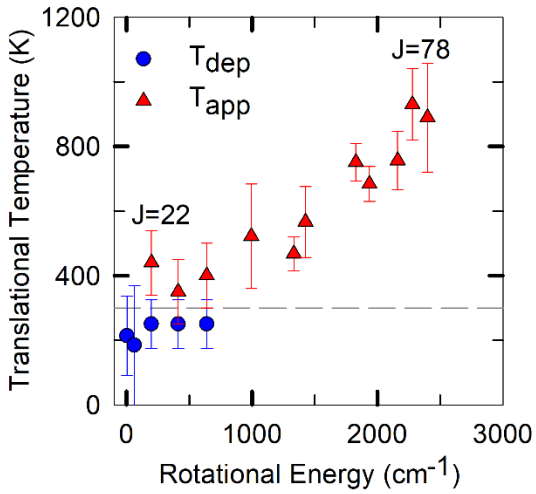

Figure 3.4 Depletion and appearance lab frame translational temperatures for the scattered CO_2 states. The gray dashed line is at 300 K.

Table 3.2: Translational temperatures in lab frame and center-of-mass (com) frame for CO_2-collidine collisions.

CO_2 J State	E_{rot} (cm^{-1})[a]	T_{Trans}(lab) (K)[b]	T_{trans}(com) (K)[c]
22[d]	197.4166	440±100	492±106
32[d]	411.9925	350±100	369±106
40[d]	639.6004	400±100	437±106
50	994.1913	522±162	604±172
58	1333.7679	467±53	529±56
60	1426.4153	566±110	664±128
68	1827.9724	750±58	914±62
70	1936.0953	683±54	823±57
74	2161.6091	756±90	923±96
76	2278.9963	929±110	1158±117
78	2399.4680	889±168	1104±179

[a] Rotational Energy from the HITRAN database for $CO_2(00^00)$ in wavenumbers
[b] Translational temperatures in the laboratory frame
[c] Translational temperatures in the center of mass frame are calculated using the Equation: $T_{trans}(com) = T_{trans}(lab) + (T_{trans}(lab) - T_0)\frac{m_{CO_2}}{m_{collidine}}$ where $T_0 = 296\ K$, m_{CO_2} is the mass of CO_2 and $m_{collidine}$ is the mass of collidine.

[d] Translational temperatures for J=22-40 are estimated from a constrained double Gaussian fit with depletion temperatures set at 250K

Our goal was to measure the full distribution of scattered CO_2 molecules. Appearance profiles were quantified for CO_2 rotational states J≥40. For rotational states with J<40, the appearance signals had insufficient signal to noise to acquire accurate population measurements. The nascent rotational distribution is presented in

Figure 3.5 as a semi-log Boltzmann plot. Three rotational distributions were measured, yielding a nascent rotational temperature of T_{rot} =511±106 K at $t = 1\ \mu s$.

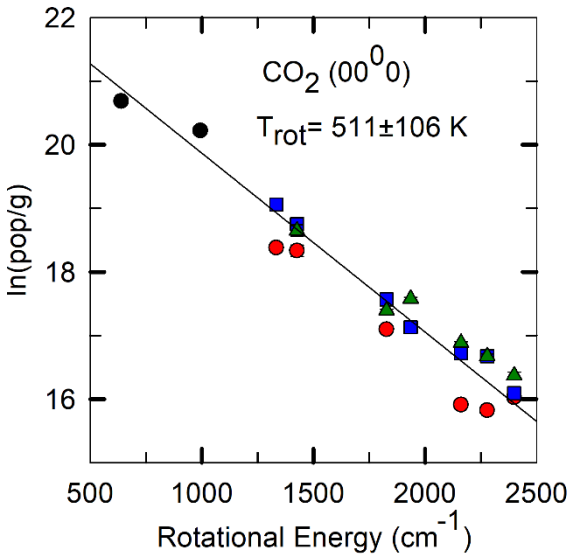

Figure 3.5 Nascent rotational distribution of CO_2 ($00^0 0$) from collisions with highly vibrationally excited collidine.

3.3.2 Energy Transfer Kinetics of Highly Vibrationally Excited Collidine and CO_2

Energy transfer rate constants were determined for both the depletion and appearance of CO_2. J-specific energy transfer rate constants for the vibration-to-rotation and translation pathway were determined based on absolute rate measurements and the nascent rotational distribution.

Bimolecular rate constant, k_2^J , for appearance of CO_2 in a particular J state is defined by Equation 3.5.

$$\frac{d[CO_2\ (00^0 0, J')]}{dt} = k_2^J [Collidine(E_{vib})]_o [CO_2(300\ K)]_o \qquad (3.5)$$

Where k_2^J is dependent on the number density of excited collidine, $[Collidine(E_{vib})]_o$, and the initial CO_2 in the collision cell, $[CO_2(300\ K)]_o$. Populations of individual CO_2 states were determined by using known absorption strengths and integrated Doppler-

profiles. The number density of excited collidine was kept around 1×10^{13} molecule cm^{-3} and the CO_2 number density was kept around 2×10^{14} molecule cm^{-3} .

An absolute rate constant was determined using the J=74 state. The k_2^J of J = 74 was measured to be $k_{app} = (8.1 \pm 1.6) \times 10^{-13} cm^3 molecule^{-1} s^{-1}$ as shown in Figure 3.6a. An integrated rate constant can be determined using the measured rotational distribution and Equation 3.6

$$\sum_{J=0}^{J=78} k_2^J = k_2^{ref} \times \frac{(2J+1)}{(2 * ref + 1)} \times \frac{e^{-\frac{E_J}{k_B T_{rot}}}}{e^{-\frac{E_{ref}}{k_B T_{rot}}}} \tag{3.6}$$

Here, k_2^{ref} is the measured appearance rate of J=74, the reference state used. Using the rotational temperature for the scattered CO_2 products of T_{rot}=511 K and extrapolating over CO_2 rotational states up to J=78 leads to an integrated rate constant $k_{int} = (1.0 \pm 0.3) \times 10^{-9} cm^3 molecule^{-1} s^{-1}$. The integrated rate is in good agreement with the calculated Lennard-Jones collision rate of $8.8 \times 10^{-10}\ cm^3 molecule^{-1} s^{-1}$.

The depletion rate constant was measured for the CO_2 J=2 state and determined by Equation 3.7. The key difference between the appearance and depletion rate Equations is the number density of CO_2 for depletion is only dependent on the state that was measured.

$$\frac{d[CO_2(300\ K, J=2)]}{dt} = -k_{dep}[Collidine(E_{vib})]_o[CO_2(300\ K, J=2)] \tag{3.7}$$

The depletion rate constant from the CO_2 J = 2 state was determined to be $k_{dep} = (9.4 \pm 3.0) \times 10^{-10} cm^3 molecule^{-1} s^{-1}$ as shown in Figure 3.6b. With $k_{LJ} \sim k_{dep} \sim k_{int}$ the dominant relaxation pathway for highly vibrationally excited

collidine undergoing collisions with CO_2 (00^00) is the vibration-to-rotation and translation (V-RT) pathway and there is little energy transfer into the vibration-to-vibration (V-V) pathway.

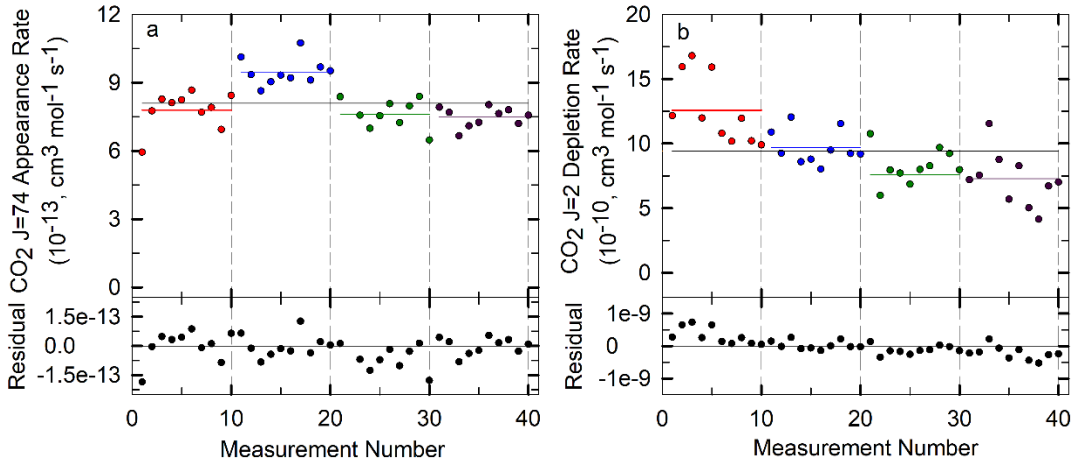

Figure 3.6 Measurements in sets of 10 for the appearance and depletion of CO_2. a) Appearance of scattered CO_2 into the J=74 state. b) Depletion of thermally populated CO_2 in the J=2 state.

3.3.3 Role of Donor Vibrational State Density to Collisional Deactivation

A comparison of the energy transfer data for pyridine and its methylated derivatives shows that increasing the number of vibrational modes (while keeping the total internal energy nearly constant) leads to reduced rotational and translational energies in the scattered CO_2 shown in figure 3.7a,b. Increasing the number of methyl groups present on the donor molecule also increases the number of low frequency torsion modes. The increase in low frequency modes lowers the average energy per mode seen in figure 3.7c. The lower frequency mode enhances the efficiency of the energy transfer in collisions, increasing the appearance rate.[68] For the methylated pyridines the increase in appearance rate is observed as well and shown in figure 3.7d.

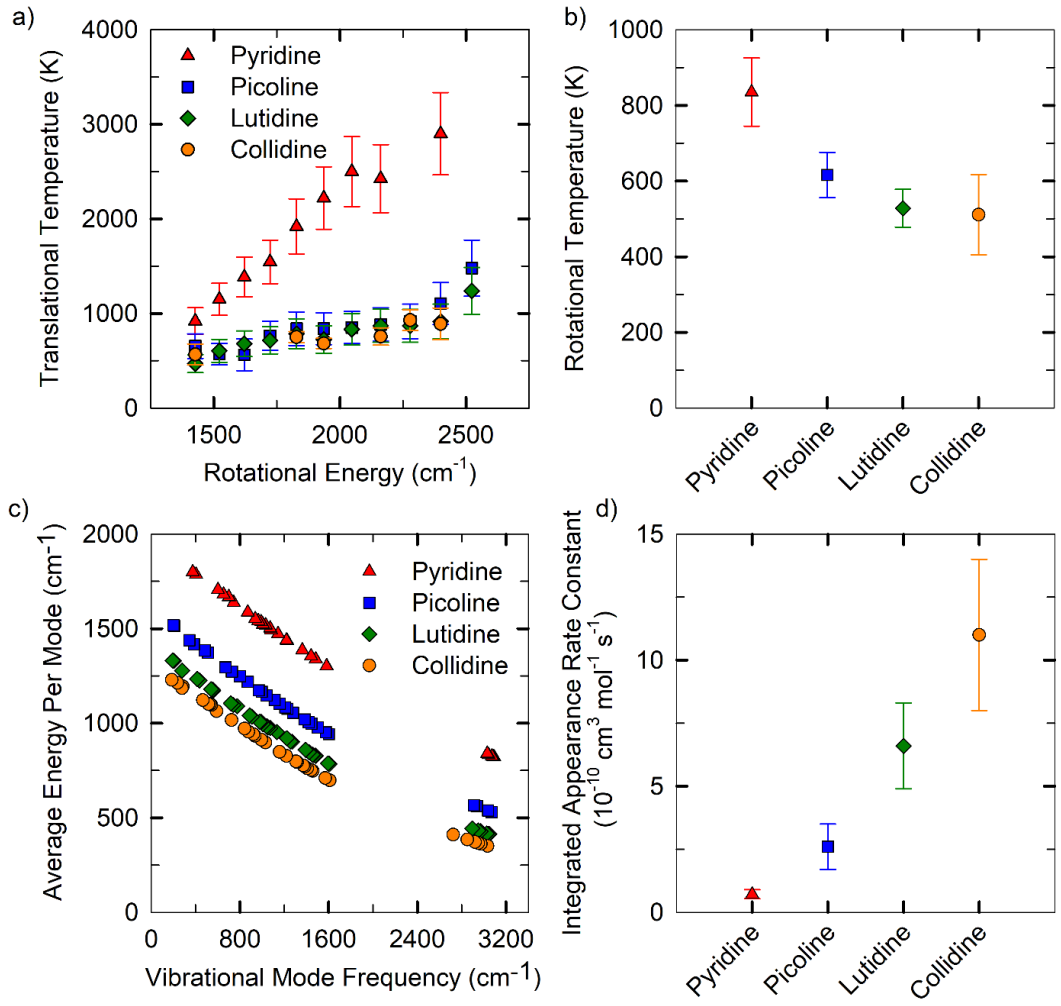

Figure 3.7 Comparison of pyridine and its methyl derivatives. a) Translational energy gains of the scattered CO_2. b) Rotational energy gains of the scattered CO_2. c) Average energy per vibrational mode of pyridine and its methyl derivatives following λ=266 nm excitation. d) Integrated appearance rate for CO_2 J=0-78 following collisions with the donor molecules. Pyridine, picoline, and lutidine were extrapolated from high-J data in reference 54. The error bars represent 25 percent error.

The translational and rotational energy gains of the scattered CO_2 product states is highest for pyridine. With the addition of the first methyl group on the pyridine ring there is a sharp decrease in both energies imparted via collisions with the donor molecule. The addition of subsequent methyl groups shows little effect on the energy gains of the scattered CO_2 products. For the methyl derivatives, picoline had a

rotational temperature of 616 ± 60 K and lutidine had a rotational temperature of 528 ± 50 K. The measured rotational distribution of collidine has a rotational temperature of 511 ± 100 K.

Where each of the methylated donors differ is in the integrated appearance rate constants of the scattered CO_2 products. The enhancement from the methyl group on the appearance rate is clearly seen with the CO_2 scattered via collisions with collidine, which have an integrated appearance rate constant $\sim$15 times that of pyridine. The addition of vibrational modes is effectively vibrationally cooling the molecule with a vibrational temperature of $T_{eff} = 1870\,K$ for collidine which is 1000 K less than pyridine. The low frequency torsion modes are responsible for the increase in the integrated appearance rate. These modes have the highest energy per mode in the highly vibrationally excited donors. The increase in integrated appearance rate constants is also seen between benzene and toluene with several different collision partners.[69]

3.3.4 Probability of Energy Transfer and the GRETCHEN model

The highly vibrationally excited pyridine donors considered here have a quasi-continuum of vibrational states. The state densities were calculated by the Beyer-Swinehart algorithm, which is a direct counting of all possible state combinations at a given internal energy.[70] From Table 3.1, the vibrational state density increases with each successive methylation.

From the state-specific appearance rate constants and the center of mass translational energy, the P(ΔE) was determined. The essential steps include determining the J-specific appearance rate, the center-of-mass translational

temperature, and the final velocity of the CO_2 product state molecule. The $P_J(\Delta E)$ function is shown in Equation 3.8, with v_f the final velocity of the CO_2, μ is the reduced mass of collidine and CO_2, T_{com} is the center-of-mass translational energy after collisions.

$$P_J(\Delta E) = 4\pi v_f^2 \left(\frac{k_2^J}{k_{LJ}}\right)\left(\frac{\mu}{2k_bT_{com}}\right)^{\frac{3}{2}} e^{-\left(\frac{\mu v_f^2}{2k_bT_{com}}\right)} \frac{1}{\mu v_f} \qquad (3.8)$$

The $P_J(\Delta E)$ function was determined for every CO_2 rotational state J = 0-78, and then summed to obtain the full P(ΔE) distribution. Three of the individual P(ΔE) curves are shown in Figure 3.8a. In the largest ΔE region of the graph where ΔE≥3000 cm^{-1} the P(ΔE) curves of the full distribution, Figure 3.8b, and just the CO_2 rotational states used in the rotational distribution are nearly identical. In the ΔE≥3000 cm^{-1} region the P(ΔE) function displays exponential behavior.

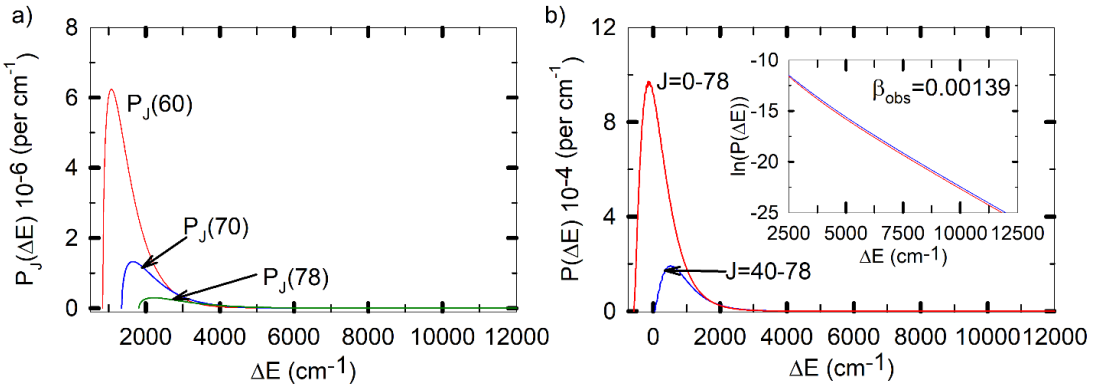

Figure 3.8 Energy transfer distribution function P(ΔE) a) Individual rotational states, $P_J(\Delta E)$ for J=60,70, and 78. b) Sum of rotational states P(ΔE) curves. The inset shows the P(ΔE) slope depending on the CO_2 states used between ΔE=2500-12000 cm^{-1}. For the P(ΔE) the J=0-78 data was used.

A numerical integration of the P(ΔE) give the average energy lost per collision $\langle E\rangle_d = 250 \pm 50$ cm^{-1}. An IRF study on collidine and CO_2 collisions observed the $\langle E\rangle_d = 340 \pm 20$ cm^{-1} at an average bulk energy of $\langle E\rangle = 25000$ cm^{-1}. The initial

energy of the collidine when excited at λ=*266 nm* is $E_{vib} = 38552$ cm^{-1}. By the time the $\langle E \rangle = 25000$ cm^{-1} multiple collisions have occurred and broadening the P(ΔE) distribution.

As the donor molecule is relaxed via collisions, the ΔE distribution of the state densities is an exponential decay. The slope of the decay, β_ρ, is correlated with decay of the P(ΔE) which is called the GRETCHEN model. In order to test collidine on the GRETCHEN model the decay of vibrational states densities ($\rho(E - \Delta E)$), as shown in Figure 3.9a was taken for ΔE =0-12000 cm^{-1}, and then linearly fit. The slope, β values, of the high energy portion of the $ln(P(\Delta E))$ curve is $\beta_{obs} = 1.39 \times 10^{-3}$ cm^{-1} and the slope of the $ln\big(\rho(E - \Delta E)\big)$ is $\beta_\rho = 8.4 \times 10^{-4}$ cm^{-1}. Comparing the relationship of these slopes to other previously reported donor molecules and CO_2 collisions show an excellent agreement with the linear relationship between the P(ΔE) function for the donor and the state density of the donor molecule after the collision as predicted by the GRETCHEN model, shown in Figure 3.9b.

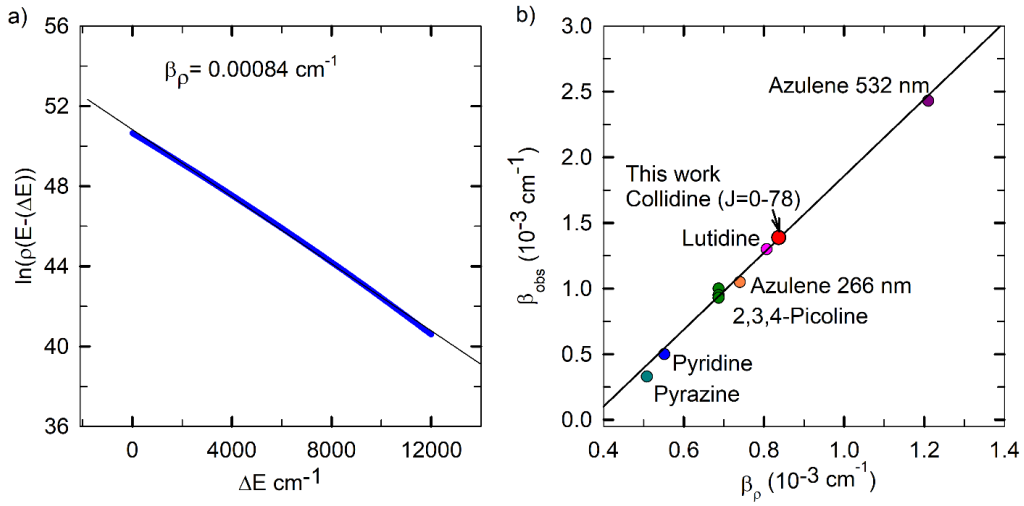

Figure 3.9 a) The decay of vibrational state density for collidine when the $\Delta E \leq 12000$ cm^{-1}. The slope is the β_ρ used in the GRETCHEN model. b) GRETCHEN model of other highly vibrationally excited donors and CO_2 collisions. The current paper is shown in the red circle.

The GRETCHEN model is an empirical model that has been used to demonstrate the correlation between the vibrational state density and the P(ΔE) function, for aromatic donors and a thermal bath of CO_2. The GRETCHEN model can be used to improve future kinetic modelling. Thus far, a large range of vibrational state densities have been studied and the correlation is linear, with the lowest state density being on the order of 10^{12} with pyrazine. It would be interesting to investigate if the linear correlation is observed where donor molecules have vibrational state density that is not a quasi-continuum.

The role of state density and the number of vibrational labs is clear. The collisional energy transfer has a statistical behavior dependent on the size of the donor molecule. The larger molecules have more internal energy and higher vibrational state density but less average energy per vibrational mode. However, these molecules also relax faster due to the increase in low frequency modes and the quasi-continuum of vibrational states that can be the final state after a collision.

3.4 Conclusion

We have investigated the full energy transfer distribution of highly vibrationally excited collidine and thermal CO_2 collisions using high-resolution transient IR absorption. Collidine was the fourth molecule studied in the series of methylated pyridines. As the number of vibrational modes increases with each molecule so does the vibrational state density. The addition of a methyl group to pyridine decreases both the translational and rotational energy gains of the scattered CO_2 molecules. Subsequent methylation of the donor has only a small effect on both translational and rotational energy gains. The overall integrated appearance rate of the highly vibrationally excited donors increases for each additional methyl group added with collidine having the highest observed rate. The integrated appearance rate and the depletion rate indicate that the V-RT pathway is the main relaxation channel. The methyl group adds low frequency modes which increases the efficiency of collisional relaxation. Collidine has the highest state density of pyridine molecules studied thus far. The GRETCHEN model was tested and the linear correlation between the decay in vibrational state density and the $P(\Delta E)$ was observed. This provides both qualitative and quantitative analysis for collisional energy transfer.

Chapter 4: Energy-dependent Photodissociation of SO_2 $\tilde{C}$-state with 220-212 nm light: Transient Product State Spectroscopy and Multireference Electronic State Calculations

Author List: Paul B. Diss, Christopher R. Lukowski, Andrew J. Pommersheim and Amy S. Mullin performed the experiments, Jacek Klos and Millard H. Alexander performed the theoretical calculations

4.1 Introduction

Sulfur dioxide, SO_2, is an important species in the atmosphere of Earth and has been detected in the interstellar medium. SO_2 is found in the troposphere, absorbs solar UV rays from the sun, and when combined with water vapor increases the acidity of rain. After UV absorption, SO_2 can undergo photodissociation, producing both SO and oxygen radicals. SO_2 in the $\tilde{C}(^1B_2)$ state (denoted as $\tilde{C}$-state here) undergoes predissociation with λ = 165 to 220 nm light. It has been proposed that isotopic differences in the predissociation dynamics could explain the observed isotope differences in the early Earth rock record.[71–73] Here, energy-dependent photodissociation experiments at five wavelengths between λ=212 and 220 nm and *ab initio* calculations on the photodissociation dynamics for the main isotope $^{32}S^{16}O_2$ are presented.

Dissociation from the SO_2 $\tilde{C}$-state has been the focus of numerous experimental and theoretical investigations, but a full understanding of the dynamics remains elusive, highlighting the complexity of the $\tilde{C}$ state. Figure 4.1a is taken from Jiang et al. and shows the complexity of the $\tilde{C}$ state,[74] and Figure 4.1b shows a single slice of the $\tilde{C}$ state, calculated by Klos and Alexander for this paper. The $\tilde{C}$-state correlates

diabatically to the SO($\tilde{a}^1\Delta$) + O(^{1}D) products as shown in Figure 4.1b, but coupling with the SO_2 ($\tilde{D}\ ^1A'$) state leads to the lower energy channel of SO($X\ ^3\Sigma^-$) + O(^3P_J) products. The potential energy curves in Figure 4.1b using multireference configuration interaction and include single and double excitations with the Davidson correction (MRCI-F12+Q) at a fixed Jacobian bond angle of 104.3°, the $\tilde{X}$ state equilibrium angle.[75] The gray band in Figure 4.1b corresponds to the range of $\tilde{C}$ state excitation energies used here, and the inset shows that these energies are not sufficient to overcome the dissociation barrier that results from coupling with the $\tilde{D}$ state. The repulsive 2($^3A'$) triplet state, also shown in Figure 4.1b, crosses the $\tilde{C}$-state at a lower energy, and is a candidate for dissociative coupling at lower photon energies. The effect of spin-orbit coupling in the excited electronic states will lead to a lowering of the energy barrier, allowing for dissociation to proceed.

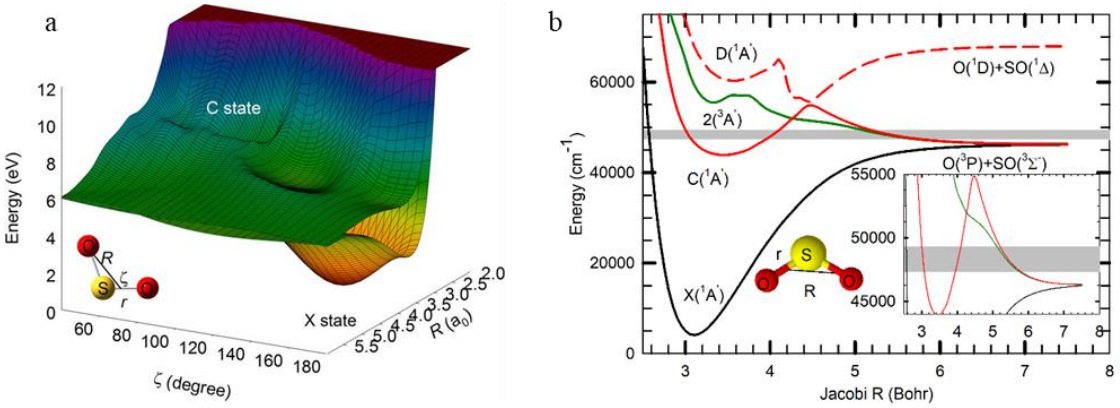

Figure 4.1 a) Full potential surface for the $SO_2(\tilde{X})$ state and the $SO_2(\tilde{C})$ state from Jiang et al.[74] b) Potential energy curves for SO_2 at a fixed Jacobi angle of 104.3°, the equilibrium value for the $SO_2(\tilde{X})$ state. Coupling of the $\tilde{C}$ state with the $\tilde{D}$ state near R=4.4 Bohr results in an energy barrier that is higher than the range of photolysis energies used in the experiments (shown as a gray band). The inset zooms in on the barrier region. A repulsive 2($^3A'$) state crosses the $\tilde{C}$ state below the energy barrier, suggesting that spin-orbit coupling may be involved in the dissociation.

The spectroscopy of the SO_2 $\tilde{C}\,^1B_2 \leftarrow \tilde{X}\,^1A_1$ band and the subsequent dissociation dynamics have been studied with numerous experimental approaches.[14-22] Product state distributions measured at several wavelengths indicate that the dissociation mechanism is wavelength dependent. The vibrational distribution for the SO($^3\Sigma^-$) products becomes inverted as the photolysis wavelength is tuned from 207 nm to 202 nm.[76] Other studies using 193 nm excitation report inverted and bimodal vibrational distributions with varying amounts of rotational excitation.[76–79]

Each SO product rotational state N is split into three J states by spin-rotation coupling. The spin-rotation coupling can be parallel or perpendicular. If the coupling is parallel and vectors can be additive with $J = N + 1$ which corresponds to the F_1 spin-manifold, or subtractive with $J = N - 1$ which corresponds to the F_3 spin-manifold. If the coupling is perpendicular J=N which corresponds to the F_2 spin-manifold. Becker and coworkers showed that spin-polarized SO products favoring F_2 states (with J=N) were observed for photolysis of a jet-cooled sample at the dissociation threshold.[80] Kanamori et al. observed at 193 nm photolysis with an initial 300 K SO_2 sample the F_1 and F_3 states of the SO products were favored.[81]

A simple comparison of the results above is not possible because of experimental differences. Becker et al. used a jet-cooled sample and the SO_2 only had 20 cm^{-1} of product energy. Kanamori et al. used a 300 K sample and λ=193 nm photolysis which corresponds to over 6000 cm^{-1} of product energy. Ebata et al. measured the emission and absorption of jet-cooled SO_2 and 300 K SO_2. Broad spectral features were present at 300 K, but the jet-cooled sample had narrow spectral features.[19] Spin-polarization is also observed in the O atom of the photoproducts. The O atom electronic states are split

by spin-orbit coupling, and spin-polarization is reported to be 91% in J = 2 for E_{pr} = 345 cm^{-1} and 83% in J = 2 when E_{pr} = 740 cm^{-1} for excitation at 217 nm but are statistical at 193 nm.[18, 82,83]

Various coupling mechanisms have been invoked including internal conversion to the $\tilde{X}^1A_1$ state, intersystem crossing to the repulsive $2^3A'$ state, and non-adiabatic coupling with higher energy repulsive states. A single mechanism has not been determined and the mechanism appears to depend on the excitation wavelength.[76,77]

The SO_2 $\tilde{\mathbf{C}}$-state is metastable with a lifetime near the dissociation threshold of 45 ns and drops to 10 ps at λ=193 nm. Photofragment studies find anisotropy values of β = 0 for photolysis at λ=193 nm and between λ=202 nm and 207 nm, consistent with a long-lived dissociative state.[76,83–85] The $\tilde{\mathbf{C}}$-state has several interesting features. Spectroscopic measurements and recent theoretical work show that the ν_3 antisymmetric stretch has an unusually low frequency near 220 cm^{-1}, with large anharmonicity and a double well potential along the ν_3 mode.[75,86–88] The $\tilde{\mathbf{C}}$-state absorption spectrum does not have regular vibronic band progressions and dispersed emission intensities vary with the vibrational symmetry and photolysis wavelength.[89]

The extent to which the $\tilde{\mathbf{C}}$-state is excited before dissociation will depend on the Franck-Condon-active modes and the extent to which those modes are coupled in the $\tilde{\mathbf{C}}$-state. When triatomic molecules predissociate from long-lived complexes, the product rotational distributions are influenced by the molecular geometry at the transition state, vibrational structure, state-coupling matrix elements, and dynamical effects in the exit channel arising from anisotropy of the potential energy surface.[90]

Potential energy curves were calculated by our collaborators Dr. Jacek Klos and Dr. Millard Alexander as a function of molecular geometry and electronic state coupling to give insight into the dissociation process. By measuring the SO product state distributions as a function of $\tilde{\mathbf{C}}$-state internal energy and comparing with the calculations, we learn about SO_2 dissociation near the threshold, including the transition state geometry and the dissociative coupling mechanisms.

The photodissociation experiments used a tunable, pulsed UV light source with output from 220 to 212 nm to initiate SO_2 photodissociation and a high-resolution transient IR absorption spectrometer to measure the nascent SO(v=0) and SO(v=1) product distributions. Doppler profiles for individual SO(v=0) product states were measured at five discrete photolysis wavelengths to determine the initial vibrational energy of the photo-excited SO_2, based on the product velocity distributions and conservation of energy. Nascent rotational distributions were measured for SO(v=0) at five UV wavelengths, yielding the product energy partitioning and its energy dependence.

4.2 Experimental

4.2.1 High-Resolution Transient IR Absorption Spectrometer

A full description was presented in Chapter 2. Here, the key experimental components are summarized. The experiments were performed using a high-resolution transient IR overtone absorption spectrometer coupled to the tunable, pulsed UV-pumped OPO. The main components are a 10 Hz Nd:YAG-pumped OPO, a modulated single-mode IR lead-salt diode laser with high-resolution output at $\lambda \approx 4.4$ μm, and a

300-cm long Pyrex flowing-gas photolysis cell. The SO products were detected with state-resolved transient IR overtone absorption. Light from the OPO and the IR laser was propagated collinearly through the photolysis cell. Both light sources are linearly polarized. The SO_2 pressure was 20 mTorr at 296 K under constant flow conditions and the average time between SO/SO_2 collisions was approximately 3 μs. A mechanical shutter reduced the UV repetition rate to 1 Hz to allow the sample cell to refresh between UV pulses. Transient SO signals were averaged on a digital oscilloscope for 100 measurements and nascent product distributions were determined at t = 0.6 μs. SO_2 ($\tilde{\mathbf{X}} \leftarrow \tilde{\mathbf{C}}$) fluorescence was collected with a photodiode adjacent to the photolysis cell and the UV absorption was monitored simultaneously.

The OPO (Continuum Horizon) has a tunable output from λ=193 nm to 2700 nm with a pulse width of 5 to 7 ns. For the wavelength range used here (212 nm to 220 nm), the spectral resolution was $\Delta\lambda_{UV}$ = 0.05 nm ($\Delta\nu_{UV} \approx 10$ cm^{-1}) and the pulse energy was between 3 and 5 mJ. The IR diode laser has tunable output near $\lambda \sim 4.4$ μm and a spectral resolution of $\Delta\nu_{IR}$ = 0.0003 cm^{-1}. Transient IR absorption signals were collected on an InSb detector with a 300-ns rise-time amplifier. The IR light was modulated at 1 kHz and the laser output wavelength was locked to a fringe of a tunable Fabry-Perot etalon with a lock-in amplifier. Known CO_2 and N_2O transitions were used for locating SO probe transitions.

Transient IR absorption signals were obtained by collecting IR absorption (ΔI) and transmitted (I_t) intensities on a 4-channel 200 MHz digital oscilloscope, averaging over 100 laser shots. Transient signals were transferred to a data acquisition computer using LabVIEW code.

4.2.2 Onset of Photodissociation and Probing SO products

At 300 K SO_2 has highly structured UV absorption.[91] Below the dissociation threshold, SO_2 fluorescence is observed. Figure 3.2a shows the structured SO_2 absorption spectrum between 224 and 212 nm, in steps of $\Delta\lambda$=0.1 nm. Figure 3.2b shows the fluorescence excitation spectra, where the onset of predissociation near 220 nm leads to a sharp reduction in emission intensity.[17] Nascent SO product distributions were measured at discrete UV wavelengths corresponding to five SO_2 absorption peaks, shown by the dashed lines in Figure 4.2a, at λ = 212.0, 213.7, 215.3, 217.2, and 218.9 nm. Action spectra were measured in UV steps of $\Delta\lambda$=0.1 nm. At 296 K, the vibronic transitions either start with the SO_2 vibrationless ground state (000) or from one quantum in the bend (010), corresponding to hot band absorption. The fluorescence of the excited SO_2 was measured, and the predissociation is observed at λ=220.7 nm, this agrees with previous measurements.[17]

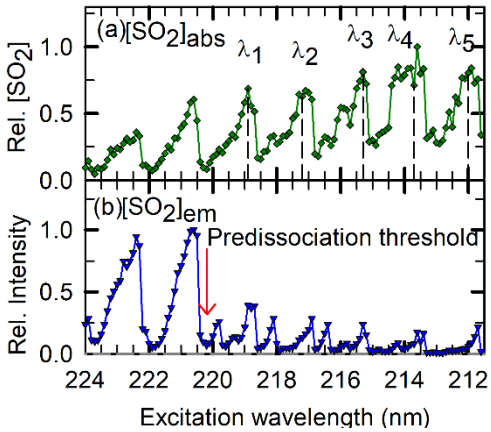

Figure 4.2 a) Absorption spectrum of SO_2 measured in wavelength steps of 0.1 nm. Wavelengths used for SO(v=0) product distributions are λ_1=218.9 nm, λ_2=217.2 nm, λ_3=215.3 nm, λ_4=213.7 nm, and λ_5=212.0 nm b) SO_2 fluorescence excitation spectrum showing the onset of predissociation near 220 nm.

The photolysis experiments involve three steps. The first step is photoexcitation to the $\tilde{\mathbf{C}}$ state, as shown by Equation 4.1.

$$SO_2\left(\tilde{X}\ ^1A_1, 296\ K\right) + h\nu\ (\lambda = 212 - 220\ nm) \longrightarrow SO_2\left(\tilde{C}\ ^1B_2\right) \qquad (4.1)$$

The second step is predissociation from the $\tilde{C}$ state, leading to $SO\left(\ ^3\Sigma^-\right)$ and $O\left(\ ^3P_J\right)$ products, as shown in Equation 4.2.

$$SO_2\left(\tilde{C}\ ^1B_2\right) \longrightarrow SO\left(\ ^3\Sigma^-, v, N, J, vel\right) + O\left(\ ^3P_J\right) \qquad (4.2)$$

Here, v is the SO vibrational quantum number, N and J are the rotational and angular momentum quantum numbers, respectively, and vel is the fragment velocity. The third step is the detection of the SO products using IR overtone absorption probing, as shown in Equation 4.3.

$$SO\left(\ ^3\Sigma^-, v, N, J, vel\right) + h\nu\ (\lambda \approx 4.4\ \mu m) \longrightarrow SO\left(\ ^3\Sigma^-, v+2, N \pm 1, J \pm 1, vel\right) \quad (4.3)$$

IR frequencies and spectral constants for $SO\left(\ ^3\Sigma^-, v\right)$ overtone transitions were reported previously by Burkholder et al.[92]

Transient IR fractional absorption signals for individual SO(v=0) spin-rotation states up to N = 36 were collected following SO_2 photolysis. Figure 3.3a shows the transient IR fractional absorption (at line center) for the SO(v=0) $J = N = 18$ products resulting from photolysis at 215.3 nm. The transient signals are prompt relative to the instrument response time and remain constant for several μs before the photoproducts undergo collisional relaxation, subsequent reactions, and/or diffusion, as shown in the inset of Figure 4.3a. Transient IR absorption features for spin-rotation states are resolved at t = 0.6 μs signals for the SO(v=0) N=18 spin states following photolysis, as shown in Figure 4.3b. The number densities of SO(v) product states were determined

from transient absorption signals using calculated Einstein A coefficients from Dr. Jacek Klos. The Einstein A coefficients are described in Appendix A1.

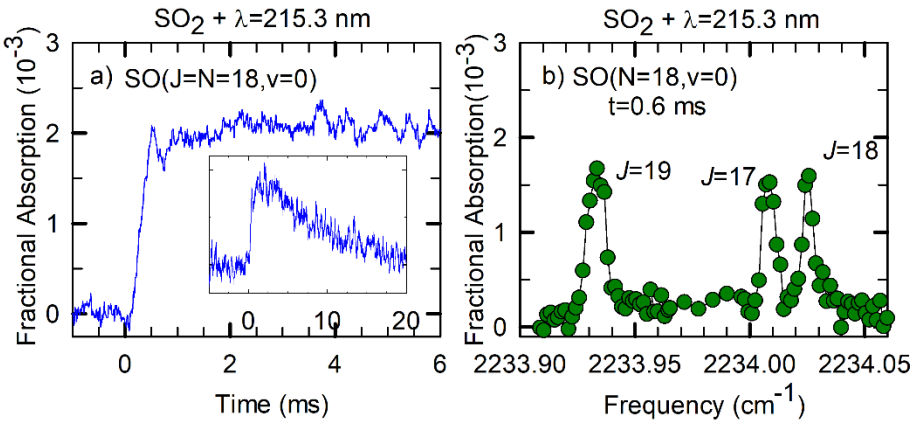

Figure 4.3. a)Transient IR absorption signal for SO(v=0) J = N = 18 following SO_2 photolysis at 215.3 nm. The inset shows the long-time decay. b) Transient IR absorption spectrum for the N = 18 spin-rotation states of SO(v=0) products at t = 0.6 μs following SO_2 dissociation at λ=215.3 nm.

4.3 Results and Discussion

4.3.1 Doppler Profiles of SO(**v**=0) and Total Product Energy

Energy-dependent photolysis studies rely on knowing the SO_2 $\tilde{\mathbf{C}}$-state energy before dissociation. Energy conservation determines the total product energy, E_{pr}, is given by equation 4.4.

$$E_{pr} = E_{rot}(SO_2) + E_{vib}(SO_2) + E(h\nu) - D_0 = E_{int}(SO) + E_{so}(O) + E_{tr} \qquad (4.4)$$

The average SO_2 rotational energy is $E_{rot}(SO_2)$ = 308 cm^{-1} at T=296 K. The SO_2 vibrational energy $E_{vib}(SO_2)$ is either 0 or 518 cm^{-1}, depending on whether the photoexcitation transition starts in the (000) or (010) state of SO_2. The UV photon energy is $E(h\nu)$ and the dissociation energy is D_0=45725.3 cm^{-1}.[80] The combined rotational and vibrational energy of SO is $E_{int}(SO)$, the O-atom spin-orbit energy is

$E_{int}(O)$, and the fragment center-of-mass (COM) kinetic energy is E_{tr}. Photolysis wavelengths of λ=220 to 212 nm correspond to E_{pr} values up to 5400 cm^{-1}. The possible $O(^3P_J)$ energies are $E_{int}(O)$=0 cm^{-1} for J = 2, 158 cm^{-1} for J = 1, and 227 cm^{-1} for J = 0.[93] Previously, O atom product yields were reported as 91% in J = 2 for E_{pr} = 345 cm^{-1} and 83% in J = 2 when E_{pr} = 740 cm^{-1}.[80]

Transient Doppler profiles were measured for individual SO(v=0) product states at five photolysis wavelengths to establish values of E_{pr}. The Doppler profiles depend on the experimental geometry, the angular distribution of the photoproducts, parent velocity distribution, and product relative velocities.[94,95] The photolysis involves a parallel electronic transition, the IR propagation vector is perpendicular to the UV polarization, and the photoproduct angular distribution is isotropic based on the long-lived SO_2 $\tilde{C}$ state. The fitting expressions use an error function formulation to convolute the parent velocity distribution and the product velocities, as described in detail in Refs. 96 and 97.[96,97] The SO Doppler profiles were fit with six possible product velocities, corresponding to two possible initial SO_2 states, either (000) or (010). The O atom was assumed to be in its ground state $^3P_2$ with an E_{int}=0. Transient IR Doppler profiles at t=0.6 μs are shown in Figure 4.4-c for either SO(v=0) F_2 N=8 or N=18 for three photolysis wavelengths, along with the best fit results and the residuals.

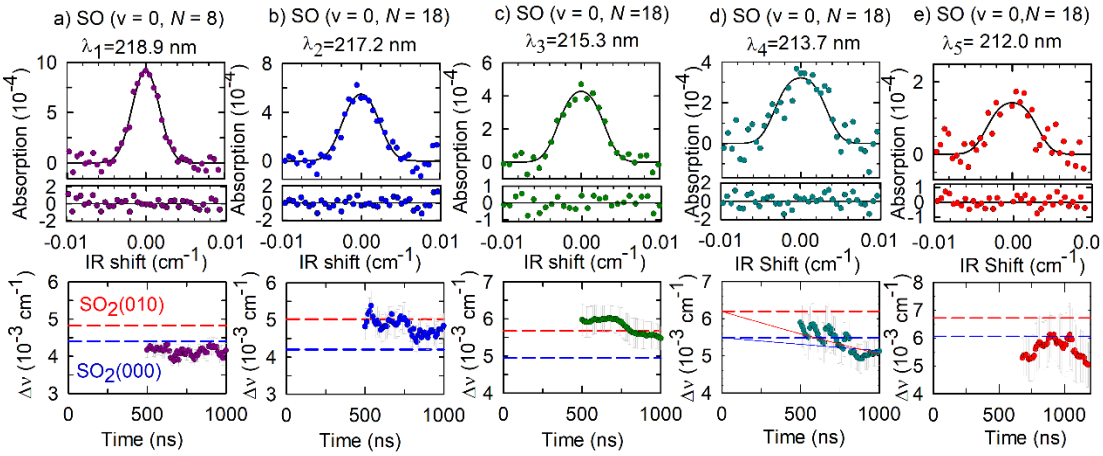

Figure 4.4 a-c) Upper plots show transient IR Doppler profiles of individual rotational states of SO(v=0) at t=0.6 μs for three photolysis wavelengths collected at 20 mTorr pressure, along with Doppler fitting results (solid lines) and residuals. Lower plots show time-dependent line widths (FWHM) for the line profiles. The blue and red dashed lines indicate line widths associated with photoexcitation of SO_2 in the ground vibrationless state (000) and the excited bend state (010), respectively. The data for d) and e) were collected at higher pressures, and the red and blue curves extrapolate to line widths for the hot band or ground state absorption.

The data in Figure 4.4 show that SO_2 is photoexcited at λ_1=218.9 nm from the (000) state and that at λ_2=217.2 nm and λ_3=215.3 nm, photoexcitation is initiated from the SO_2 (010) state. Doppler profiles of SO(v=0) states for λ_4 and λ_5, are shown in Figures 4.4d and 4.4e, along with the fitting results and residuals. The SO_2 pressure was increased to 60 mTorr for these data to increase signal levels. In the lower plots, the time-dependent FWHM linewidths for λ_4=213.7 nm shows the effect of collisional relaxation and are fit as an exponential decay from t=0 starting with the calculated line width from either SO_2(000) or (010) photoexcitation. The λ_5=212.0 nm time-dependent FWHM linewidths do not show collisional relaxation and indicate that the SO_2(000) state is involved in the λ_5 absorption.

The Doppler profile analysis establishes the values of E_C and E_{pr} at the five photolysis wavelengths and the resulting energies are listed in Table 4.1. The values of E_C and E_{pr} for λ_5 are lower limits, based on the assignment of absorption from SO_2 (000).

Table 4.1 Energies (in cm^{-1}) for SO_2 Photodissociation

Excitation (nm)	$E(h\nu)$	$E_{vib}(SO_2)$[a]	E_C	E_{pr}[b]
λ_1 = 218.9	45683	0	3418	266
λ_2 = 217.2	46040	518	4294	1141
λ_3 = 215.3	46447	518	4700	1547
λ_4 = 213.7	46816	518	5047	1895
λ_5 = 212.0	47170	0 [c]	4904 [c]	1752[c]

[a] Based on analysis of time-dependent Doppler line widths.
[b] Using $E_{int}(O) = 0$.
[c] Lower limits to E_C and E_{pr} based on assignment of SO_2 (000) absorption.

4.3.2 SO(**v**=0) Rotational Energy Distributions and Spin-Rotation Branching Ratios

Nascent SO(v=0) rotational distributions from SO_2 photolysis were measured as a function of wavelength and are shown in Figure 4.5 as semi-log plots. Each distribution was measured at least three times. Nascent populations were determined from transient signals at t = 0.6 μs and included contributions to Doppler line broadening. Figure 3.5 also shows the SO_2 absorption spectrum along with photolysis wavelengths, internal energies in the $\tilde{C}$-state (E_C), and total product energies (E_{pr}). At low photolysis energies, the SO(v=0) products are limited to low rotational states by the small values

of E_{pr} but as the $\tilde{C}$-state energy increases, the SO(v=0) products are formed in higher rotational states and the distributions broaden for each SO spin-rotation manifold.

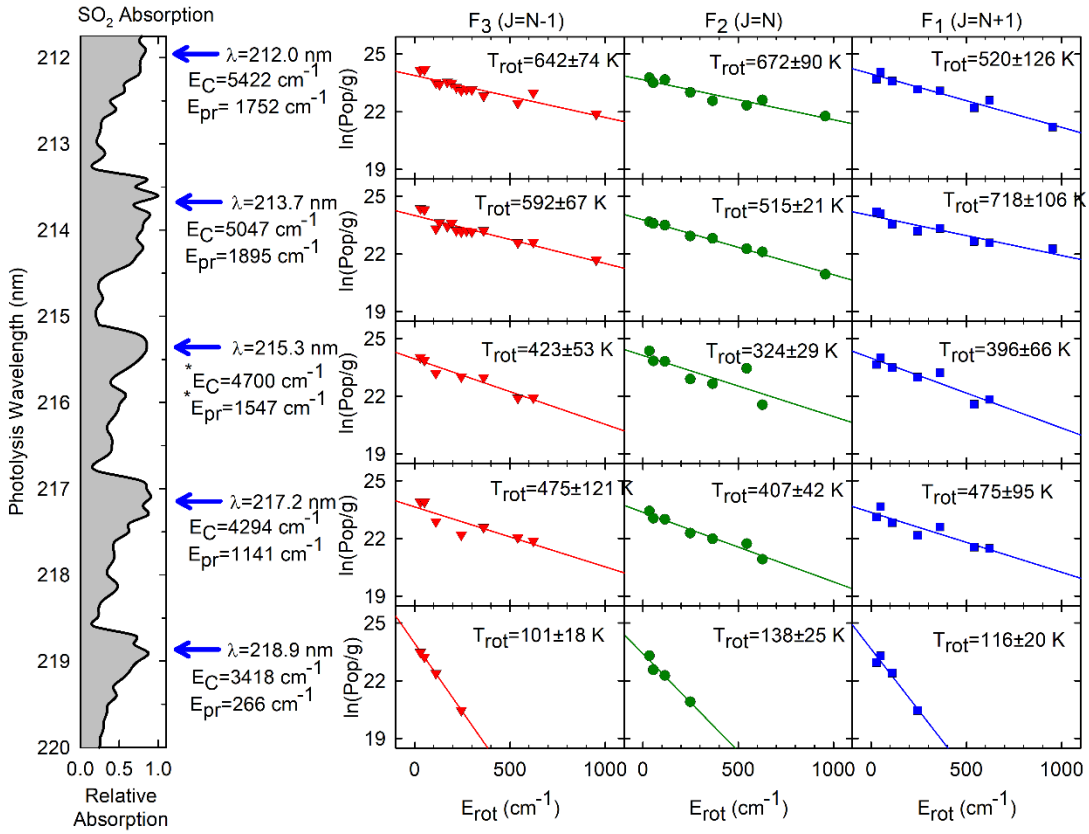

Figure 4.5. Nascent rotational distributions of SO(v=0) F_1, F_2, and F_3 states from SO_2 $\tilde{C}$ state photolysis at five UV wavelengths. The SO_2 absorption spectrum is shown on the left, with the excitation wavelengths, internal energy in the $\tilde{C}$-state (E_C) and the total product energy (E_{pr}).

Nascent rotational temperatures, T_{rot}, for the SO(v=0) products were determined from the slopes of the semi-log plots. Figure 4.6a compares the nascent rotational temperatures as a function of the available product energy for the three spin-rotation manifolds. Within uncertainty, no substantial differences are seen among the spin-rotational manifolds at a given photolysis energy. The rotational temperatures generally increase as a function of the total product energy.

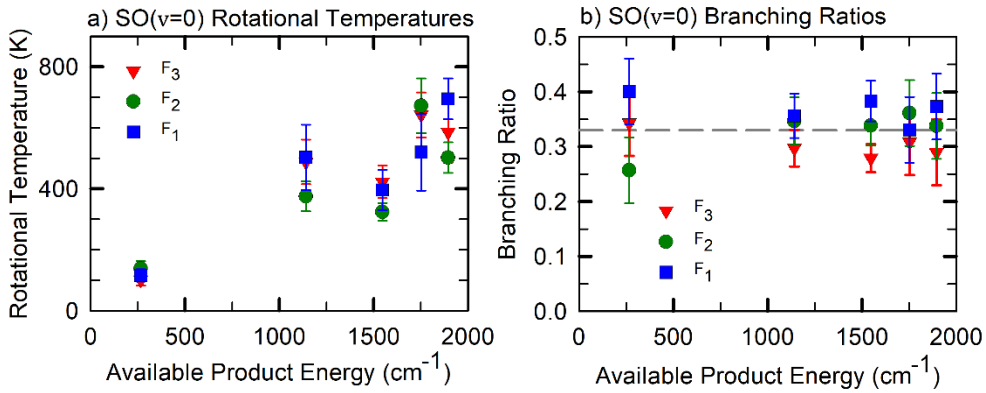

Figure 4.6. (a) Nascent rotational temperatures of SO(v=0) products, based on rotational distributions shown in Figure 3.5. (b) Branching ratios for the SO(v=0) spin-rotation manifolds.

The branching ratios for the SO(v=0) spin-rotation manifolds were determined using the rotational temperatures and number density measurements for each spin-manifold. Figure 4.6b shows that the product branching ratios are approximately one-third for the three spin manifolds and independent of the available product energy, for the photolysis range studied.

Our results differ from those reported by Becker et al. and Kanamori et al.[77,80] Becker et al. reported spin-polarization of the SO product states for photolysis near the dissociation threshold, but this experiment was performed from a jet-cooled sample with only 20 cm^{-1} of total product energy. Threshold photolysis at 296 K increases the available product energy and leads to a lack of spin-rotation polarization. In other experiments by Kanamori et al. using λ=193 nm and a 296 K sample, the product energy is 6,000 cm^{-1} and the SO products are observed, although with different manifolds found relative to the threshold studies. This comparison shows that the product state distributions depend on the $\tilde{C}$-state energy, which directly results from the

thermal energy in the $\tilde{X}$-state and the photolysis wavelength. As the photolysis energy increases, more electronic states are available that can lead to dissociative coupling.

4.3.3 Product Energy Partitioning

The product energy partitioning between rotation and translation was determined using the rotational energy distributions and the total product energy. The average total SO(v=0) rotational energy, E_{rot}^{tot}, is determined using the observed nascent rotational temperatures and Equation 4.5.

$$E_{rot}^{tot} = \sum_J \left(N_J / N_{tot}\right) E_{rot,J} = \sum_J \left(g_J e^{-E_{rot,J}/k_B T_{rot}} / Q_{rot}\right) E_{rot,J} \qquad (4.5)$$

Here, g_J is the degeneracy of the J rotational state, $E_{rot,J}$ is the energy of the J state, k_B is the Boltzmann constant, and Q_{rot} is the rotational partition function at T_{rot}. The average total translational energy is based on the conservation of product energy, as shown in Equation 4.6.

$$E_{tr}^{tot} = E_{pr} - E_{rot}^{tot} \qquad (4.6)$$

Figure 4.7a shows the rotational and translational energy partitioning for the SO(v=0) products as a function of E_{pr}. The slopes yield the fraction of product energy in rotation and translation, respectively; these values are plotted in Figure 4.7b as a function of product energy. We find that 79% of the product energy is in translation and 21% is in SO rotation, and that this ratio is the same for the three SO(v=0) spin-rotation manifolds. The observation that the photodissociation products have nearly 4-fold more translation than rotation is consistent with dissociation from a linear transition state. The equilibrium bond angle of the SO_2 $\tilde{C}$-state is 104.3°, and these data

indicate that the SO_2 bond angle must open up before dissociation occurs. The energy partitioning between translational and rotational is an upper limit. If the O atom product is excited, less energy will be in the translational energy of the photolysis products.

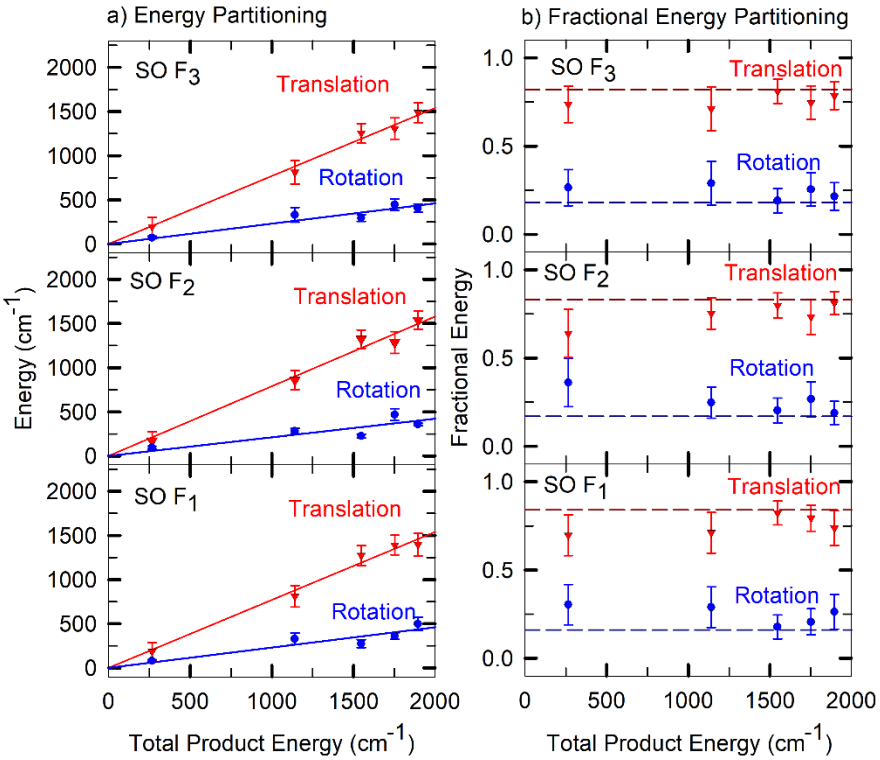

Figure 4.7. Energy partitioning of the SO(v=0) spin manifolds as a function of total product energy. (a) Product energies are partitioned approximately four-fifths in translation (red triangles) and one-fifth in rotation. (b) The three SO spin-rotation manifolds have similar fractional energy partitioning.

4.3.4 Ab Initio Calculations of SO_2 Electronic States

The predominance of translational energy in the SO(v=0) products indicates that the SO_2 transition state configuration is linear, or nearly so. The overall similarity in energy partitioning for the three spin-rotation manifolds of SO indicates that the electronic coupling matrix elements for predissociation are not strongly dependent on the SO spin-rotation coupling. The predominance of product translational energy over

rotation also highlights the impulsive forces present in the dissociation transition state and points to a repulsive state as a likely candidate for the non-adiabatic coupling that leads to dissociation.

Figure 4.8a shows idealized SO_2 potential energy curves at two fixed SO_2 Jacobi angles. The inserts show the potential energy curves in the region of dissociation occurs. The experimental energies in this paper are shown in gray. The top curves have fixed bond angle of θ=104.3°, corresponding to the equilibrium bond angle of the $\tilde{X}$-state. The lower curves have a fixed bond angle of θ=179.5°, based on the observed SO product energy partitioning. The range of experimental energies is shown in gray. The energies have been scaled to the minimum in the $\tilde{C}$-state for θ=104.3°, where the Franck-Condon overlap allows for excitation from the ground electronic state. The resulting barrier to dissociation in the bent geometry lies higher in energy than the region probed in this study. Increasing the Jacobi angle to θ=179.5° results in a decrease in barrier height and shows that dissociation can occur via coupling to the repulsive triplet state ($2^3A'$) shown in green. However, the barrier energy is still higher than the experimental photolysis energy.

Additional calculations were performed that included spin-orbit coupling for both geometries. Figure 4.8b shows the same potential energy curves with the addition of spin-orbit coupling. When the SO_2 is in the bent geometry the energy barrier for dissociation is still too high for dissociation to occur. With spin-orbit coupling and a linear, θ=179.5°, SO_2 geometry the $\tilde{C}$-state and the repulsive $2^3A^{'}$ state interact at a Jacobi distance of 4.2 Bohr, lowering the dissociation barrier such that dissociation will proceed at our experimental energies near the dissociation threshold.

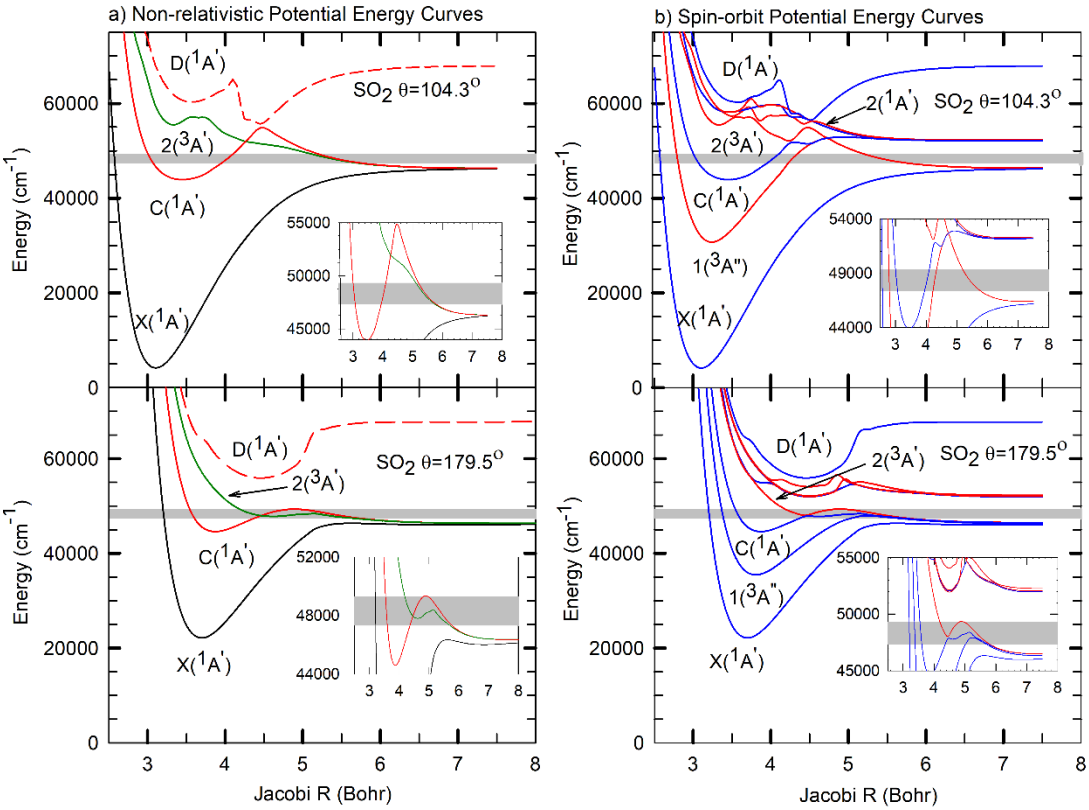

Figure 4.8 a)The potential energy curves for SO_2 dissociation in bent and linear geometries. When the SO_2 is bent dissociation cannot proceed over the barrier. With a relaxed angle, the dissociation can proceed via the repulsive triplet state. b) The potential energy curves for SO_2 with spin-orbit coupling included in the calculation. The $\tilde{\mathbf{C}}$ state interacts with the repulsive triplet state around 4.2 Bohr, lowering the dissociation barrier. The gray shaded area indicates the range of experimental energies scaled to the $\tilde{\mathbf{C}}$ state minimum for the bent geometry in both.

The product energy partitioning in Figure 4.7 and the potential energy curves in Figure 4.8 show that spin-orbit coupling is key to SO_2 $\tilde{C}$-state dissociation for photolysis energies near threshold. We investigated this phenomenon further by performing MRCI calculation of the $\tilde{C}$-state that include spin-orbit coupling and unconstrained geometry as a function of the Jacobi coordinate R. The results are shown in Figure 4.9a, where the $\tilde{C}$-state curve shows evidence of multiple curve crossings. The dissociation barrier height from these calculations is in excellent agreement with the experimental photlysis energies. Figure 4.9b shows that the SO_2 $\tilde{\mathbf{C}}$-state bond angle

undergoes a set of discrete increases prior to dissociation at R values where the electronic state coupling occurs. The calculations show that upon photoexcitation, SO_2 in the **C̃**-state is initially bent with a bond angle near 120° and R=3.2 Bohr. The bond angle opens to a nearly linear until the barrier is reached at R=4.6 Bohr and dissociation occurs. Figure 4.9c shows that the SO product is mainly a spectator in the transition state. These calculations also show that past the transition state the Jacobi angle jumps to 90°, consistent with a T-shaped van der Waals complex of the recoiling SO and O products, not counting any rotation in the SO products.

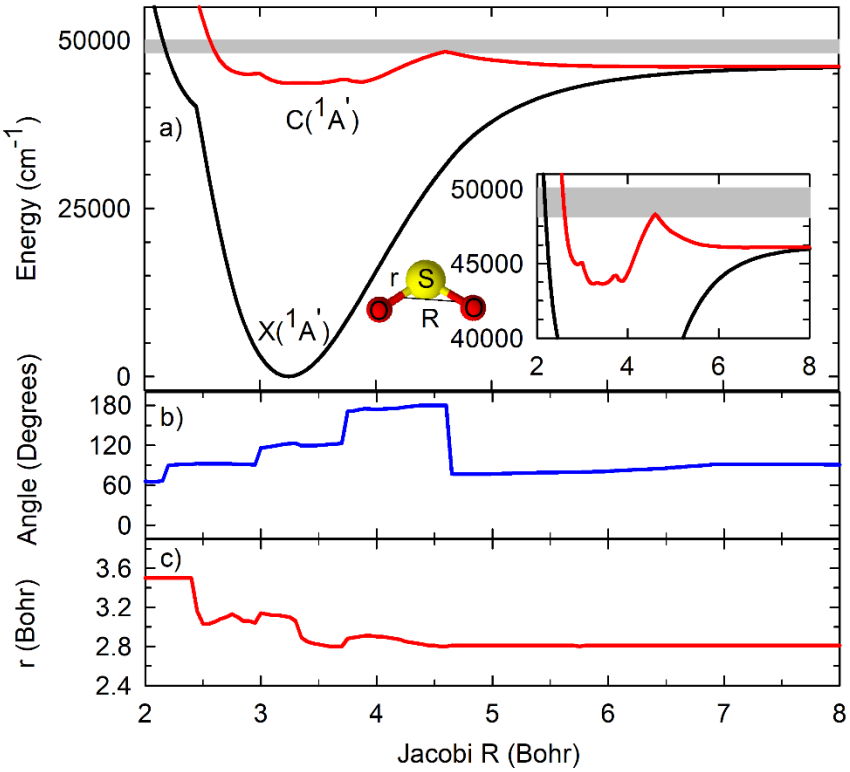

Figure 4.9 a) The minimum energy curve for the SO_2 **C̃**-state dissociation based on the nonadiabatic coupling described in Figure 4.1. The excitation energy range is shown in gray. b) The SO_2 bond angle as a function of the distance R for the minimum energy curve. The SO_2 is bent at the bottom of the **C̃**-state and linear at the barrier. c) The SO bond distance as a function of R for the minimum energy curve. The bond length decreases slightly prior to dissociation.

The SO_2 bond angle opening from bent to near linear underscores the complexity of the $\tilde{C}$-state surface. The photodissociation mechanism of SO_2 has been a topic of research for a while with different groups concluding different mechanisms. Based on results presented here, it is likely that the mechanism will change as the excitation energy is increased. Our data show that near the dissociation threshold at λ=220 nm, SO_2 photodissociation occurs via coupling from a repulsive triplet state and through a close to linear transition state.

4.3.5 Onset of Vibrationally Excited SO Products

Increasing photolysis energy opens new channels for vibrationally excited SO products, which has been observed at λ=193 nm and λ=202-208 nm.[76,77] When the photolysis wavelength was λ=193 nm SO(ν=2) was found to be the most populated. At λ=202-208 nm when the photolysis wavelength was λ=206.71 there was equal population in SO(v=1) and SO(v=2). The vibrational distribution of the SO products changes to SO(v=0) at λ=202.13 nm. The threshold for the SO(ν=1) product channel is at λ=214.8 nm if the absorption starts with SO_2(000); if hot band absorption from SO_2(010) is involved, the threshold is λ=217.1 nm. Action spectra were collected by measuring transient IR absorption signals for individual SO(v=0) product states as the UV wavelength was tuned quasi-continuously in steps of $\Delta\lambda$ = 0.1 nm from 211.5 nm to 221 nm. However, UV action spectra taken for J=6,12, and 18 in the F_2 manifold observed that there was no sudden onset of the vibrationally excited SO(ν=1) state, as shown in Figure 4.10.

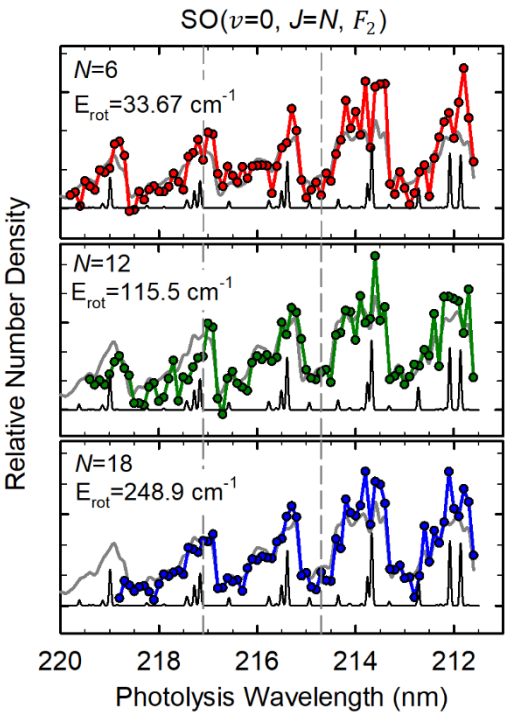

Figure 4.10 Transient IR action spectra (circles) measured at t = 0.6 μs for SO(v=0) F_2 product states resulting from SO_2 dissociation. The grey curve is the relative number density of dissociating SO_2. The theoretical SO_2 vibronic transitions from Kumar et al are shown in black.

Action spectra were additionally collected for the spin-rotation manifolds of SO(v=0) products. Action spectra for the N = 6 and 12 states of the F_1, F_2, and F_3 manifolds are shown in Figure 4.11, along with the scaled parent number density. The action spectra generally track the parent number density, and the only significant deviations are seen at the lowest photolysis energies for the F_1 states that have slightly higher rotational energies than the related F_2 and F_3 states. These data show that the SO(v=1) product channel has a relatively small yield for all three spin-rotation manifolds.

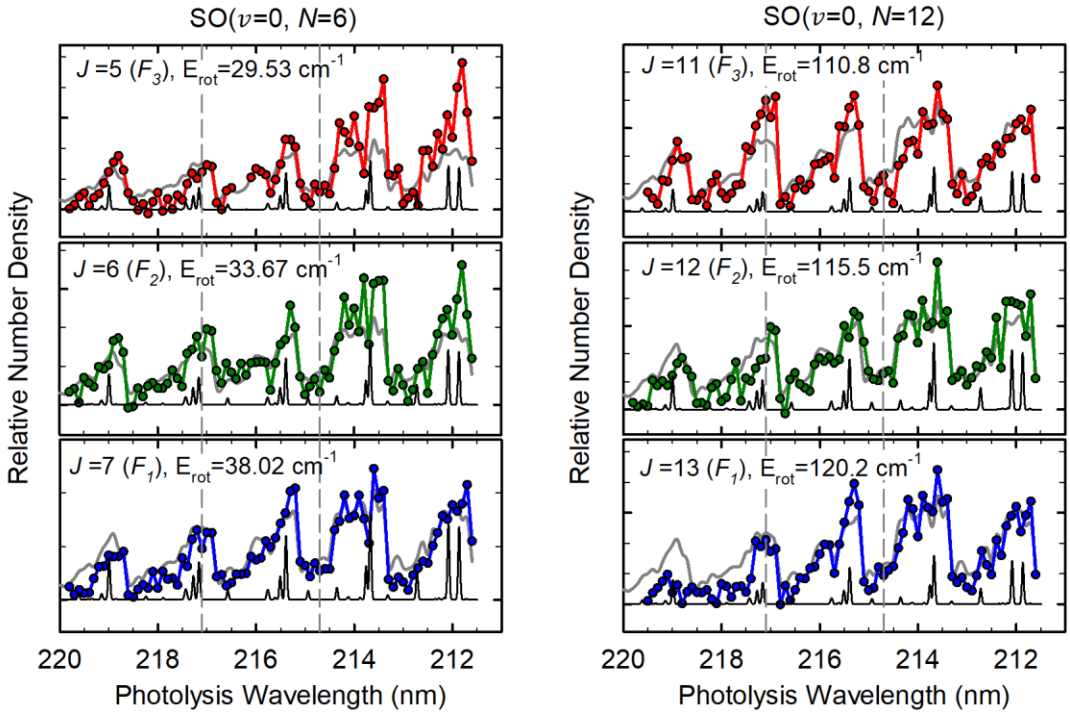

Figure 4.11 Transient IR action spectra at t = 0.5 μs for the F_1, F_2, and F_3 components of the SO(v=0) N = 6 and 12 states as a function of UV wavelength collected in steps of $\Delta\lambda$ = 0.1 nm. The relative number density of dissociating SO_2 molecules is shown in grey and the theoretical absorption spectrum is shown in black.

The spectra in Figures 4.10 and 4.11 do not show significant population changes at the SO(v=1) threshold wavelength(s), indicating that SO(v=1) is a minor product channel over this wavelength range. To check for the presence of SO(v=1) products, transient IR overtone absorption probing was used to measure several SO(v=1) states following SO_2 excitation at 213.7 nm. Figure 4.12a shows the transient absorption signal of SO(v=1) $J = N$ = 4. Absorption intensities for the (v=1) state are smaller than those for the (v=0) state by approximately two orders of magnitude. Number densities for SO(v=1) product states with N = 2 to 14 were determined at t = 0.5 μs and the nascent rotational temperature for the SO(v=1) products is T_{rot} = 165 K, based on the semi-log plot shown in Figure 4.12b. The integrated number density of the SO(v=1)

products shows that the SO(v=1) channel accounts for only 2% of the dissociation products following excitation with 213.7 nm. Furthermore, the energy partitioning for the SO(v=1) product channel includes the vibrational energy of E_{vib}^{tot}=1138 cm^{-1} with approximate rotational and translational values of E_{rot}^{tot}=120 cm^{-1} and E_{tr}^{tot}=640 cm^{-1}. The SO(v=1) products also have substantially more translational than rotational energy.

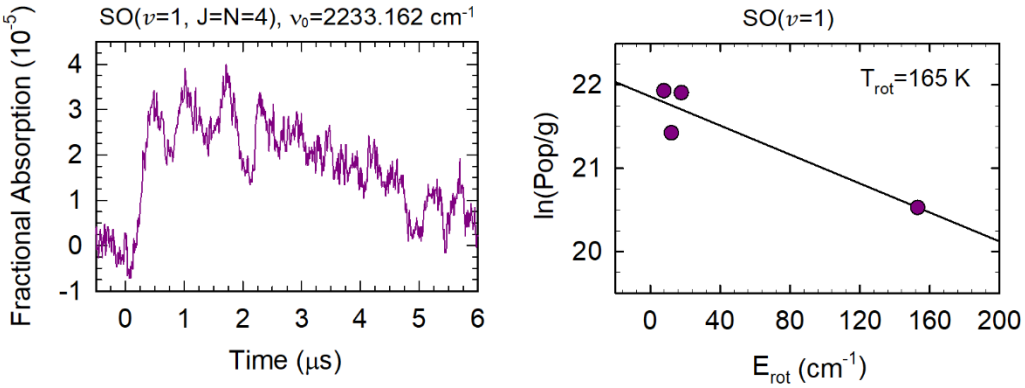

Figure 4.12 a) Transient IR absorption signal of SO(v=1) J = N = 4 products following SO_2 photolysis at 213.7 nm. b) Nascent populations at t = 0.5 μs for SO(v=1) states with J = N = 2, 3, 4, and 14 have a rotational temperature of T_{rot} = 165 K.

4.4 Conclusions

SO_2 photodissociation is a complex process. SO_2 has well-defined vibronic bands, and when excited from a 300 K sample, the SO_2 excited into the C̃ state can come from either the SO_2(000) or (010) state. For 3 of the excitation wavelengths studied the latter is true and there is an additional 518 cm^{-1} of energy available to the products. The additional available energy does not affect the photodissociation process as the rotational temperature increases with increasing excitation energies. For the five excitation energies studied here the energy partitioning after photodissociation favors translational energy by a 4:1 ratio over rotational energy. The preference for translational energy indicates that prior to dissociation the SO_2 becomes near linear. Ab

initio calculations on the SO_2 $\tilde{C}$ state reveals that there is a significant energy barrier for dissociation when the SO_2 is in a bent conformation. The energy barrier is lowered to the observed onset of photodissociation when the calculations include spin-orbit coupling and a nonconfined geometry of the SO_2. The $\tilde{C}$-state of SO_2 remains a complex surface of interest for both theory and experiments, especially as the excitation energies increase.

Chapter 5: Probing New IR Spectral Lines of N_2O (00^01-00^00) Excited in a Tunable Optical Centrifuge: J=100-200

5.1 Introduction

A tunable optical centrifuge has been coupled with a high-resolution transient IR absorption spectrometer to investigate the structure and dynamics of molecules with extreme amounts of rotational angular momentum. The optical centrifuge uses two chirped ultrafast laser pulses to trap and angular accelerate molecules into high rotational states.[24] The transient IR absorption spectrometer is used to measure the appearance and decay of the rotationally excited molecules. The extent of rotational excitation imparted to the molecules by the optical centrifuge depends on the spectral bandwidth of the ultrafast laser pulses. In some cases, centrifuged molecules are prepared in rotational states for which no spectral information is available. Hence, knowledge of IR transition frequencies is required. Such is the case with N_2O. Our optical centrifuge has a spectral bandwidth that is capable of rotationally excited N_2O as high as J=380, yet IR transitions have only been reported up to J=100,[98–100] with an exception discussed below.

N_2O is a linear, asymmetric molecule with three IR active modes. It is an important greenhouse gas, plays a role in stratospheric ozone regulation, and contributes to production of NO_x pollutants in the atmosphere. The first rotationally-resolved IR spectrum of N_2O was reported in 1931 by Plyler and Barker.[101] They resolved P- and R-branch transitions for the fundamental ν_3 absorption band near λ=4.5 μm with a spectral resolution of 0.2 cm^{-1}. They reported line spacings near $\Delta\nu$=0.84 cm^{-1},

consistent with a rotational constant of B=0.42 cm^{-1}. The current value if B=0.419011 cm^{-1}. The observed spectral lines were collected at 300 K and included transitions with rotational quantum number up to J=41. Since then, long-path FTIR spectroscopy has been used to extend the number of transitions, first to R74 and P80,[102] then later to R92 and P90.[100] More recently, transitions up to R99 were identified by Yuan et al using full bandwidth optical centrifuge excitation and transitions up to R100 were reported by Ting et al, using an optical frequency comb.[98,103]

At 300 K, 99.9% of N_2O rotational states have $J \leq 56$. To access higher-J IR transitions, it is necessary to move population into higher J states. Traditional spectroscopic methods are limited to small changes in J; the selection rule for absorption is $\Delta J = \pm 1$ and for Raman, $\Delta J = 0, \pm 2$. It is possible to increase temperature to shift the Boltzmann distribution to higher energy levels, but spectral broadening and congestion can interfere with high-resolution measurements. As an example, the emission spectrum from CO_2 in a T=1800 K flame contains transitions up to J=142 but the intensities are relatively weak, and the line positions overlap with lower-J transition frequencies.[21]

Here we use a tunable optical centrifuge to move population selectively to N_2O rotational states with J=100-200 and use transient IR absorption spectroscopy to measure ν_3 R-branch transition frequencies for these states. An optical centrifuge is tuned by reducing the spectral bandwidth of the ultrafast pulses, thereby reducing the extent of rotational excitation imparted to the sample. This work expands on an earlier study from the Mullin group that measured 8 ν_3 R-branch transitions of N_2O with J

between 140 and 205.[99] Two computational models were used as a guide to locate the spectral transitions.

In the first, R-branch transitions were calculated by extrapolating rotational energy levels for the (00^00) and (00^01) vibrational states using the spectroscopic parameters for transitions with J=92 and below. The predicated transitions were very similar to the observed IR transitions between J=140 and 205. The second computational work was reported in 2016 and expanded in 2019 by Tashkun et al.[104,105] They used an effective Hamiltonian with a polyad model to calculate N_2O IR transitions. The effective Hamiltonian uses 138 parameters and accurately models over 37,000 known transitions in over 300 vibrational bands of N_2O. In this paper the IR transition frequencies calculated from the effective Hamiltonian is denoted ν_{Ham}.

This chapter identifies R-branch IR transition frequencies for $N_2O(00^01\text{-}00^00)$ J=100-200 rotational states. A Doppler-broadened line profile method was used to determine the line center frequencies for the IR transitions. The tunable optical centrifuge was used to increase the population of the rotational states. The line center frequencies were compared to both computational methods and the deviations are compared.

5.2 Experimental

The optical centrifuge has been described in detail in Chapter 2 and the key features are described here. The optical centrifuge pulse begins with an ultrafast Ti:Sapphire oscillator, which generates a 40 fs pulse centered at $\lambda = 806$ nm. The pulse is stretched in time from 40 fs to 100 ps in a regenerative amplifier. The temporal stretching also induces a positive chirp. A pulse shaper then splits the pulse into a pair of pulses and a

negative chirp is induced onto one of the pulses. The pair of oppositely chirped pulses is sent through a multi-pass amplifier, which is pumped by an Nd:YAG laser at $\lambda =$ 532 nm. The pulses are amplified to 20 mJ/pulse. The pair of pulses is recombined in space and time with a delay stage and a polarizing beam cube. The recombined pulses are then given opposite circular polarization. This process creates the optical centrifuge pulses that angularly accelerate molecules into high rotational states. A tunable optical centrifuge is realized by removing the short-wavelength component of the positively chirped pulses with an an adjustable beam block. This step limits the extent of angular acceleration of the molecules and thereby releases the centrifuged molecules in a selected range of rotational states.

Individual rotational states of the centrifuged N_2O are measured with transient IR absorption spectroscopy at $\lambda = 4.5\,\mu m$ from a quantum cascade laser (Daylight Solutions). The probe transitions excite the fundamental ν_3 asymmetric stretch of N_2O. The quantum cascade laser has a resolution of $\Delta\nu_{QCL} \leq 0.0002\ cm^{-1}$. The IR beam is controlled via active feedback by a Fabry-Perot etalon and lock-in amplifier to tune over the N_2O transitions, while the wavelength is monitored on a wavemeter (Bristol Instruments) with a resolution of $\Delta\nu_{wm} \leq 0.0003\ cm^{-1}$. Inside the gas cell, the IR beam is overlapped with the optical centrifuge beam 11 times using an IR multipass mirrors. An example transient absorption signal for the N_2O R-branch transition for J=195 is shown in Figure 5.1. Transient absorption signals are smoothed with a Savitzky-Golay filter and then fit to an exponential decay from 300-1000 ns, shown in the Figure 2 inset. The Savitzky-Golay filter smooths the data with the moving average of successive data points.

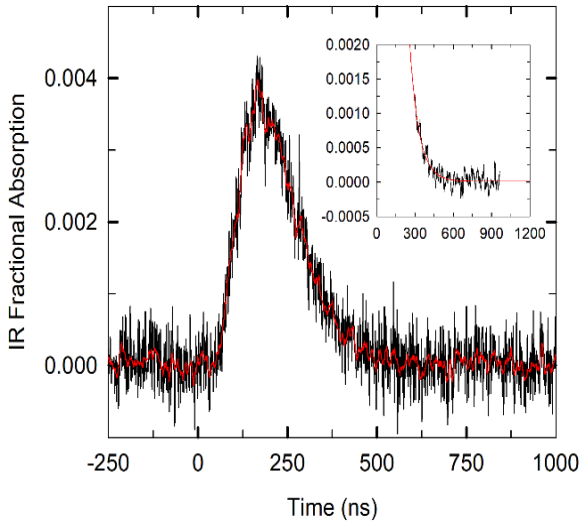

Figure 5.1: Transient signal from optically centrifuged N_2O with J=195. The transient is smoothed using a Savitzky-Golay fit, red line. Inset) The smoothed transient from t=300-1000 ns which was exponentially fit.

The IR transitions for the R-branch of N_2O were reported up to J=92 previously by Toth and are tabulated in the HITRAN database. IR transition frequencies were extrapolated up to J=200 using a third-order polynomial expansion of the rigid rotor model. The B, D, and H constants were determined by fitting the energies of the N_2O (00^00) and (00^01) vibrational states. The optical centrifuge pulses were tuned in order to maximize population in the J=100-200 states.

5.3 Results and Discussion

5.3.1 Spectral Fingerprinting and Enhancement factor of Transient Absorption Signals

A tunable optical centrifuge was used to optimize transient absorption signals in N_2O rotational states with J=100-200. Here we demonstrate this process for the N_2O R190 transition. The classical rotational frequency of a linear molecule is Ω_J. Reducing the intensity of the optical trap at Ω_{OC}=Ω_J enhances the population of molecules in

rotational state J. Figure 5.2a shows the optical traps used for maximizing population in J=190. The full bandwidth optical trap extends to $\Omega_{OC}=8\times10^{13}$ rad s^{-1} and $\Omega_J=3\times10^{13}$ rad s^{-1} for J=190. Sequentially clipping the spectrum of the optrical centrifuge pulses reduces the intensity of the optical trap at Ω_J. Figure 5.2b shows the enhancement of the transient absorption signal for J=190. When the intensity of the trap is $0.68\Omega_{OC}$ the population in J=190 is maximized. The population in J=190 is increased by a factor of four over the full bandwidth.

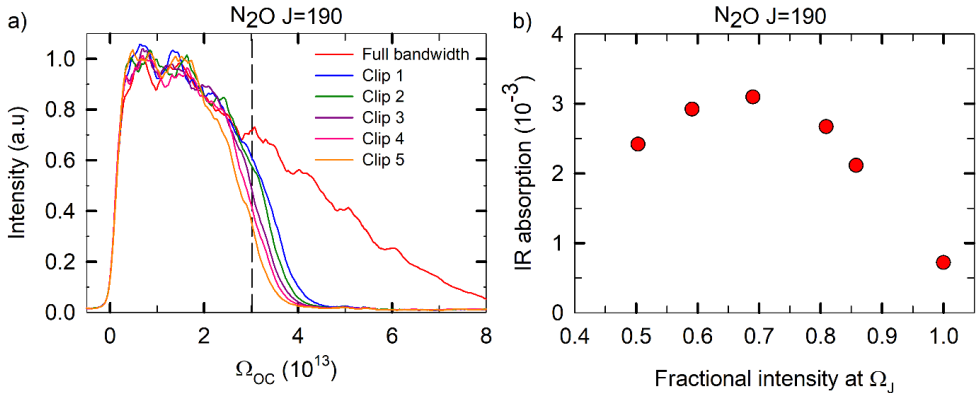

Figure 5.2: a) Optical traps used to maximize population in N_2O J=190. The grey dashed line indicates the corresponding Ω_J of J=190. b) Fractional IR absorption of R190 at linecenter and t=300 ns as a function of fractional trap intensity at Ω_J. The reduced bandwidth trap increases population in J=190 by a factor of 4.

In the ν_3 R-branch IR spectra of N_2O, a bandhead is predicted to be observed around J=116, allowing for fingerprinting of the high rotational states using known IR transitions of lower rotational states. The transitions of R98 and R99 are separated by $\Delta\nu \approx 0.15$ cm^{-1} apart, and between these transitions is predicted to be R134. This small difference in the IR transitions can be tuned over with the Fabry-Perot etalon via a series of voltage-controlled locks. The IR fingerprinting is shown in Figure 5.3 for two different optical traps. The two different optical traps shown in Figure 5.3a and 5.3b

where 5.3a is the full bandwidth and 5.3b is the optimized bandwidth for population in the J=140 rotational state. The fingerprinted region in Figure 5.3c was taken with the full bandwidth trap in 5.3a. The optimized trap in Figure 5.3b was used for the optimized fingerprint in Figure 5.3d. The data points were taken at t=300 ns and at 1.5 Torr of spectroscopic pressure, the time between collisions is approximately 50 ns, so after 300 ns, there have been 6 collisions on average. For J=134, there is an enhancement factor of 3 times when compared to the full clip. An expected increase in transient IR absorption signals for the R98 and R99 transitions is also observed. The lower N_2O rotational states are being populated in two ways: ineffective trapping from the optical centrifuge and collisional relaxation.

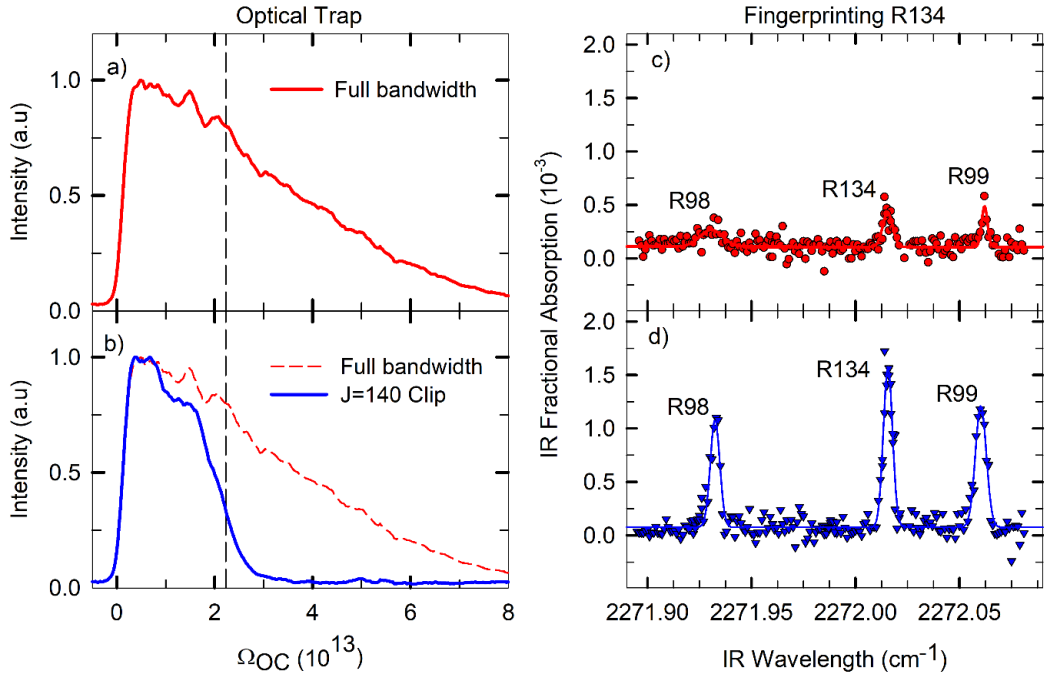

Figure 5.3 Optimizing population for IR transitions of N_2O J=100-200. a) Full bandwidth optical centrifuge trap and b) optical centrifuge trap optimized for J=140. c) Transient IR fingerprinting spectrum at t=300 ns for the N_2O R134 transition located between R98 and R99 using the full bandwidth optical trap. d) Fingerprint spectrum with the optimized optical trap.

5.3.2 IR Transition Frequencies for N_2O ($00^01 \leftarrow 00^00$) R-branch with J=100-200

For each N_2O J-state an line center profile (LCP) was collected where the IR transition was tuned over much like a Doppler profile, however, no baseline was collected. Figure 5.4a shows a full Doppler broadened line profile for N_2O J=140 in the R-branch and Figure 5.4b shows an example of the LCP for the same state. The line center frequency for the full doppler was ν_o=2271.1094±0.0003 cm^{-1} and for the LCP the line center frequency was ν_o=2271.1097±0.0005 cm^{-1}. These frequencies are in good agreement with the reported line center frequency of J=140 which is ν_o=2271.108±0.002 cm^{-1}.[27] The accuracy of these LCP's allowed us to determine the line centers for the states between J=100-200 with a much lower experiment run time versus previous methods.

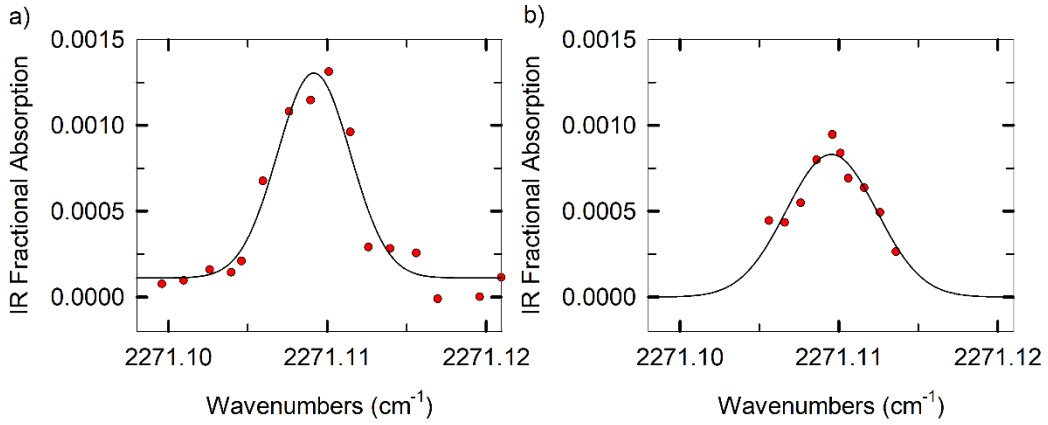

Figure 5.4 a) Full Doppler broadened line profile of N_2O J=140. b) LCP for J=140 that was used to determine the line center of the transition. For both the line center is ν_o=2271.110±0.001 cm^{-1}.

At least one LCP was measured for every rotational state with J=100-200. For a select rotational states three LCPs were collected to determine the reproducibility of the IR transition frequencies. This in the line center frequencies is based on the resolutions of the modulated quantum cascade laser, the wavemeter, and the Gaussian

fits. The error from the modulated QCL is negligible compared to the wavemeter and Gaussian fit. The uncertainty in the wavenumbers is smaller than the data points in Figure 5. The new IR transition frequencies agree well with 9 previously measured N_2O transitions above J=140 and the IR transition frequency for J=100 in the current work is in excellent agreement with the previous reported frequency by Ting et al.[98,99] The LCP line centers measured for these previously found states are in good agreement with the previously published IR transition frequencies. Figure 5.5 shows a fortrat diagram for the R-branch transitions between J=0-200 based on previously reported transition frequencies and those reported here. The states from J=100-200 in Figure 5.5 are transitions reported from this study while the states J=0-99 were reported previously.[98,100]

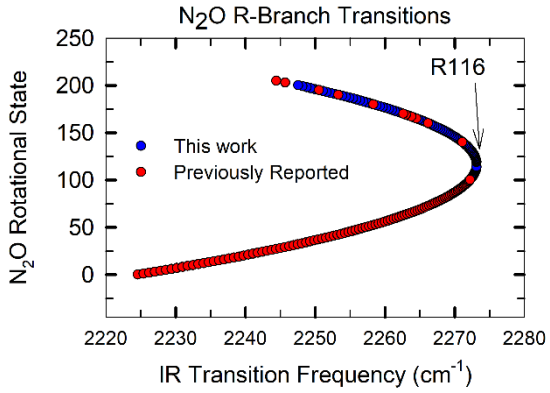

Figure 5.5 N_2O R-branch ($00^01 \leftarrow 00^00$) transition frequencies vs. the rotational states of N_2O between J=0-200. Included in this figure are the previously reported R-branch transition frequencies (red)[98–100,103] and the transition frequencies reported in this paper (blue).

Table 5.1 shows a subset of the observed IR transition frequencies reported in this study. The full list is provided in Appendix B. In Table 5.1 transition frequencies ν_{obs} are reported from this experiment. The calculated transition frequencies ν_{RR} from the rigid rotor expansion and extrapolation. The transition frequencies have also been

calculated using an effective Hamiltonian.[105] These transition frequencies are denoted as ν_{Ham}.

Table 5.1: Representative N_2O R-branch transition frequencies and residuals in units of cm^{-1}.

N_2O J	ν_{obs}	$\Delta\nu_{obs}$	ν_{RR}	$\nu_{H_{eff}}$	$\nu_{obs} - \nu_{RR}$	$\nu_{obs} - \nu_{H_{eff}}$
100	2272.1827	0.0004	2272.1824	2272.1811	-0.0041	0.0017
110	2273.0057	0.0005	2273.0054	2273.0027	0.0003	0.0031
120	2273.1024	0.0005	2273.1015	2273.0964	0.0009	0.0060
130	2272.4712	0.0003	2272.4689	2272.4600	0.0023	0.0112
140	2271.1097	0.0005	2271.1057	2271.0908	0.0038	0.0187
150	2269.0168	0.0003	2269.0106	2268.9868	0.0062	0.0300
160	2266.1916	0.0004	2266.1825	2266.1457	0.0091	0.0459
170	2262.6341	0.0004	2262.6208	2262.5655	0.0133	0.0686
180	2258.3466	0.0005	2258.3251	2258.2443	0.0215	0.1023
190	2253.3274	0.0003	2253.2956	2253.1800	0.0318	0.1474
200	2247.5769	0.0003	2247.5329	2247.3709	0.0439	0.2060

a) ν_{obs} are the transition frequencies reported in this paper.
b) ν_{RR} are the transition frequencies from the extrapolation of the rigid rotor model.
c) ν_{Ham} are transition frequencies from the effective Hamiltonian calculations.[106]

Interestingly, the third-order rigid rotor expansion model, Equation 2.23, predicted the transition frequencies more accurately than the effective Hamiltonian. The rigid rotor expansion predicts the transition frequencies to within 0.05 cm^{-1} at R200. The effective Hamiltonian predicts the transition frequencies to within 0.20 cm^{-1} at R200.

The residuals of the R100-R200 IR transition frequencies are shown in Figure 5.7. For both models the observed transitions frequencies are higher than predicated by the models as the rotational state increases. The B, D, and H constants obtained in the rigid rotor expansion based on R<92, and the H constant may not be well defined for the higher rotational states by the lower rotational states. The effective Hamiltonian accounts for rotation, vibration, and their couplings, any of which could be overestimated. However, these rotational states have been modeled up to 17,000 cm^{-1} within an error of 0.2 cm^{-1} of the found IR transitions, which is remarkably accurate. With this newly provided data, the effective Hamiltonian model could be improved upon. The (00^01) vibrational state could be also coupling to other vibrational states of N_2O at these high rotational states.

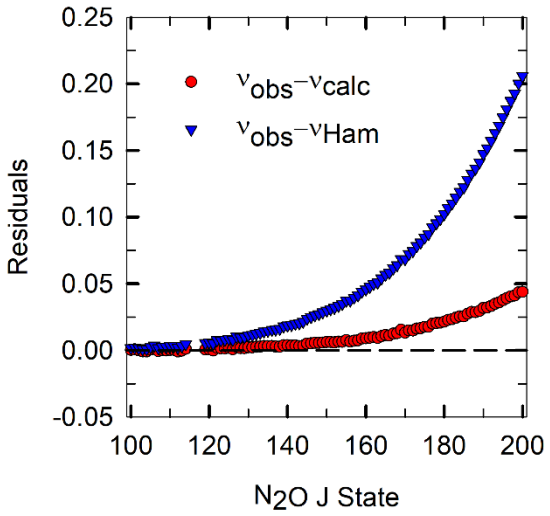

Figure 5.7 Residuals to the observed IR transition frequencies of N_2O J100-200. The third order polynomial expansion provides a better calculation for the IR transitions. Both calculations deviate more at as the J increases.

The tunable optical centrifuge enabled us to selectively populate rotational states without congesting the spectral lines. In the R-branch of N_2O the a bandhead, where

the IR transition frequencies turn around on themselves, is predicated around R116. A bandhead is caused by the upper state having a lower B rotational constant than the lower state. The bandhead in the R-branch is observed at R116 where it was predicated to be. Overlap of the spectral features leads to spectral congestion. Figure 5.6 shows transient absorption signals at t=300 ns as a function of IR frequency, showing transitions with J=112-121. The six rotational states to the left of the bandhead were divided into sets of 2 and fit to a sum of two Gaussians. The double Gaussian fits were used to determine the line center IR transition frequency due to their proximity. The double Gaussian fitting for R121/R112 and R120/R113 was straightforward due to the large enough difference between peaks. The fitting of R119/R114 is a double Gaussian with 2 distinct peaks, however, on the scale of Figure 5.6 the fit appears as a single Gaussian. The appearance of the fit is due to the peaks near overlap and being of similar intensity. The remaining states R115-R118 are not spectrally resolved at 300 K and the line center frequencies are not reported.

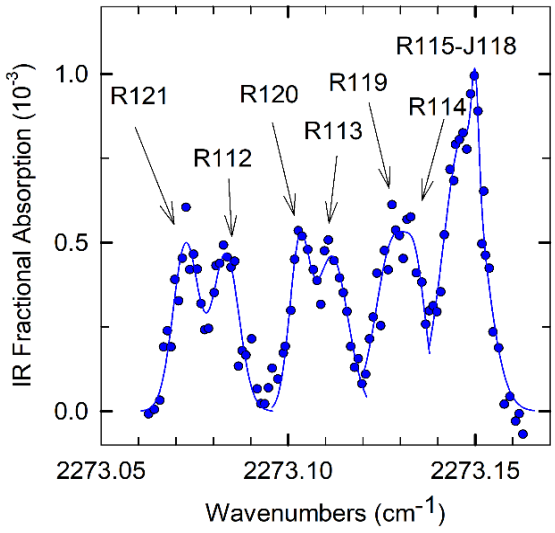

Figure 5.6 N_2O bandhead centered around R115-R118. Double Gaussian fits were used to determine line center frequencies for the 3 blended peaks on the left. Line centers were not determined for R115-118.

5.4 Conclusion

Here, new fundamental ν_3 IR transitions in the R-branch of N_2O have been reported between J=100-200. A bandhead was predicted based on extrapolating available data up to R92 in the HITRAN database. The bandhead was observed at R116 and the rotational states J=115-118 could not be distinguished. By controlling the optical trap with the tunable optical centrifuge, the population in rotational states can be enhanced by a factor of three to four. Overall, an optical centrifuge is a tool that can be used to identify IR transitions of the high rotational states in molecules. The ability to populate specific rotational states by controlling the extent of the optical trap opens the possibility to understand how these molecules in the high rotational states behave in extreme environments.

Chapter 6: State-Resolved Rotational Distributions of N_2O Molecules Using a Tunable Optical Centrifuge

6.1 Introduction

The mechanism by which energy is dissipated from molecules with chemically significant amounts of energy is an active field of research. Most of this work has focused on relaxation pathways for electronic and vibrational energy. Here, using the new IR probe transition frequencies of N_2O reported in Chapter 5, the relaxation dynamics of N_2O molecules in extreme rotational states are studied and compared to other studies on collisional energy transfer of super-rotors.

Rotational energy relaxation is different than vibrational or electronic energy relaxation due to the energy gaps between rotational states. For thermally populated rotational states, the average collision energy k_BT is much larger than the energy gap between the rotational states. As such, rotational relaxation occurs on essentially every collision. A number of state-resolved studies on rotational states with energy gaps similar to k_BT have shown that the most probable relaxation occurs by either resonant or near-resonant energy transfer. This observation is consistent with the energy gap model for collisional energy transfer wherein the most probable rotational energy changes involve the smallest energy gap between collision partners. Collisions that involve large energy gaps are less likely to occur, and when they do occur, the collision partner often gains both rotational and translational energy to conserve energy and angular momentum.

The relaxation dynamics of rotationally excited molecules have been reported for small molecules such as H_2, the hydrogen halides, CO, and CO_2.[107–112] In a system containing H_2 and N_2, the H_2 was excited vibrationally and rotationally to $H_2(\nu=1, J=7)$ using stimulated Raman scattering. The relaxation of the $H_2(\nu=1, J=7)$ state was measured by observing the appearance of $H_2(\nu=1, J=3,5)$ and of $N_2(\nu=1)$. Population gain of $H_2(\nu=1, J=3)$ showed prompt appearance. The energy gap between the $H_2(\nu=1, J=7)$ and the $H_2(\nu=1, J=3)$ rotational state is near 2,300 cm^{-1}, which is close to the energy gap needed to excite N_2 vibrational. For relaxation of the $H_2(\nu=1, J=7)$, the predominant mechanism involves loss of H_2 rotation and gain in N_2 vibration.[108]

Rotation-to-rotation energy transfer also plays an important role in relaxation dynamics of excited molecules. A previous study determined the rotational relaxation rates of rotationally excited $HF(\nu=0, J=13)$ with a number of collision partners. HF was excited into the J=13 rotational state through deactivating collisions with $HF(\nu=0)$ and vibrationally excited $HF(\nu=1)$. When the collision partner is H_2 or D_2, the relaxation rate in the rotation-to-translation pathway was 10 times faster than when the collision partner was He. Helium and D_2 have the same collision reduced mass so the enhancement in relaxation rate is attributed to rotation-to-rotation energy transfer of $HF(\nu=0, J=13)$ and D_2. Helium will only gain translational energy as a singular atom when colliding the $HF(\nu=0, J=13)$.[107]

Advances in optical techniques continue to be made, and now extreme rotational states can be prepared with an optical centrifuge.[24] The optical centrifuge enables the study of molecules with much higher rotational states then have been prepared previously using traditional optical methods. The Mullin group used a tunable optical

centrifuge to rotationally excite carbon monoxide (CO) up to J=80.[28] The optically centrifuged molecules have an inverted rotational distribution and the peak of the distribution is found at J=62. The transient fall off of the distribution with J>62 yielded relaxation rate constants that are only 20% of the gas kinetic collision rate.[28] To understand the lower relaxation rates of CO, master equation calculations were performed using extrapolated state-to-state rate constants for rotational states up to J=90.[112] State-to-state rate constants were determined up to J=29 by Phibbs et al. and then extrapolated up to J=90 by fitting a statistical exponential gap model.[113] The master equation model is in qualitative agreement with the observed CO relaxation rate constants but the model values are a factor of 10 higher. The inhibition in the rotational relaxation of optically centrifuged CO is attributed to large amounts of angular momentum, and the orientational anisotropy of the optically centrifuged molecules.[112]

In this chapter, a tunable optical centrifuge with two different optical traps was used to maximize population in N_2O rotational near J=140 and J=160 in order to study the relaxation dynamics of the extreme rotational states. The inverted N_2O rotational distributions are characterized and the orientational anisotropy was measured by polarization-sensitive IR absorption. Doppler-broadened line profiles were measured to determine the extent to which translational energy results from collisions of optically centrifuged N_2O. Finally relaxation rate constants of optically centrifuged N_2O were determined.

6.2 Experimental

A full description of the optical centrifuge was presented in Chapter 2. The key features are described here. A femtosecond laser pulse centered around λ=806 nm with

a bandwidth of $\Delta\lambda$=65 nm is generated using a Ti:sapphire oscillator. The pulse is stretched in time in a regenerative amplifier, inducing a positive chirp. In the pulse shaper, the pulse is spectrally split into two pulses by a knife-edge mirror and the chirp of one of the pulses is reversed to a negative chirp. The pair of pulses are amplified to 20 mJ per pulse in a multi-pass amplifier, combined in a polarizing beam cube, overlapped in time with a delay line, and circularly polarized by a quarter waveplate to form the optical centrifuge. A tunable optical centrifuge is realized by removing the short-wavelength component of one of the pulses to limit the angular acceleration of the optical trap, as has been discussed previously.[114]

6.2.1 IR Detection of N_2O Rotational States

Individual rotational states of the centrifuged N_2O molecules are measured with transient IR absorption spectroscopy using a high-resolution $\lambda = 4.5\,\mu m$ quantum cascade laser. The IR probe transitions excite one quantum of the ν_3 in the asymmetric stretch ($00^0$1-$00^0$0). The IR wavelength is controlled via active feedback with a Fabry-Perot etalon and a lock-in amplifier. The IR wavelength was monitored using a wavemeter and the wavemeter is calibrated with a known CO_2 IR transition. The transmitted IR intensity is collected on a t=300 ns rise time InSb detector as a function of time. Transient absorption signals are collected on a 500 MHz oscilloscope for approximately 100 laser pulses. The IR polarization is controlled by a half waveplate to either be vertical or horizontal, as shown in Chapter 2. By collecting transient absorption signals of both IR polarizations, the orientational anisotropy of the centrifuged N_2O rotational states is determined as a function of time. The pressure of

N_2O in the sample cell was 1.5 Torr spectroscopic pressure, and the time between collisions is near 50 ns.

6.2.2 Controlling the Initial Distribution of Optically Centrifuged N_2O

The IR transitions for $N_2O(00^01\text{-}00^00)$ absorption with J=100-200 were presented in Chapter 5. When using the full bandwidth optical trap, it is estimated that N_2O can be excited to J=380. Here, we focus on N_2O rotational states with known IR probe frequencies. The tunable optical centrifuge limits the rotational excitation of the molecules to a range of rotational states that can be observed. The J=140 and J=160 rotational states were chosen as peak populations so that the entire nascent distribution could be observed. The optical trap was sequentially reduced in angular frequency and the population in selected N_2O rotational states was maximized. The two optical traps used in this study are shown in Figure 6.1, along with the full bandwidth trap. The dashed lines correspond to the classical rotational frequencies of the N_2O J=140 and J=160 rotational states.

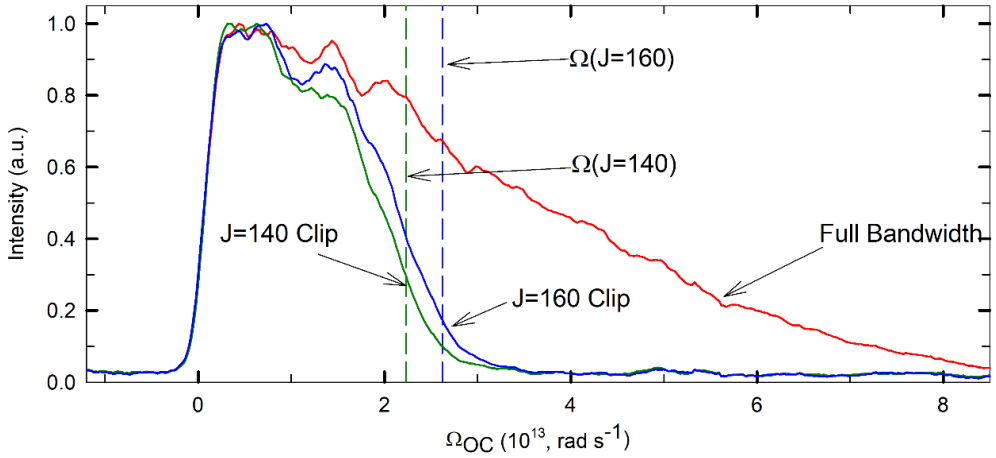

Figure 6.1 The spectral profiles of the optical traps used in this study. The red curve is the full bandwidth trap, while the blue curve is the optical trap used for maximizing population near J=160 and the green curve is the optical trap for maximizing population in J=140. The dashed lines represent the classical rotational frequency of the indicated N_2O rotational states.

6.3 Results and Discussion

Here, we report polarization-sensitive IR spectroscopy used to measure the orientational anisotropy of the inverted distributions of optically centrifuged N_2O when the optical trap is set to maximize the population in selected states. Doppler-broadened line profiles were collected for several rotational states with J in each distribution to determine the extent of translational energy that accompanies the relaxation process. From the distributions, the relaxation dynamics of optically centrifuged N_2O are determined and compared to the relaxation dynamics of optically centrifuged CO.

6.3.1 Nascent Distribution of Optically Centrifuged N_2O

The optical centrifuge creates an inverted rotational distribution of N_2O rotational states. Measuring a range of rotational states showcases the inverted distribution. Transient IR absorption signals for both vertical (s-polarized) and horizontal (p-polarized) IR polarizations were collected to determine the in-plane and out-of-plane rotors. Figure 6.2 shows an s-pol and p-pol transient for N_2O J=100, J=139, and J=151. The data in Figure 6.2 used an optical trap optimized for J=140.

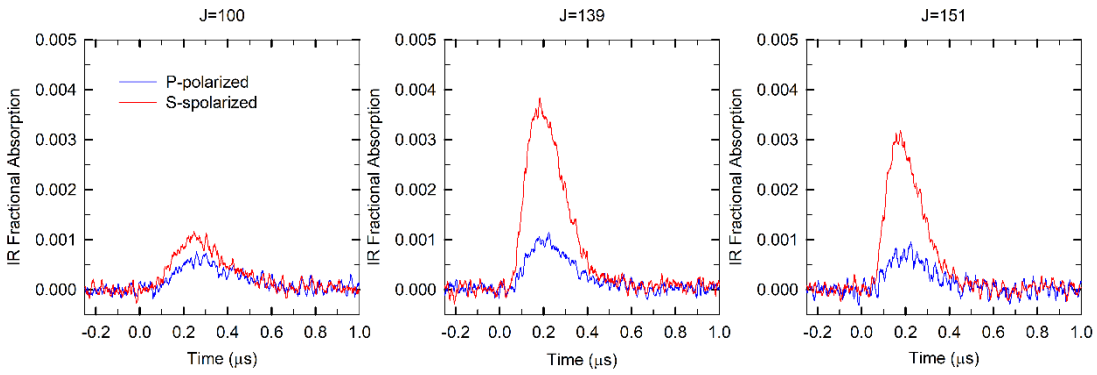

Figure 6.2 S-polarized (red) and p-polarized (blue) transient absorption signal for N_2O with J=100, J=139, and J=151 when the population J=140 rotational state was maximized in the tunable optical centrifuge.

For an N_2O molecule to be considered in-plane, the angular momentum vector of the molecule is aligned to the propagation vector $\vec{z}$ of the optical centrifuge beam. If the N_2O molecule has its angular momentum vector in the $\vec{x}$or $\vec{y}$, the molecule is considered out of plane. A more detailed description and relevant equations are given in section 2.3.5. The orientational anisotropy of the rotational states and its relaxation are calculated by equation 2.28. Orientational anisotropy is a measure of the extent to which the centrifuged molecules are in-plane rotors. The orientational anisotropy for the optically centrifuged N_2O is shown in Figure 6.3.

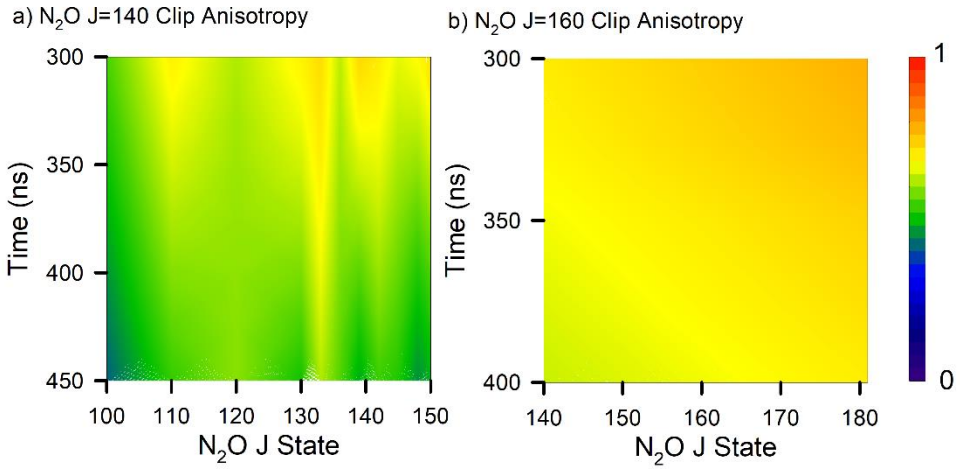

Figure 6.3 The orientational anisotropy of the excited N_2O rotational states. a) For the J=140 clip the orientational anisotropy decreases from r=0.76 to 0.5 as time increases and collisions occur. b) For the J=160 clip, the orientational anisotropy remains relatively flat around r=0.75

At t=300 ns approximately 6 collisions have occurred for the cell pressures in these experiments. For the J=140 clip, the higher-J rotational states have an orientational anisotropy of r=0.76 at 300 ns, and the orientational anisotropy decreases to r=0.55-0.6,The J=100 state has an orientational anisotropy of r=0.55 at 300 ns, and at 450 ns the anisotropy has decreased to r=0.4. If the orientation is isotropic, the anisotropy value is r=0.33. The p-polarized transient absorption signals are essentially gone by

t=450 ns and time-dependent anisotropy values were recorded up to this time point. For the J=160 clip ,the higher-J rotational states have an anisotropy of near r=0.75 at t=300 ns, and remain steady until t=400 ns. After 400 ns, the p-polarized transient IR absorption decreased to zero.

The orientational anisotropy values in Figure 6.3 were used to calculate in-plane transient absorption signals from s-polarized signals, using equation 2.28. Figure 6.4 shows a distribution for each optical trap at t=300 ns. The black line in Figure 6.4 is the angular frequency profile of the optical trap in terms of the N_2O rotational quantum number, scaled to a) J=140 and b) J=160. The populations of the rotational states increase as a function of J until the population is maximized at J=140 and J=160. The rotational state with the maximized population is referred to as J_{max}. The distribution of optically centrifuged molecules shifts to higher J_{max} values for reduced clipping, as the intensity of the optical trap decreases. The population of rotational states with $J > J_{max}$ decreases as the intensity of the optical trap decreases.

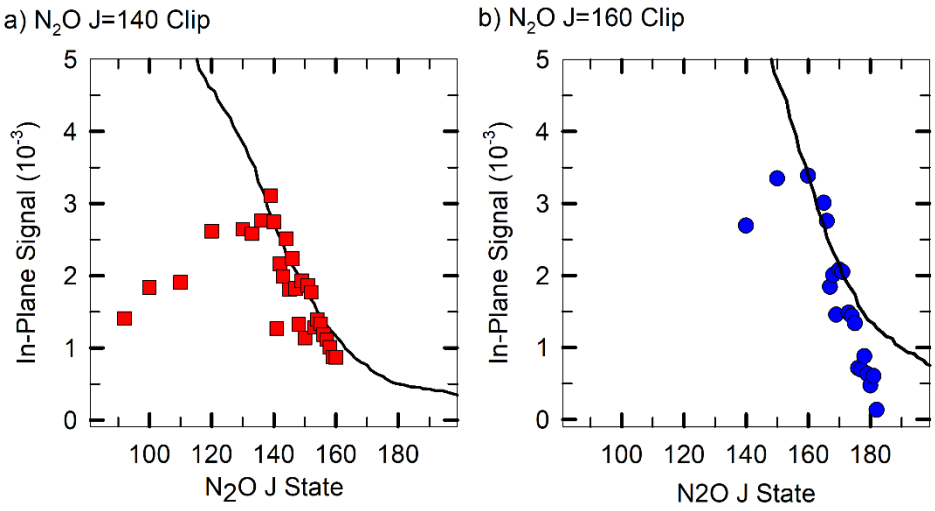

Figure 6.4 Inverted distribution of optically centrifuged N_2O at 300 ns at a pressure of 1.5 Torr. The black line is the optical trap used to obtain this inverted distribution. a) The fractional IR absorption of N_2O increases until the near J=140. b) The fractional IR absorption of N_2O increases until J=160.

6.3.2 Translational Energy of Optically Centrifuged N_2O

The optical centrifuge excites a molecule's rotational energy while leaving the translational energy unchanged. The centrifuged N_2O molecules start from an initial 300K Boltzmann distribution. Transient Doppler-broadened line profiles were measured for 3 rotational states using both optical traps. These rotational states were chosen to be a rotational state below, near, and above J_{max}.

The Doppler line profiles for J=140 clip and their translational temperatures at t=300 ns are shown in Figure 6.5. The spectroscopic pressure was 1.5 mTorr in the gas cell, leading to a collision time of 50 ns per collision. After t=300 ns, on average 6 collisions have occurred. The inverted distribution is clear based on the intensity differences. The Doppler line profiles were fit using Gaussian functions to determine the translational temperatures, based on equation 2.7. The translational temperatures in Figure 6.5 are T_{trans}=776±104 K for J=100, T_{trans}=472±83 K for J=140, and T_{trans}=470±119 K for J=150.

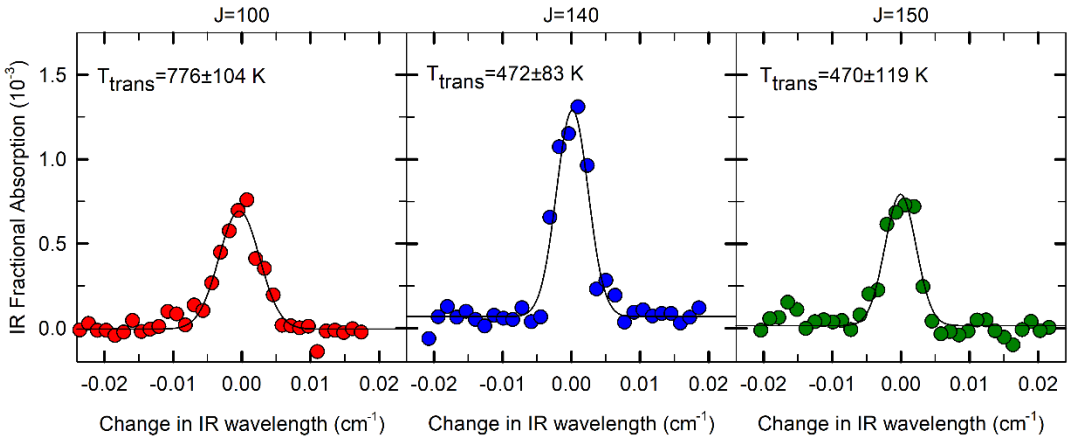

Figure 6.5 Transient Doppler line profiles for the N_2O rotational states J=100, J=140, and J=150 at t=300 ns. The translational temperatures were determined to be T_{trans}=776±104 K for J=100, 472±83 K for J=140, and 470±119 K for J=150.

There is evidence for translational energy gain from collisions of optically centrifuged N_2O. The J=100 state has gained 500 cm^{-1} of translational energy, while the J=140 and 150 states gain only 180 cm^{-1}. This result shows that collisions of optically centrifuged molecules leads to larger recoil velocities for lower rotational states. With six collisions occurring by t=300 ns J=100 gains 83 cm^{-1} over translational energy per collision, while J=140 and J=150 gain only 30 cm^{-1} of translational energy per collision.

The translational temperatures of Figure 6.5 were determined as a function of time and plotted in Figure 6.6. The time evolution for the J=100 state shows that the temperature increases slightly as collisions populate this state. The gain in translational energy comes from the energy mismatch for donor and acceptor states. The population observed in J=100 is from a combination of rotational and translational transfer. The translational temperatures for J=140 remain near T_{trans}=470 K between 300 and 400 ns. A slight increase in translational energy is seen for J=150, but it remains smaller than that for J=100. The combination of smaller orientational anisotropy and larger translational energy is consistent with formation of J=100 through collisions of optically centrifuged molecules. The lower translational energy gains for J=140 and J=150 show that these states result from collisions with smaller energy gap mismatches than the J=100 state.

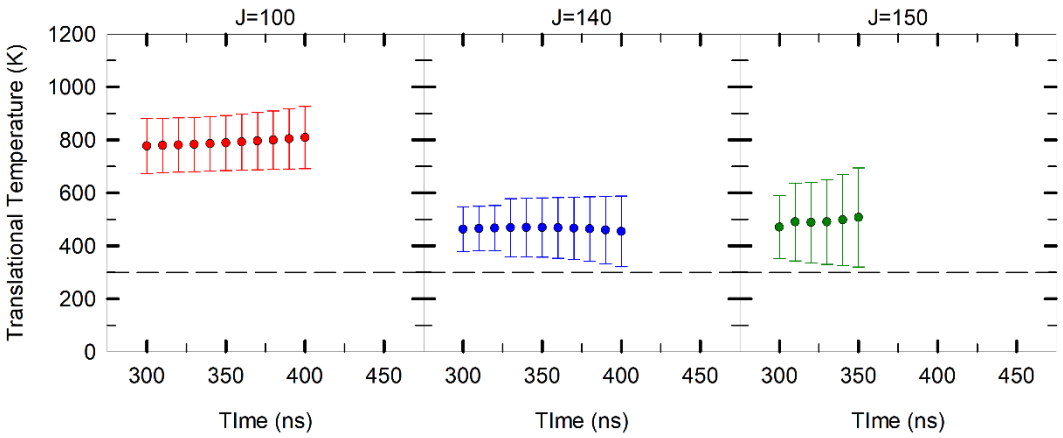

Figure 6.6 Time evolution of translational temperatures for the J=100, J=140, and J=150 rotational states for N_2O. The temperature for J=100 appears to increase showing that these states are being populated by collisions. The translational temperature for J=140 and J=150 remains consistent around 470 K. The translational temperatures are the average of three Doppler line profiles, and the error bars are from the error in the Gaussian fit and the standard deviation the three Doppler profiles.

Doppler-broadened line profiles were also collected for rotational states populated with the J=160 clip. Figure 6.7 shows Doppler-broadened line profilesfor J=140, J=168, and J=170 at t=300 ns. The translational temperatures were determined to be T_{trans}=543±250 K for J=140, T_{trans}=382±94 K for J=168, and T_{trans}=398±214 K for J=175. Again we see that the lowest rotational state of the data set has the largest translational temperature, corresponding to the largest translational energy gain. A comparison of the two data sets shows translational temperatures drop as a function of J, indicating that the probability of inelastic collisions decreases as a molecule's angular momentum increases for the range of states studied here. The lower rotational states gain more translational energy as these rotational states are formed by rotational states with a greater energy mismatch, leading to translational energy in the products of the collision.

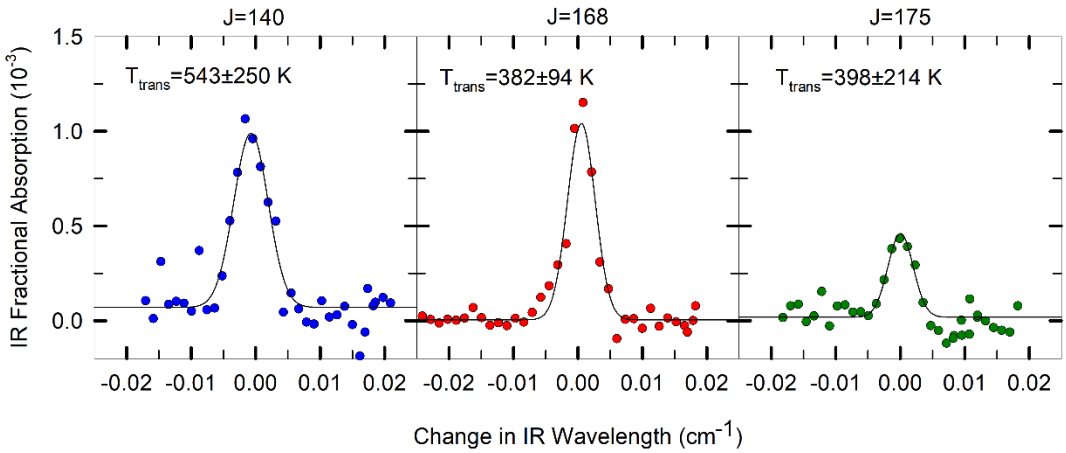

Figure 6.7 Doppler-broadened line profiles for J=140, J=168, and J=175, when the optical trap was maximizing population in J=160. The translational temperatures were determined to be 543±250 K for J=140, 382±94 K for J=168, and 398±214 K for J=175 at t=300 ns.

The time evolution of the translational temperatures for the J=160 clip is shown in Figure 6.8. Similar to the J=140 clip, the time dependence of the translational temperatures shows an increase in the J=140 rotational state and those for J=168 and J=170 remain near 400 K. The increase in translational temperature in J=140 is consistent with J=140 being populated by collisions. The stable translational energy for J=168 and J=175 shows that the relaxing collisions for these optically centrifuged states lead to minimal translational energy gain in the rotational states with higher angular momentum.

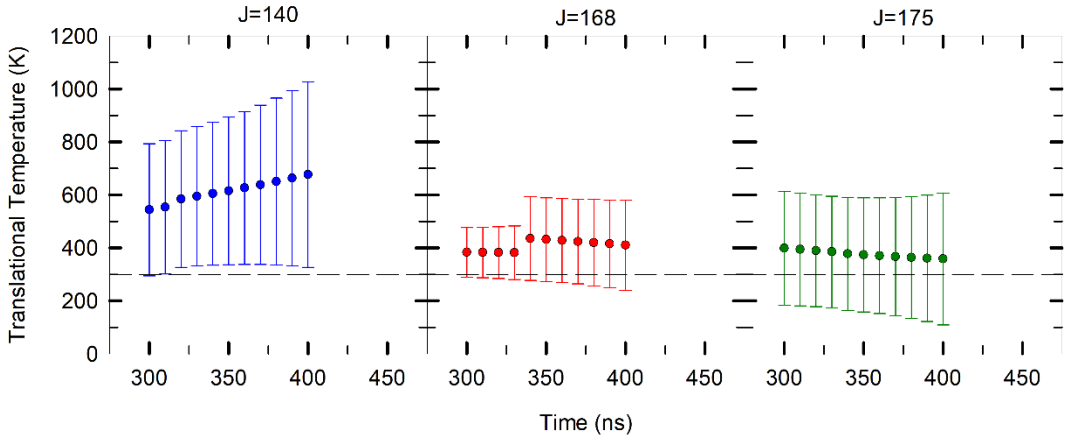

Figure 6.8 Time evolution of the translational temperatures for J=140, J=168, and J=175 when the optical trap was maximizing population near J=165. The translational temperature of J=140 increases with time as collisions populate the rotational state. J=168 and J=175 have relatively flat translational temperatures indicating near resonant energy transfer as the rotational states are collisional relaxed. The translational temperatures are the average of three Doppler line profiles, and the error bars are from the error in the Gaussian fit and the standard deviation the three Doppler profiles.

6.3.3 Relaxation Dynamics and Kinetics of the High-J N_2O Tail

One goal of studying molecules in high-energy states is to understand how they undergo collisional relaxation. The relaxation kinetics were investigated by measuring the time-dependent population loss from rotational states with $J \geq J_{max}$. The high-J tail of both clipped distributions is shown at three time steps in Figure 6.9. Each time slice was fit to a linear function with no constraints. For each distribution, the linear fits have a single intersection point, which represents the maximum rotational state that is populated by the optical trap.

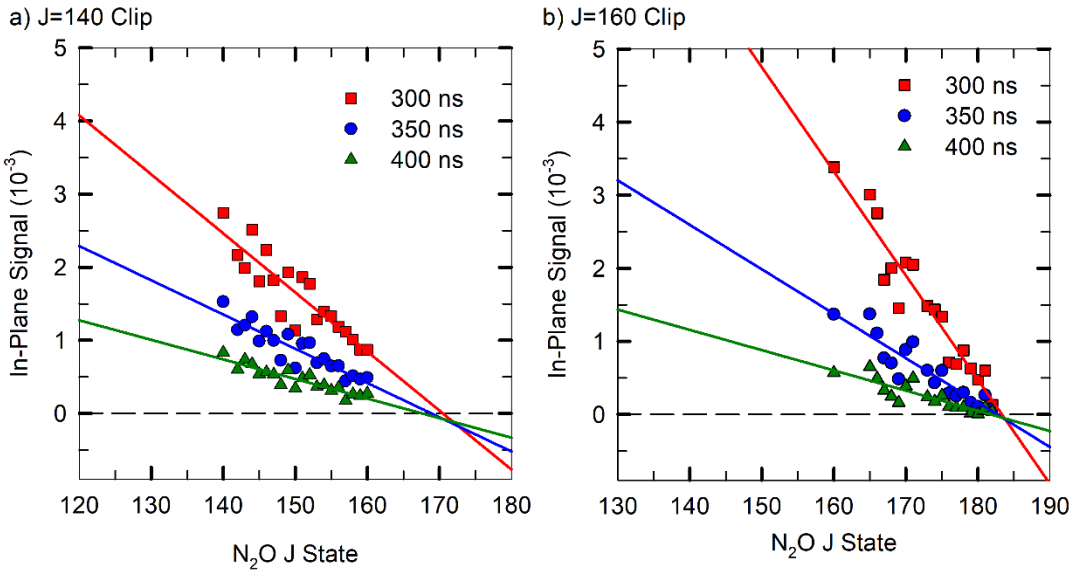

Figure 6.9 a) The high-J tail of the distribution optimized at J=140 at three times after the optical centrifuge pulse. b) The high-J tail of the distributions optimized at J=160. The intersection point of the linear fit represents the highest rotational state that is populated by the optical trap.

The decay rate constants were determined using the linear fit results. Under pseudo-first order conditions, the rate for collisional relaxation of optically centrifuged N_2O is given by Equation 6.1.

$$\frac{d[N_2O(J)]}{dt} = -k_r[N_2O(J)][M] \approx -\gamma[N_2O(J)] \tag{6.1}$$

Here, $[N_2O(J)]$ is the population of N_2O in a specific J rotational state, k_r is the rate constant, and $[M]$ is the population of the non-centrifuged N_2O. It is reasonable to use pseudo first-order kinetics with $[M] \gg [N_2O(J)]$ and defining that $\gamma \equiv k_r[M]$. Integration of Equation 6.1 yields the time-dependence of $[N_2O(J)]$, shown in Equation 6.2.

$$[N_2O(J)]_t = [N_2O(J)]_0\, e^{-\gamma t} \tag{6.2}$$

The ratio of J-specific populations at different times yields Equation 6.3

$$\frac{[N_2O(J)]_{t1}}{[N_2O(J)]_{t2}} = e^{-\gamma(t1-t2)} \tag{6.3}$$

The rate constant is determined by solving for k_r, as shown in Equation 6.4.

$$k_r = ln\left(\frac{[N_2O(J)]_{t1}}{[N_2O(J)]_{t2}}\right)[M]^{-1}(t_2 - t_1)^{-1} \tag{6.4}$$

The relaxation rate constants for the two optical traps are shown in Figure 6.10. Each data point is the average of the three distributions with the error calculated based on the standard deviation.

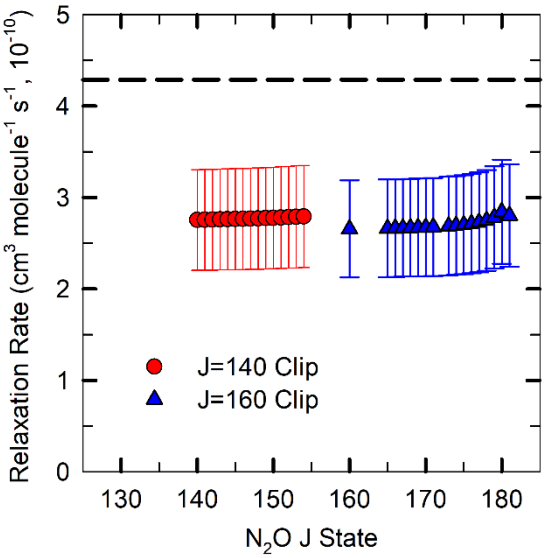

Figure 6.10 The relaxation rate constants for N_2O rotational states in the high-J tail of the optical traps. The dotted line represents the gas kinetic collision rate for N_2O at 1.5 torr. Among the rotational states there is no observed J dependence of the relaxation rate.

The average relaxation rate constant for the J=140 clip is $k_r = 2.8(6) \times 10^{-10}$ cm^3 molecules^{-1} s^{-1}. The average relaxation rate for the J=160 clip is $k_r = 2.8(6) \times 10^{-10}$ cm^3 molecules^{-1} s^{-1}. The gas kinetic collision rate constant, based on the Lennard-Jones parameters for N_2O, is 4.29×10^{-10} cm^3 molecules^{-1} s^{-1}. These data show that the relaxation rate constant for N_2O J=140-180 is about 65% that of the gas kinetic rate

constant. The observed relaxation rate constants reported here are a lower limit since the kinetic model does not include collisions that populate the rotational states.

A difference between the rate constants and the gas kinetic collision rate constant has been observed for collision of CO J=60-80. For CO, the relaxation rate constant was about 20% that of the gas kinetic rate constant.[115] Our data show that molecules in extreme rotational energy states relax slower than do molecules in low rotational states. It is likely the difference in N_2O and CO relaxation rates is related to the energy gaps between states. The energy gaps in CO J=60-80 are near 300 cm^{-1}, whereas the energy gaps in N_2O J=140-180 are near 150 cm^{-1}. N_2O J=140-180 has energy gaps that are below the average collision energy at T=300 K, and its relaxation rates are faster than those for CO.

In collisional energy transfer, both energy and angular momentum must be conserved. The energy gaps in N_2O J=140-180 are 8-10 times higher than the energy gaps in the thermal distribution, so for collisions with $\Delta J=\pm 1$, the bath molecule must increase its angular momentum by $\Delta J=+8$ to +10 if energy remains in rotation. Collisions involving smaller ΔJ for the bath molecules are possible if some energy goes into translational energy. The reduced relaxation rate constants for N_2O can be related to the physics of gyroscopes. When there is a large amount of angular momentum, molecules tend to maintain both their rotational energy and angular momentum longer compared lower energy molecules. This phenomenon is seen in the optically centrifuged N_2O as the oriented angular momentum that persists for the lifetime of the rotational state, leading to slower rotational energy transfer.

6.4 Conclusion

Using a tunable to optical centrifuge, we investigated the relaxation dynamics of N_2O in extreme rotational energy states with J=100-180. The optical trap was tuned to maximize population in either J=140 or J=160 rotational states. The average translational energy of N_2O J=100-175 is dependent on the rotational state J. At the peak of the initial distribution and higher rotational states, the translational temperature was measured to be T_{trans}=470 K for the J=140 clip and T_{trans}=400 K for the J=160 clip, and these values remain relatively flat over a number of collisions. A lower rotational state , J=100, has a translational temperature of T_{trans}=800 K for the J=140 clip and for the J=160 clip the translational temperature of J=140 is T_{trans}=543 K. In both cases, the translational temperature increases with the number of collisions. The orientational anisotropy of the N_2O molecules at the peak of the inverted distributions is r=0.75 at t=300 ns and decreased to r=0.5 by t=450 ns for the J=140 clip. Data for the J=160 clip yield r=0.75 and this value persists for the lifetime of the rotational states. As the excited N_2O relaxes via collisions, the angular momentum projections do not fully relax before the population has decayed out of the rotational state. The relaxation rate constant of the centrifuged N_2O J=140-180 is roughly 65% of the predicated gas kinetic rate constant. This observation is consistent with results for centrifuged CO, which has a relaxation rate of 20% the predicated gas kinetic rate constant. The faster relaxation of N_2O J=140-180 is mainly a result of smaller energy compared to the average collision energy at 300 K.

Chapter 7: Conclusion and Future Projects

The research described in this thesis focused on the energy transfer dynamics of highly excited molecules. The molecules were excited either electronically, vibrationally, or rotationally. The research was performed using high-resolution transient IR spectroscopy as a probe with two different excitation sources, UV photon absorption and an optical centrifuge, as the pump. UV photon absorption was used to excite SO_2 to a metastable electronic state and to vibrationally excite a large aromatic molecule in collidine. The optical centrifuge was used to identify new IR transitions in N_2O and the relaxation dynamics of the rotationally excited N_2O. This thesis focused on the fundamental question of how high-energy molecules are relaxed via chemical processes and deactivating collisions.

In Chapter 3, the collision dynamics of highly vibrationally excited collidine with bath CO_2 were studied to determine the role of state density in collisions. Collidine is the latest in a series of methylated pyridines. The full state distribution of scattered bath CO_2 was collected. Doppler-broadened line profiles of CO_2 appearance show that with increasing rotational state the translational temperature also increases. Doppler-broadened line profiles of CO_2 depletion show that the depletion temperatures are below the 300 K. The colder subset of the Boltzmann distribution is undergoing collisions with the vibrationally excited collidine. Compared to other methylated pyridines, collidine has a similar rotational temperature to lutidine (2,6-dimethylpyridine). The integrated appearance and depletion rate are within error of each other, indicating that the dominant pathway for energy relaxation is the vibration-to-rotation and -translation energy pathway. From the appearance rate and the

rotational temperature, the energy transfer distribution function P(ΔE) is calculated for the collidine-CO_2 system. With $\Delta E > 2500$ cm^{-1} the P(ΔE) distribution has an exponential decay behavior. The same is true for the state density of collidine as the vibrational energy of collidine is decreased. The decay of the P(ΔE) and the state density is correlated by the GRETCHEN model, which has shown a linear dependence on the slopes thus far. Collidine is no different and fits the model, even with one of the highest state densities studied to date. This further confirmation of the GRETCHEN model can lead to predictive compatibility of the P(ΔE) distribution regarding other possible energy donor molecules. This thesis focused on donors with a high state density of vibrational states, to further test the GRETCHEN model and to determine the full role of state density in deactivating collisions, donor molecules with much lower vibrational state density could be studied. If the vibrational state density is below 10^7 states per cm^{-1} and not in a quasi-continuum, will the linear relationship between the P(ΔE) distribution and the vibrational state density decay still hold? For these studies, molecules would have to be vibrationally excited, possibly directly, like $CO_2(03^30)$.

In Chapter 4, the photodissociation dynamics of SO_2 excited to the metastable $\tilde{C}$ electronic state was investigated near the dissociation threshold. A tunable UV pump source was used to excite the SO_2 with differing amounts of energy in the $\tilde{C}$ state and the resulting SO photofragments were probed using the overtone IR transition SO(2←0). Doppler-broadened line profiles on the SO at 5 discrete excitation wavelengths revealed that at certain wavelengths the $SO_2(010)$ vibrational state was the initial state of the SO_2. Nascent rotational distributions show that as the excitation

energy is increased, the rotational temperature of the products also increases. The rotational distributions and the Doppler profiles provided both the total amount of energy and the partition of that energy going into the rotational energy of the dissociation products. Conservation of energy showed that translational energy was preferred in a 4:1 ratio over rotational energy at each of the excitation wavelengths. The preference for translational energy is consistent with a linear transition state before photodissociation. Calculations by theoretical collaborators and experimental results indicate that the dissociation mechanism for SO_2 is the $\tilde{C}$ state coupling to a repulsive triplet state that lowers the energy barrier, but that also the SO_2 goes from a bent geometry to a linear geometry as well.

In Chapter 5 an optical centrifuge was used to rotationally excite N_2O molecules into extreme rotational states to identify their IR transitions. The optical centrifuge was tuned by limiting the optical trap to selectively populate N_2O rotational states between J=100-200, and a QCL was used to probe the R-branch of the $N_2O(00^01\text{-}00^00)$ IR transitions. Line center profiles were collected for each N_2O rotational state and fit to a Gaussian to determine the line center frequency of the IR transition. N_2O has a bandhead in the R-branch around J=116, allowing for spectral fingerprinting of high rotational states with known lower rotational states. This study expanded the known R-branch transitions from N_2O J=100 to N_2O J=200 and enables the study of near nascent rotational distributions of optically centrifuged N_2O, which was studied in Chapter 6.

In Chapter 6, the a tunable optical centrifuge was used to populate select rotational states. The inverted distributions of N_2O molecules was characterized by Doppler-broadened line profiles, orientational anisotropy measurements, and the relaxation rates

of the rotational distribution. For the J=140 clip the orientational anisotropy at the peak of the inverted distributions is r=0.75 at t=300 ns and decreased to r=0.5 by t=450 ns for the J=140 clip. The J=160 clip yielded and orientational anisotropy of r=0.75 and this value persists for the lifetime of the rotational states. Doppler-broadened line profiles showed that lower rotational states have higher translational energy gains than higher rotational states. The translational temperature of the lower rotational states increases as a function of time showing that population in these rotational states is the product of collisions. The relaxation rate constant for N_2O rotational states between J=140-180 was determined to be 65 % of the gas kinetic collision rate. Previously for CO J=60-80 the relaxation rate constant was 20 % that of the gas kinetic collision rate.

The expansion of the known N_2O IR transitions and the ability to tune the optical centrifuge to control where the near nascent rotational distribution provides exciting possibilities for future experiments. Further expansion of the N_2O IR transitions would require a new IR probe laser that will provide the opportunity to probe N_2O up to J=360. The energy gap between the rotational states in this region of N_2O is 284 cm^{-1}, which is similar to the energy gaps of CO. It would be interesting to characterize a near nascent rotational distribution in this region and determine the relaxation dynamics of rotational states with higher rotational energies. The relaxation rate could be similar to the relaxation rate of CO. With a new IR probe laser, the P-branch N_2O IR transitions could also be probed between J=100-200, this combination difference study would provide details on why the rigid rotor model can predict the IR transition frequencies and determine if the upper state, lower state, or both states are distorted.

Appendix A: Einstein A Coefficients for SO ($0 \leftarrow 2$) Emission

This appendix is based on theoretical calculations performed by Dr. Jacek Klos. The computational approach to determine the Einstein coefficients is based first on ab initio electronic structure calculations of the relevant potential energy curves and dipole moment function for the $X\ ^3\Sigma^-$ground electronic state of the SO molecule. Using the $X\ ^3\Sigma^-$ potential energy curve for SO, we calculated vibrational states and corresponding vibrational wave functions using the Discrete Variable Representation (sinc-DVR) approach.[116] The vibrational state energies, corresponding wave functions, and dipole moments are then used in an analytical formula for Einstein absorption coefficients.

For benchmark and testing purposes, we also determined the potential energy curve and dipole function for the $X\ ^1\Sigma^+$electronic ground state of the CO molecule and the Einstein coefficients for the first few vibrational states. Values of A for CO are available in the HITRAN database for comparison.

A.1 Potential Energy and Permanent Dipole Moment Curves

An explicitly correlated variant of the internally contracted multi-reference configuration interaction method (ic-MRCI-F12) to calculate SO potential energy curves for the few lowest-lying singlet, triplet, and quintet spin states was used.[117,118] The ic-MRCI-F12 method included single and double excitation and the influence of higher excitations was accounted for by employing the Davidson correction.[119] The basis was composed of Dunning's augmented, correlation consistent polarized valence triple-zeta basis sets for S and O atoms,[120,121] optimized for Douglas Kroll Hamiltonian integrals (aug-cc-pVTZ-DK), and suitable for recovering possibly small scalar

relativistic effects on S atom. The auxiliary density fitting basis sets for explicitly correlated MRCI-F12 method were generated based on aug-cc-pVTZ basis sets. The reference wave function for the MRCI method was constructed at the complete active space self-consistent field level (CASSCF)[122,123] for spin-singlet, triplet and quintet states.

The calculations were done on a discrete radial grid of 127 points spanning interatomic distance R from R=2.0 to 26.0 Bohr with a step of 0.1 Bohr. Along the potential energy curves for singlet, triplet, and quintet states, we also have calculated the permanent dipole and transition dipole moment curves between electronic states at the MRCI level of theory.

Similar calculations for the CO$\left(X\ ^1\Sigma^+\right)$ molecule was performed as well to test our Einstein coefficients. All the calculations were performed with MOLPRO 2012 suite of codes. As we are interested mainly in the electronic ground triplet state of the SO molecule, we show in Figure A1a the potential energy curve for the ground state $X\ ^3\Sigma^-$ triplet. This potential energy curve has a stationary point corresponding to the global minimum at R=2.812 Bohr, which agrees well with the 2.799 Bohr value given by Huber et al.[124] The calculated S$\left(\ ^3P\right)$+O$\left(\ ^3P\right)$ dissociation limit is 5.3 eV above the minimum. The first five vibrational states calculated using the DVR approach are indicated in Figure A1 as red solid lines.

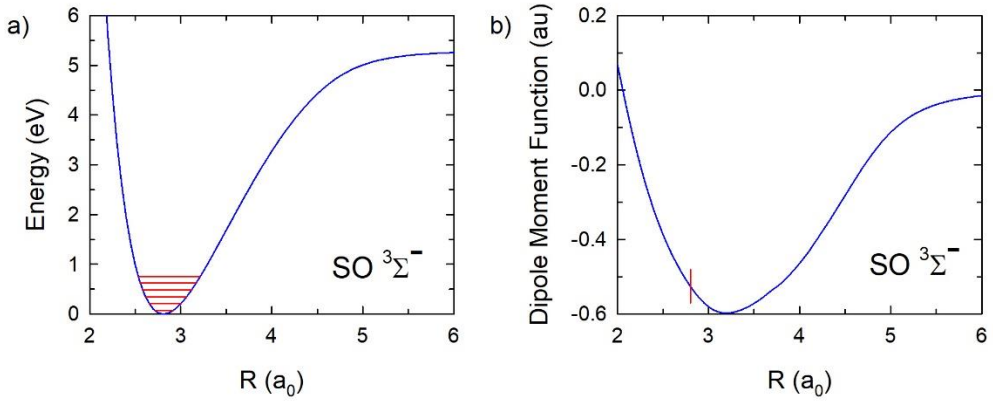

Figure A1: a) Potential energy curve for the SO$\left(X\ ^3\Sigma^-\right)$ determined at the ic-MRCI-F12 level with aug-cc-pVTZ-DK basis. The minimum of the curve is at the equilibrium position of the SO$\left(X\ ^3\Sigma^-\right)$ state near R=2.8 Bohr. The calculated dissociation S(^{3}P) + O(^{3}P) limit has an energy of 5.3 eV (42821 cm^{-1}). The first five vibrational states of the SO molecule (from v=0 to v=4) are indicated by red solid lines. b) Plot of the permanent dipole moment function of the SO$\left(X\ ^3\Sigma^-\right)$ molecule determined with the ic-MRCI-F12 method. The dipole moment at equilibrium geometry is indicated by the red solid line.

The permanent dipole moment curve $\mu(R)$ for the SO$\left(X\ ^3\Sigma^-\right)$ molecule is shown in Figure A1b. The dipole moment was determined at the ic-MRCI-F12 level of theory with the same basis set as described for the potential energy calculations. The short red solid line shows the dipole moment for $R = R_e$ of the SO molecule.

A.2 Calculation of Einstein Coefficients

We set up the vibrational Schrödinger equation with the SO$\left(X\ ^3\Sigma^-\right)$ potential to determine vibrational states and wave functions. We use the sine-DVR approach to solve the resulting Schrödinger equation on a discrete grid of 2500 points spanning interatomic distances R from 2.0 to 14 Bohr. In Table A.1, the first 5 calculated vibrational energies of the SO$\left(X\ ^3\Sigma^-\right)$ molecule along with expectation values of R for each state and the corresponding rotational constant calculated from the expectation value of $1/R^2$ operator are shown.

Table A.1: Vibrational energy states for $^{32}S^{16}O(X\ ^3\Sigma^-)$ molecule and expectation values of R_v and rotational constants B_v.

Vibrational State v	Energy (cm^{-1})	$\langle R_v \rangle$ (Bohr)	$\langle B_v \rangle$ (cm^{-1})
0	566.49	2.8198	0.7115
1	1690.10	2.8366	0.7058
2	2801.20	2.8535	0.7001
3	3899.35	2.8704	0.6944
4	4984.77	2.8876	0.6888

The energy values are in good agreement with experimental values obtained by Clyne and McDermid. The B_0 value is also in good agreement as the reported B_0 is 0.72082 cm^{-1}.[125] In the next step, Einstein coefficients A_{ij} (in S^1) are computed for transitions between level $i = (v', J')$ and $j = (v", J")$ using the following formula that makes use of calculated vibrational wave functions χ_v,[126]

$$A_{ij} = \frac{\left(8\pi h \Delta E_{ij}^3\right) HL}{c^3} B_{ij} \tag{S3}$$

where

$$B_{ij} = \frac{\langle \chi_{v'} | \mu(R) | \chi_{v"} \rangle^2}{(3\epsilon_0 \hbar^2)} \tag{S4}$$

and ΔE_{ij} is the difference between the i-th and j-th rovibrational energy levels defined in equation (S5)

$$\Delta E_{ij} = E(v', N', J') - E(v'', N'', J'') \tag{S5}$$

The rotational energy levels of the $SO(X\ ^3\Sigma^-)$molecule are defined in Hund's case (b) coupling scheme by N and J quantum numbers with J being defined by rotational and spin angular momenta as J=N+S. We used formulas and spectroscopic molecular

parameters given by Burkholder and coworkers for the rotational energies of the $\mathrm{SO}(X\ ^3\Sigma^-)$.[92]

The HL in equation S6 for A_{ij} Einstein coefficient is the so-called Hönl-London factor that depends on the initial J' and final J'' rotational quantum numbers that differ by 1 and is zero otherwise:

$$HL = \begin{cases} \frac{J''}{2J'+1} & for\ J'' - J' = 1 \\ \frac{J''+1}{2J'+1} & for\ J'' - J' = -1 \end{cases} \tag{S6}$$

Figure A2 shows a plot of Einstein coefficients for vibrational transitions of SO involving v=0, 1, 2 states, with A_{ij} coefficients for transitions between rotational states. The Einstein coefficients for SO are approximately an order of magnitude smaller than those for the CO molecule. The calculated coefficients for CO $(0 \leftarrow 2)$ emission are within 10% of the HITRAN values. The calculated Einstein coefficients for the $\mathrm{SO}(X\ ^3\Sigma^-)$ molecule are given in Table SII for the P-branch and Table SIII for the R-branch, along with the lower rotational energies E", transition frequencies ν, and line strengths S.

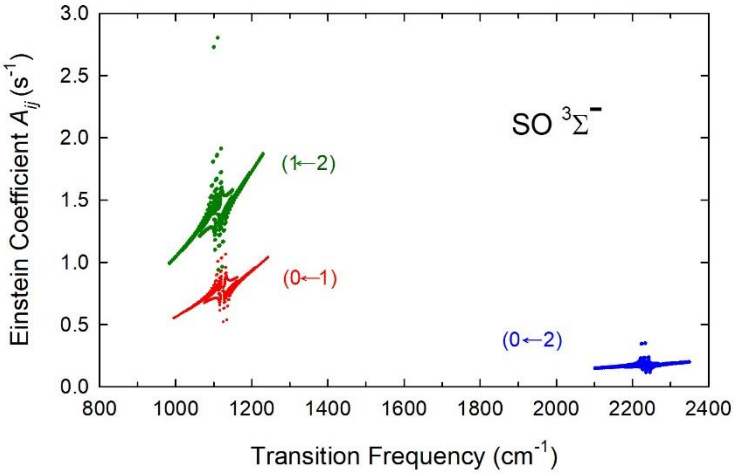

Figure A2 Plot of calculated Einstein coefficients for the rovibrational transitions of SO$\left(X\,^3\Sigma^-\right)$ molecule. Each colored dot represents the Einstein coefficient for an individual $(N',J') \rightarrow (N'',J'')$ rotational transition for the indicated vibrational transitions

A.3 IR Overtone Transitions for SO

IR transition frequencies for SO (v=0) overtone transitions (up to J=31) and spectral fitting parameters were reported previously by Burkholder and coworkers.[13] We used their spectral parameters and analytic expressions to calculate SO (v=0) rotational energies and overtone transition frequencies up to N=39. The calculated transition frequencies have a root mean square deviation from the observed frequencies of 1×10^{-3} cm^{-1} or better. Some error was introduced in the low energy states from using the fitting parameters instead of the observed transitions; in this case, the state energies were established using microwave data.[127,128]

Table A.2. P-branch $(2 \leftarrow 0)$ Overtone Transitions of SO$\left(\,^3\Sigma^-, v=0\right)$: Einstein A Coefficients, Frequencies, and Intensities

v′	J'	N'	v"	J"	N"	A (s^{-1})	E" (cm^{-1})	g'	ν (cm^{-1})	S (10^{-23} cm molecule^{-1})
2	40	39	0	41	40	0.1601	1182.8031	79	2188.2596	1.22
2	38	39	0	39	40	0.1602	1173.0325	79	2188.2771	1.28
2	39	39	0	40	40	0.1601	1177.9267	79	2188.3340	1.25
2	39	38	0	40	39	0.1606	1125.6589	77	2190.5678	1.58
2	37	38	0	38	39	0.1607	1115.8851	77	2190.5860	1.65
2	38	38	0	39	39	0.1607	1120.7801	77	2190.6426	1.61
2	38	37	0	39	38	0.1612	1069.9293	75	2192.8542	2.02
2	36	37	0	37	38	0.1613	1060.1527	75	2192.8729	2.12
2	37	37	0	38	38	0.1612	1065.0482	75	2192.9294	2.07
2	37	36	0	38	37	0.1617	1015.6151	73	2195.1187	2.56
2	35	36	0	36	37	0.1619	1005.8362	73	2195.1380	2.69
2	36	36	0	37	37	0.1618	1010.7321	73	2195.1942	2.63
2	36	35	0	37	36	0.1623	962.7175	71	2197.3612	3.23
2	34	35	0	35	36	0.1624	952.9368	71	2197.3812	3.39
2	35	35	0	36	36	0.1624	957.8328	71	2197.4371	3.31

2	35	34	0	36	35	0.1628	911.2374	69	2199.5817	4.04
2	33	34	0	34	35	0.1630	901.4554	69	2199.6025	4.24
2	34	34	0	35	35	0.1629	906.3513	69	2199.6581	4.14
2	34	33	0	35	34	0.1634	861.1758	67	2201.7802	5.02
2	32	33	0	33	34	0.1636	851.3932	67	2201.8019	5.27
2	33	33	0	34	34	0.1635	856.2886	67	2201.8571	5.14
2	33	32	0	34	33	0.1640	812.5335	65	2203.9566	6.18
2	31	32	0	32	33	0.1641	802.7509	65	2203.9793	6.49
2	32	32	0	33	33	0.1641	807.6456	65	2204.0341	6.33
2	32	31	0	33	32	0.1645	765.3116	63	2206.1110	7.55
2	30	31	0	31	32	0.1647	755.5297	63	2206.1347	7.93
2	31	31	0	32	32	0.1646	760.4233	63	2206.1890	7.74
2	31	30	0	32	31	0.1651	719.5108	61	2208.2432	9.15
2	29	30	0	30	31	0.1653	709.7305	61	2208.2680	9.61
2	30	30	0	31	31	0.1652	714.6225	61	2208.3219	9.38
2	30	29	0	31	30	0.1656	675.1321	59	2210.3533	11.01
2	28	29	0	29	30	0.1658	665.3541	59	2210.3794	11.56
2	29	29	0	30	30	0.1657	670.2442	59	2210.4327	11.28
2	29	28	0	30	29	0.1662	632.1761	57	2212.4413	13.13
2	27	28	0	28	29	0.1664	622.4014	57	2212.4687	13.79
2	28	28	0	29	29	0.1663	627.2892	57	2212.5214	13.46
2	28	27	0	29	28	0.1668	590.6437	55	2214.5070	15.54
2	26	27	0	27	28	0.1670	580.8734	55	2214.5360	16.32
2	27	27	0	28	28	0.1669	585.7582	55	2214.5880	15.93
2	27	26	0	28	27	0.1673	550.5356	53	2216.5504	18.24
2	25	26	0	26	27	0.1676	540.7708	53	2216.5811	19.16
2	26	26	0	27	27	0.1675	545.6521	53	2216.6324	18.69
2	26	25	0	27	26	0.1679	511.8525	51	2218.5716	21.23
2	24	25	0	25	26	0.1682	502.0945	51	2218.6042	22.30
2	25	25	0	26	26	0.1681	506.9716	51	2218.6547	21.76
2	25	24	0	26	25	0.1685	474.5951	49	2220.5705	24.50
2	23	24	0	24	25	0.1688	464.8453	49	2220.6052	25.74
2	24	24	0	25	25	0.1686	469.7175	49	2220.6547	25.11
2	24	23	0	25	24	0.1691	438.7640	47	2222.5469	28.04
2	22	23	0	23	24	0.1694	429.0239	47	2222.5840	29.45
2	23	23	0	24	24	0.1692	433.8905	47	2222.6324	28.74
2	23	22	0	24	23	0.1697	404.3598	45	2224.5010	31.80
2	21	22	0	22	23	0.1700	394.6313	45	2224.5408	33.41
2	22	22	0	23	23	0.1698	399.4913	45	2224.5879	32.60
2	22	21	0	23	22	0.1703	371.3831	43	2226.4326	35.76

2	20	21	0	21	22	0.1706	361.6682	43	2226.4754	37.57
2	21	21	0	22	22	0.1705	366.5204	43	2226.5211	36.65
2	21	20	0	22	21	0.1709	339.8343	41	2228.3416	39.84
2	19	20	0	20	21	0.1713	330.1353	41	2228.3879	41.87
2	20	20	0	21	21	0.1711	334.9786	41	2228.4320	40.84
2	20	19	0	21	20	0.1715	309.7139	39	2230.2281	43.98
2	18	19	0	19	20	0.1720	300.0335	39	2230.2784	46.22
2	19	19	0	20	20	0.1717	304.8664	39	2230.3205	45.08
2	19	18	0	20	19	0.1722	281.0223	37	2232.0919	48.09
2	17	18	0	18	19	0.1727	271.3634	37	2232.1467	50.55
2	18	18	0	19	19	0.1724	276.1844	37	2232.1867	49.30
2	18	17	0	19	18	0.1728	253.7599	35	2233.9330	52.07
2	16	17	0	17	18	0.1734	244.1261	35	2233.9931	54.75
2	17	17	0	18	18	0.1731	248.9332	35	2234.0304	53.39
2	17	16	0	18	17	0.1735	227.9268	33	2235.7512	55.81
2	15	16	0	16	17	0.1741	218.3222	33	2235.8175	58.70
2	16	16	0	17	17	0.1738	223.1132	33	2235.8518	57.24
2	16	15	0	17	16	0.1742	203.5234	31	2237.5465	59.20
2	14	15	0	15	16	0.1749	193.9528	31	2237.6200	62.29
2	15	15	0	16	16	0.1746	198.7249	31	2237.6506	60.72
2	15	14	0	16	15	0.1750	180.5496	29	2239.3187	62.12
2	13	14	0	14	15	0.1758	171.0189	29	2239.4009	65.38
2	14	14	0	15	15	0.1754	175.7689	29	2239.4270	63.72
2	14	13	0	15	14	0.1758	159.0055	27	2241.0676	64.43
2	12	13	0	13	14	0.1767	149.5215	27	2241.1602	67.84
2	13	13	0	14	14	0.1762	154.2455	27	2241.1809	66.11
2	13	12	0	14	13	0.1766	138.8908	25	2242.7930	66.02
2	11	12	0	12	13	0.1777	129.4619	25	2242.8983	69.56
2	12	12	0	13	13	0.1771	134.1552	25	2242.9122	67.76
2	12	11	0	13	12	0.1775	120.2052	23	2244.4946	66.77
2	10	11	0	11	12	0.1788	110.8418	23	2244.6156	70.41
2	11	11	0	12	12	0.1781	115.4983	23	2244.6210	68.56
2	11	10	0	12	11	0.1785	102.9481	21	2246.1721	66.59
2	10	10	0	11	11	0.1792	98.2752	21	2246.3072	68.40
2	9	10	0	10	11	0.1801	93.6632	21	2246.3127	70.30
2	10	9	0	11	10	0.1796	87.1184	19	2247.8248	65.39
2	9	9	0	10	10	0.1805	82.4862	19	2247.9708	67.21
2	8	9	0	9	10	0.1816	77.9285	19	2247.9907	69.13
2	9	8	0	10	9	0.1809	72.7148	17	2249.4520	63.11
2	8	8	0	9	9	0.1820	68.1316	17	2249.6117	64.92

2	7	8	0	8	9	0.1833	63.6414	17	2249.6510	66.86
2	8	7	0	9	8	0.1823	59.7351	15	2251.0525	59.72
2	7	7	0	8	8	0.1837	55.2117	15	2251.2299	61.51
2	6	7	0	7	8	0.1855	50.8068	15	2251.2961	63.45
2	7	6	0	8	7	0.1841	48.1761	13	2252.6246	55.20
2	6	6	0	7	7	0.1859	43.7267	13	2252.8255	56.96
2	5	6	0	6	7	0.1883	39.4321	13	2252.9305	58.93
2	6	5	0	7	6	0.1862	38.0331	11	2254.1657	49.58
2	5	5	0	6	6	0.1887	33.6769	11	2254.3983	51.31
2	4	5	0	5	6	0.1922	29.5290	11	2254.5618	53.34
2	5	4	0	6	5	0.1890	29.2989	9	2255.6714	42.91
2	4	4	0	5	5	0.1926	25.0624	9	2255.9484	44.63
2	3	4	0	4	5	0.1982	21.1167	9	2256.2049	46.80
2	4	3	0	5	4	0.1929	21.9621	7	2257.1343	35.26
2	3	3	0	4	4	0.1985	17.8834	7	2257.4757	37.00
2	2	3	0	3	4	0.2085	14.2296	7	2257.8919	39.56
2	3	2	0	4	3	0.1988	16.0045	5	2258.5424	26.68
2	2	2	0	3	3	0.2088	12.1401	5	2258.9802	28.56
2	1	2	0	2	3	0.2322	8.9342	5	2259.7215	32.24
2	2	1	0	3	2	0.2091	11.3953	3	2259.8753	17.20
2	1	1	0	2	2	0.2325	7.8325	3	2260.4618	19.45
2	1	0	0	2	1	0.2327	8.0829	1	2261.1045	6.48
2	0	1	0	1	2	0.3449	5.3958	3	2262.9209	29.14

Table A.3. R-branch $(2 \leftarrow 0)$ Overtone Transitions of SO$\left({}^3\Sigma^-, v = 0\right)$: Einstein A Coefficients, Transition Frequencies, and Intensities

v	J'	N'	v	J"	N"	A (s^{-1})	E" (cm^{-1})	g'	ν (cm^{-1})	S (10^{-23} cm $molecule^{-1}$)
2	2	1	0	1	0	0.1404	4.9830	3	2265.2869	16.70
2	1	2	0	0	1	0.1184	5.9837	5	2263.6727	11.80
2	2	2	0	1	1	0.1406	4.9607	5	2266.1596	19.78
2	3	2	0	2	1	0.1507	8.0829	5	2266.4639	20.87
2	2	3	0	1	2	0.1407	5.3958	7	2266.7258	27.64
2	3	3	0	2	2	0.1509	7.8325	7	2267.5266	29.27
2	4	3	0	3	2	0.1565	11.3953	7	2267.7012	29.84
2	3	4	0	2	3	0.1510	8.9342	9	2268.3874	37.45
2	4	4	0	3	3	0.1567	12.1401	9	2268.8707	38.24
2	5	4	0	4	3	0.1603	16.0045	9	2268.9658	38.38
2	4	5	0	3	4	0.1569	14.2296	11	2269.8611	46.29

2	5	5	0	4	4	0.1606	17.8834	11	2270.1918	46.51
2	6	5	0	5	4	0.1631	21.9621	11	2270.2367	46.30
2	5	6	0	4	5	0.1608	21.1167	13	2271.2458	54.13
2	6	6	0	5	5	0.1633	25.0624	13	2271.4898	53.92
2	7	6	0	6	5	0.1651	29.2989	13	2271.5019	53.41
2	6	7	0	5	6	0.1636	29.5290	15	2272.5739	60.91
2	8	7	0	7	6	0.1668	38.0331	15	2272.7545	59.59
2	7	7	0	6	6	0.1654	33.6769	15	2272.7647	60.36
2	7	8	0	6	7	0.1657	39.4321	17	2273.8603	66.55
2	9	8	0	8	7	0.1682	48.1761	17	2273.9907	64.73
2	8	8	0	7	7	0.1671	43.7267	17	2274.0165	65.72
2	8	9	0	7	8	0.1673	50.8068	19	2275.1124	70.99
2	10	9	0	9	8	0.1693	59.7351	19	2275.2081	68.78
2	9	9	0	8	8	0.1685	55.2117	19	2275.2452	69.94
2	9	10	0	8	9	0.1687	63.6414	21	2276.3345	74.23
2	11	10	0	10	9	0.1704	72.7148	21	2276.4053	71.70
2	10	10	0	9	9	0.1696	68.1316	21	2276.4508	73.01
2	10	11	0	9	10	0.1699	77.9285	23	2277.5289	76.27
2	12	11	0	11	10	0.1712	87.1184	23	2277.5814	73.51
2	11	11	0	10	10	0.1706	82.4862	23	2277.6331	74.92
2	11	12	0	10	11	0.1709	93.6632	25	2278.6971	77.15
2	13	12	0	12	11	0.1720	102.9481	25	2278.7357	74.23
2	12	12	0	11	11	0.1715	98.2752	25	2278.7922	75.71
2	12	13	0	11	12	0.1717	110.8418	27	2279.8398	76.95
2	14	13	0	13	12	0.1727	120.2052	27	2279.8678	73.93
2	13	13	0	12	12	0.1723	115.4983	27	2279.9281	75.45
2	13	14	0	12	13	0.1725	129.4619	29	2280.9578	75.74
2	15	14	0	14	13	0.1734	138.8908	29	2280.9774	72.70
2	14	14	0	13	13	0.1730	134.1552	29	2281.0407	74.23
2	14	15	0	13	14	0.1732	149.5215	31	2282.0514	73.65
2	16	15	0	15	14	0.1740	159.0055	31	2282.0644	70.62
2	15	15	0	14	14	0.1737	154.2455	31	2282.1300	72.14
2	15	16	0	14	15	0.1739	171.0189	33	2283.1209	70.79
2	17	16	0	16	15	0.1745	180.5496	33	2283.1284	67.84
2	16	16	0	15	15	0.1742	175.7689	33	2283.1960	69.31
2	16	17	0	15	16	0.1745	193.9528	35	2284.1663	67.31
2	18	17	0	17	16	0.1751	203.5234	35	2284.1695	64.45
2	17	17	0	16	16	0.1748	198.7249	35	2284.2387	65.88
2	19	18	0	18	17	0.1755	227.9268	37	2285.1874	60.61
2	17	18	0	16	17	0.1750	218.3222	37	2285.1879	63.32

2	18	18	0	17	17	0.1753	223.1132	37	2285.2579	61.96
2	20	19	0	19	18	0.1760	253.7599	39	2286.1821	56.42
2	18	19	0	17	18	0.1755	244.1261	39	2286.1857	58.97
2	19	19	0	18	18	0.1758	248.9332	39	2286.2538	57.69
2	21	20	0	20	19	0.1764	281.0223	41	2287.1536	52.01
2	19	20	0	18	19	0.1760	271.3634	41	2287.1598	54.39
2	20	20	0	19	19	0.1762	276.1844	41	2287.2262	53.19
2	22	21	0	21	20	0.1768	309.7139	43	2288.1018	47.49
2	20	21	0	19	20	0.1764	300.0335	43	2288.1101	49.68
2	21	21	0	20	20	0.1767	304.8664	43	2288.1751	48.58
2	23	22	0	22	21	0.1772	339.8343	45	2289.0265	42.97
2	21	22	0	20	21	0.1769	330.1353	45	2289.0368	44.96
2	22	22	0	21	21	0.1771	334.9786	45	2289.1006	43.96
2	24	23	0	23	22	0.1776	371.3831	47	2289.9279	38.53
2	22	23	0	21	22	0.1773	361.6682	47	2289.9398	40.33
2	23	23	0	22	22	0.1774	366.5204	47	2290.0025	39.42
2	25	24	0	24	23	0.1779	404.3598	49	2290.8057	34.24
2	23	24	0	22	23	0.1776	394.6313	49	2290.8191	35.85
2	24	24	0	23	23	0.1778	399.4913	49	2290.8809	35.04
2	26	25	0	25	24	0.1783	438.7640	51	2291.6601	30.17
2	24	25	0	23	24	0.1780	429.0239	51	2291.6747	31.59
2	25	25	0	24	24	0.1782	433.8905	51	2291.7358	30.87
2	27	26	0	26	25	0.1786	474.5951	53	2292.4909	26.36
2	25	26	0	24	25	0.1783	464.8453	53	2292.5067	27.60
2	26	26	0	25	25	0.1785	469.7175	53	2292.5670	26.97
2	28	27	0	27	26	0.1789	511.8525	55	2293.2981	22.83
2	26	27	0	25	26	0.1787	502.0945	55	2293.3149	23.91
2	27	27	0	26	26	0.1788	506.9716	55	2293.3746	23.36
2	29	28	0	28	27	0.1792	550.5356	57	2294.0817	19.61
2	27	28	0	26	27	0.1790	540.7708	57	2294.0994	20.54
2	28	28	0	27	27	0.1791	545.6521	57	2294.1585	20.07
2	30	29	0	29	28	0.1795	590.6437	59	2294.8417	16.71
2	28	29	0	27	28	0.1793	580.8734	59	2294.8601	17.50
2	29	29	0	28	28	0.1794	585.7582	59	2294.9188	17.10
2	31	30	0	30	29	0.1797	632.1761	61	2295.5780	14.12
2	29	30	0	28	29	0.1795	622.4014	61	2295.5971	14.79
2	30	30	0	29	29	0.1797	627.2892	61	2295.6553	14.45
2	32	31	0	31	30	0.1800	675.1321	63	2296.2905	11.84
2	30	31	0	29	30	0.1798	665.3541	63	2296.3103	12.40
2	31	31	0	30	30	0.1799	670.2442	63	2296.3681	12.12

2	33	32	0	32	31	0.1802	719.5108	65	2296.9793	9.84
2	31	32	0	30	31	0.1801	709.7305	65	2296.9997	10.31
2	32	32	0	31	31	0.1802	714.6225	65	2297.0571	10.08
2	34	33	0	33	32	0.1805	765.3116	67	2297.6443	8.12
2	32	33	0	31	32	0.1803	755.5297	67	2297.6653	8.51
2	33	33	0	32	32	0.1804	760.4233	67	2297.7224	8.31
2	35	34	0	34	33	0.1807	812.5335	69	2298.2855	6.65
2	33	34	0	32	33	0.1805	802.7509	69	2298.3070	6.97
2	34	34	0	33	33	0.1806	807.6456	69	2298.3638	6.80
2	36	35	0	35	34	0.1809	861.1758	71	2298.9029	5.40
2	34	35	0	33	34	0.1808	851.3932	71	2298.9249	5.66
2	35	35	0	34	34	0.1809	856.2886	71	2298.9813	5.53
2	37	36	0	36	35	0.1811	911.2374	73	2299.4964	4.35
2	38	37	0	37	36	0.1813	962.7175	75	2299.4964	3.48
2	39	38	0	38	37	0.1815	1015.6151	77	2299.4964	2.76
2	35	36	0	34	35	0.1810	901.4554	73	2299.5188	4.56
2	36	36	0	35	35	0.1811	906.3513	73	2299.5750	4.45
2	36	37	0	35	36	0.1812	952.9368	75	2300.0888	3.65
2	37	37	0	36	36	0.1813	957.8328	75	2300.1448	3.56
2	37	38	0	36	37	0.1814	1005.8362	77	2300.6349	2.90
2	38	38	0	37	37	0.1815	1010.7321	77	2300.6906	2.83
2	40	39	0	39	38	0.1817	1069.9293	79	2301.1334	2.18
2	38	39	0	37	38	0.1816	1060.1527	79	2301.1570	2.28
2	39	39	0	38	38	0.1816	1065.0482	79	2301.2125	2.23
2	41	40	0	40	39	0.1819	1125.6589	81	2301.6311	1.70
2	39	40	0	38	39	0.1817	1115.8851	81	2301.6551	1.78
2	40	40	0	39	39	0.1818	1120.7801	81	2301.7104	1.74

Appendix B: N_2O R-branch IR Transition Frequencies

Table B.1: N_2O R-branch IR transitions between J=100-200

N_2O J	ν_{obs}	$\Delta\nu_{obs}$	ν_{RR}	$\nu_{H_{eff}}$	$\nu_{obs} - \nu_{RR}$	$\nu_{obs} - \nu_{H_{eff}}$
100	2272.1827	0.0004	2272.1824	2272.1811	0.0003	0.0017
101	2272.2981	0.0004	2272.2974	2272.2959	0.0007	0.0022
102	2272.4052	0.0004	2272.4051	2272.4035	0.0001	0.0017
103	2272.5047	0.0004	2272.5055	2272.5038	-0.0008	0.0009
104	2272.5978	0.0004	2272.5987	2272.5969	-0.0009	0.0009
105	2272.6852	0.0004	2272.6846	2272.6827	0.0006	0.0025
106	2272.7649	0.0005	2272.7633	2272.7612	0.0016	0.0037
107	2272.8342	0.0004	2272.8347	2272.8325	-0.0005	0.0017
108	2272.8990	0.0003	2272.8989	2272.8965	0.0002	0.0026
109	2272.9558	0.0004	2272.9557	2272.9532	0.0000	0.0026
110	2273.0057	0.0005	2273.0054	2273.0027	0.0003	0.0031
111	2273.0481	0.0004	2273.0477	2273.0448	0.0004	0.0033
112	2273.0819	0.0006	2273.0828	2273.0797	-0.0009	0.0022
113	2273.1104	0.0006	2273.1106	2273.1073	-0.0002	0.0031
114	2273.132	0.005	2273.1312	2273.1276	0.0012	0.0048
115	2273.15	-	2273.1444	2273.1406	-	-
116	Bandhead	-	2273.1504	2273.1464	-	-
117	Bandhead	-	2273.1491	2273.1448	-	-
118	2273.15	-	2273.1405	2273.1360	-	-
119	2273.125	0.005	2273.1247	2273.1198	0.0007	0.0056
120	2273.1024	0.0005	2273.1015	2273.0964	0.0009	0.0060

121	2273.0709	0.0005	2273.0711	2273.0657	-0.0002	0.0052
122	2273.0353	0.0004	2273.0334	2273.0276	0.0020	0.0077
123	2272.9899	0.0004	2272.9883	2272.9823	0.0015	0.0076
124	2272.9376	0.0004	2272.9360	2272.9296	0.0016	0.0080
125	2272.8783	0.0004	2272.8764	2272.8696	0.0018	0.0086
126	2272.8103	0.0004	2272.8095	2272.8023	0.0008	0.0080
127	2272.7380	0.0020	2272.7353	2272.7277	0.0027	0.0103
128	2272.6554	0.0004	2272.6538	2272.6458	0.0016	0.0096
129	2272.5666	0.0004	2272.5650	2272.5565	0.0016	0.0101
130	2272.4712	0.0003	2272.4689	2272.4600	0.0023	0.0112
131	2272.3677	0.0004	2272.3655	2272.3561	0.0022	0.0116
132	2272.2573	0.0006	2272.2547	2272.2448	0.0026	0.0125
133	2272.1395	0.0003	2272.1367	2272.1263	0.0028	0.0132
134	2272.0146	0.0004	2272.0114	2272.0004	0.0032	0.0142
135	2271.8819	0.0003	2271.8787	2271.8671	0.0032	0.0148
136	2271.7420	0.0004	2271.7387	2271.7266	0.0033	0.0154
137	2271.5944	0.0007	2271.5915	2271.5786	0.0029	0.0157
138	2271.4396	0.0004	2271.4369	2271.4234	0.0027	0.0162
139	2271.2788	0.0004	2271.2749	2271.2608	0.0039	0.0180
140	2271.1096	0.0005	2271.1057	2271.0908	0.0038	0.0187
141	2270.9326	0.0004	2270.9292	2270.9135	0.0034	0.0191
142	2270.7489	0.0004	2270.7453	2270.7289	0.0036	0.0200
143	2270.5573	0.0005	2270.5541	2270.5369	0.0032	0.0204

144	2270.3591	0.0004	2270.3556	2270.3375	0.0035	0.0216
145	2270.1547	0.0004	2270.1497	2270.1308	0.0050	0.0239
146	2269.9418	0.0005	2269.9366	2269.9168	0.0052	0.0250
147	2269.7217	0.0004	2269.7161	2269.6953	0.0056	0.0264
148	2269.4938	0.0003	2269.4882	2269.4665	0.0056	0.0273
149	2269.2590	0.0004	2269.2531	2269.2303	0.0059	0.0286
150	2269.0168	0.0003	2269.0106	2268.9868	0.0062	0.0300
151	2268.7670	0.0004	2268.7608	2268.7359	0.0062	0.0311
152	2268.5096	0.0004	2268.5037	2268.4776	0.0059	0.0320
153	2268.2456	0.0004	2268.2392	2268.2120	0.0064	0.0336
154	2267.9738	0.0003	2267.9674	2267.9389	0.0064	0.0349
155	2267.6959	0.0004	2267.6882	2267.6585	0.0077	0.0374
156	2267.4083	0.0003	2267.4018	2267.3707	0.0065	0.0376
157	2267.1152	0.0004	2267.1080	2267.0756	0.0072	0.0396
158	2266.8144	0.0003	2266.8068	2266.7730	0.0076	0.0414
159	2266.5072	0.0004	2266.4983	2266.4631	0.0089	0.0441
160	2266.1916	0.0004	2266.1825	2266.1457	0.0091	0.0459
161	2265.8689	0.0005	2265.8594	2265.8210	0.0095	0.0479
162	2265.5388	0.0005	2265.5289	2265.4889	0.0099	0.0499
163	2265.2004	0.0003	2265.1911	2265.1494	0.0093	0.0510
164	2264.8566	0.0004	2264.8459	2264.8025	0.0107	0.0541
165	2264.5049	0.0004	2264.4934	2264.4482	0.0115	0.0567
166	2264.1447	0.0004	2264.1336	2264.0864	0.0111	0.0583

167	2263.7790	0.0005	2263.7664	2263.7173	0.0126	0.0617
168	2263.4048	0.0003	2263.3919	2263.3408	0.0130	0.0640
169	2263.0254	0.0005	2263.0100	2262.9569	0.0154	0.0685
170	2262.6341	0.0004	2262.6208	2262.5655	0.0133	0.0686
171	2262.2392	0.0003	2262.2243	2262.1668	0.0149	0.0724
172	2261.8352	0.0004	2261.8204	2261.7606	0.0148	0.0746
173	2261.4254	0.0003	2261.4091	2261.3471	0.0163	0.0783
174	2261.0072	0.0003	2260.9906	2260.9261	0.0166	0.0811
175	2260.5824	0.0005	2260.5647	2260.4977	0.0177	0.0847
176	2260.1492	0.0004	2260.1314	2260.0618	0.0178	0.0874
177	2259.7109	0.0003	2259.6909	2259.6186	0.0200	0.0923
178	2259.2634	0.0003	2259.2430	2259.1679	0.0204	0.0955
179	2258.8084	0.0004	2258.7877	2258.7098	0.0207	0.0986
180	2258.3466	0.0005	2258.3251	2258.2443	0.0215	0.1023
181	2257.8780	0.0004	2257.8552	2257.7713	0.0228	0.1066
182	2257.4013	0.0003	2257.3779	2257.2909	0.0234	0.1103
183	2256.9177	0.0003	2256.8933	2256.8031	0.0244	0.1146
184	2256.4269	0.0004	2256.4013	2256.3078	0.0256	0.1191
185	2255.9276	0.0003	2255.9020	2255.8051	0.0255	0.1224
186	2255.4229	0.0003	2255.3954	2255.2950	0.0275	0.1279
187	2254.9102	0.0003	2254.8815	2254.7774	0.0287	0.1328
188	2254.3889	0.0004	2254.3602	2254.2524	0.0287	0.1365
189	2253.8612	0.0003	2253.8316	2253.7199	0.0296	0.1413

190	2253.3274	0.0003	2253.2956	2253.1800	0.0318	0.1474
191	2252.7845	0.0003	2252.7523	2252.6327	0.0322	0.1518
192	2252.2350	0.0004	2252.2017	2252.0778	0.0333	0.1572
193	2251.6786	0.0004	2251.6438	2251.5156	0.0348	0.1630
194	2251.1144	0.0004	2251.0785	2250.9459	0.0359	0.1685
195	2250.5436	0.0004	2250.5059	2250.3687	0.0377	0.1749
196	2249.9650	0.0003	2249.9259	2249.7841	0.0391	0.1809
197	2249.3791	0.0004	2249.3387	2249.1920	0.0404	0.1871
198	2248.7852	0.0003	2248.7441	2248.5924	0.0411	0.1928
199	2248.1857	0.0003	2248.1422	2247.9854	0.0435	0.2003
200	2247.5769	0.0003	2247.5329	2247.3709	0.0439	0.2060

Bibliography

1 T. H. Maiman, Stimulated Optical Radiation in Ruby, *Nat.*, **1960**, 187, 493–494.

2 R. E. Smalley, Dynamics of Electronically Excited States, *Ann. Rev. Phys. Chem* **2003**, 34, 129–153.

3 S. M. Beck, D. L. Monts and M. G. Liverman, Intramolecular vibrational redistribution of electronically excited naphthalene, *J. Chem. Phys.*, 1979, **70**, 1062-1063

4 M. J. Robey, I. G. Ross, R. V. Southwood-Jones and S. J. Strickler, A priori calculations on vibronic coupling in the $^1B_{2u}$—^1Ag (3200 Å) and higher transitions of naphthalene, *Chem. Phys.*, **1977**, 23, 207–216.

5 S. M. Beck, D. E. Powers, J. B. Hopkins and R. E. Smalley, Jet-cooled naphthalene. I. Absorption spectra and line profiles, *J. Chem. Phys.*, 2008, **73**, 2019-2028

6 J. H. Callomon, J. E. Parkin and R. Lopez-Delgado, Non-radiative relaxation of the excited Ã $^1B_{2u}$ state of benzene, *Chem. Phys. Lett.*, **1972**, 13, 125–131.

7 R. S. Minns, D. S. N. Parker, T. J. Penfold, G. A. Worth and H. H. Fielding, Competing ultrafast intersystem crossing and internal conversion in the “channel 3” region of benzene, *Phys. Chem. Chem. Phys.*, **2010**, 12, 15607–

15615.
8 M. Sumitani, D. O'Connor, Y. Takagi, N. Nakashima, K. Kamogawa, Y. Udagawa and K. Yoshihara, Fluorescence quantum yields of S_1, benzene in the channel 3 region, *Chem. Phys. Lett.*, **1983**, 97, 508–512.
9 H. Rubahn and K. Bergmann, The Effect of Laser-Induced Vibrational Bond Stretching in Atom-Molecule Collisions, *Annu. Rev. Phys. Chem.*, **1990**, 41, 735–773.
10 E. M. Miller, L. Murat, N. Bennette, M. Hayes and A. S. Mullin, Relaxation dynamics of highly vibrationally excited picoline isomers (E_{vib}=38 300 cm^{-1}) with CO_2: The role of state density in 199impulsive collisions, *J. Phys. Chem. A*, **2006**, 110, 3266–3272.
11 Q. Liu, D. K. Havey, Z. Li and A. S. Mullin, Effects of Alkylation on Deviations from Lennard−Jones Collision Rates for Highly Excited Aromatic Molecules: Collisions of Methylated Pyridines with $HOD^{\dagger}$, *J. Phys. Chem. A*, **2009**, 113, 4387–4396.
12 S. Yong Bae, H. Young Kim, H. Yang and J. Park, Collisional quenching of vibrationally excited methyl-substituted pyrazine and pyridine series by CO_2, *Chem. Phys. Lett.*, **2001**, 341, 483–489.
13 W. M. Gelbart, Photodissociation Dynamics of Polyatomic Molecules, *Annu. Rev. Phys. Chem.*, **1977**, 28, 323–348.
14 H. Gebelein and J. Jortner, On the Relation between Non Adiabatic Unimolecular Reactions and Radiationless Processes, *Theor. chim. Acta*, **1972**, 25, 143–168.
15 R. G. Gilbert and I. G. Ross, Unimolecular reactions as radiationless transitions. Calculation of the rate of decomposition of N_2O, *Aust. J. Chem.*, 1971, **24**, 1541–1565.
16 F. Fiquet-Fayard and P. M. Guyon, Préionisation et prédissociation dans la dissociation des molécules triatomiques par impact électronique, *Mol. Phys.*, **1966**, 11, 17–30.
17 H. Okabe, Fluorescence and Predissociation of Sulfur Dioxide, *J. Am. Chem. Soc.*, **1971**, 93, 7095-7096.
18 M. H. Hui and S. A. Rice, Decay of Fluorescence from Single Vibronic States of SO_2, *Chem. Phys. Lett.*, 1972, **17**, 474–478.
19 T. Ebata, O. Nakazawa and M. Ito, Rovibrational dependences of the predissociation in the $\tilde{C}(^1B_2)$ state of SO_2, *Chem. Phys. Lett.*, **1988**, 143, 31–37.
20 C. J. Xie, B. Jiang, J. Klos, P. Kumar, M. H. Alexander, B. Poirier and H. Guo, Final State Resolved Quantum Predissociation Dynamics of SO_2 $\tilde{C}(^1B_2)$ and Its Isotopomers via a Crossing with a Singlet Repulsive State, *J. Phys. Chem. A*, **2017**, 121, 4930–4938.
21 D. Bailly, C. Camy-Peyret and R. Lanquetin, Temperature Measurement in Flames through CO_2 and CO Emission: New Highly Excited Levels of CO_2, *J. Mol. Spectrosc.*, **1997**, 182, 10–17.
22 C. A. Taatjes and S. R. Leone, Laser double-resonance mesurements of rotational relaxation rates of HF(J=13) with rare gases, *J. Chem. Phys*, **1988**, 89, 302-308.
23 D. L. Thompson, Vibrational-rotational energy transfer in collisions of HF

(v=4, J=20) with rare gases, *J. Chem. Phys*, **1983**, 78, 1763-1766.
24 J. Karczmarek, J. Wright, P. Corkum and M. Ivanov, Optical Centrifuge for Molecules.
25 T. Armon and L. Friedland, Quantum versus classical dynamics in the optical centrifuge, *Phys. Rev. A*, **2017**, 96, 033411-1-033411-7.
26 L. Yuan, C. Toro, M. Bell and A. S. Mullin, Spectroscopy of molecules in very high rotational states using an optical centrifuge, *Faraday Discussions*, **2011**, 150, 101-111
27 H. M. Ogden, T. J. Michael, M. J. Murray and A. S. Mullin, Transient IR ($00^0 1$–$00^0 0$) absorption spectroscopy of optically centrifuged N2O with extreme rotation up to J = 205, *J. Quant. Spectrosc. Radiat. Transf.*,**2020**, 246, 106867-1-106687-7
28 T. J. Michael, H. M. Ogden and A. S. Mullin, State-resolved rotational distributions and collision dynamics of CO molecules made in a tunable optical centrifuge, *J. Chem. Phys*, **2021**, 154, 134307-1-137707-11.
29 C. N. Hinshelwood, On the Theory of Unimolecular Reactions, *Proc. Math. Phys. Eng. Sci.*, **1926**, 113, 230–233.
30 T. Lenzer, K. Luther, J. Troe, R. G. Gilbert and K. F. Lim, Trajectory simulations of collisional energy transfer in highly excited benzene and hexafluorobenzene, *J. Chem. Phys.*, **1998**, 103, 626-641.
31 H. Hippler, J. Troe and H. J. Wendelken, Collisional deactivation of vibrationally highly excited polyatomic molecules. II. Direct observations for excited toluene, *J. Chem. Phys.*, **1983**, 78, 6709–6717.
32 L. D. Brouwer, H. Hippler, L. Lindemann and J. Troe, Measurement of internal energies by hot ultraviolet absorption spectroscopy: spectra of excited azulene molecules, *J. Phys. Chem.*, **1985**, 89, 4608–4612.
33 H. Hippler, L. Lindemann and J. Troe, Collisional energy transfer of vibrationally highly excited molecules. V. UV absorption study of azulene, *J. Chem. Phys.*, **1985**, 83, 3906–3912.
34 R. E. Weston and G. W. Flynn, Relaxation of Molecules with Chemically Significant Amounts of Vibrational Energy: The Dawn of the Quantum State Resolved Era, *Annu. Rev. Phys. Chem.*, **1992**, 43, 559–589.
35 M. Damm, F. Deckert, H. Hippler and J. Troe, Isomerization and collisional deactivation of highly vibrationally excited azulene molecules after UV excitation at 248 and 193 nm, *J. Phys. Chem.*, **1991**, 95, 2005–2009.
36 U. Grigoleit, T. Lenzer, K. Luther, M. Mützel and A. Takahara, Collisional energy transfer of highly vibrationally excited toluene and pyrazine: Transition probabilities and relaxation pathways from KCSI experiments and trajectory calculations, *Phys. Chem. Chem. Phys.*, **2001**, 3, 2191–2202.
37 N. A. West, J. D. Winner, R. D. W. Bowersox and S. W. North, Resolving the energy and temperature dependence of $C_6H_6^*$ collisional relaxation via time-dependent bath temperature measurements, *J. Chem. Phys.*, **2016**, 145, 014308-1-014308-11
38 U. Hold, T. Lenzer, K. Luther, K. Reihs and A. C. Symonds, Collisional energy transfer probabilities of highly excited molecules from kinetically controlled selective ionization (KCSI). I. The KCSI technique: Experimental

approach for the determination of P(E′,E) in the quasicontinuous energy range, *J. Chem. Phys.*, **2000**, 112, 4076-4089.

39 L. A. Miller and J. R. Barker, Collisional deactivation of highly vibrationally excited pyrazine, *J. Chem. Phys.*, **1996**, 105, 1383–1391.

40 M. L. Yerram, J. D. Brenner, K. D. King and J. R. Barker, Collisional deactivation of highly vibrationally excited benzene pumped at 248 nm, *J. Phys. Chem.*, **1990**, 94, 6341–6350.

41 J. A. Johnson, A. M. Duffin, B. J. Hom, K. E. Jackson and E. T. Sevy, Quenching of highly vibrationally excited pyrimidine by collisions with CO_2, *J. Chem. Phys.*, **2008**, 128, 054304-1-054304-13.

42 C. A. Michaels, Z. Lin, A. S. Mullin, H. C. Tapalian and G. W. Flynn, Translational and rotational excitation of the CO2(00^00) vibrationless state in the collisional quenching of highly vibrationally excited perfluorobenzene: Evidence for impulsive collisions accompanied by large energy transfers, *J. Chem. Phys.*, **1997**, 106, 7055–7071.

43 E. T. Sevy, S. M. Rubin, Z. Lin and G. W. Flynn, Translational and rotational excitation of the CO2(00^00) vibrationless state in the collisional quenching of highly vibrationally excited 2-methylpyrazine: Kinetics and dynamics of large energy transfers, *J. Chem. Phys.*, **2000**, 113, 4912-4932.

44 M. C. Wall, A. E. Lemoff and A. S. Mullin, Unraveling the energy dependence in large $\Delta E(V \rightarrow RT)$ energy transfer: Separation of ΔE and probability in the collisional relaxation of highly vibrationally excited pyrazine (E_{vib}=36,000 to 41,000 cm^{-1}) by CO_2, *J. Chem. Phys.*, **1999**, 111, 7373–7382.

45 L. Yuan, J. Du and A. S. Mullin, Energy-dependent dynamics of large- ΔE collisions: Highly vibrationally excited azulene (E=20,390 and 38,580 cm-1) with CO_2, *J. Chem. Phys.*, **2008**, 129, 014303-1-014303-11

46 M. S. Elioff, M. C. Wall, A. S. Lemoff and A. S. Mullin, Observation of an energy threshold for large ΔE collisional relaxation of highly vibrationally excited pyrazine (Evib=31,000-41,000 cm^{-1}) by CO_2, *J. Chem. Phys.*, **1999**, 110, 5578–5588.

47 D. K. Havey, Q. Liu, Z. Li, M. Elioff, M. Fang, J. Neudel and A. S. Mullin, Direct Determination of Collision Rates beyond the Lennard-Jones Model through State-Resolved Measurements of Strong and Weak Collisions, *J. Phys. Chem. A*, **2007**, 111, 2458–2460.

48 D. K. Havey, J. Du, Q. Liu and A. S. Mullin, Full State-Resolved Energy Gain Profiles of CO_2 (J=2−80) from Collisions of Highly Vibrationally Excited Molecules. 1. Relaxation of Pyrazine (E=37,900 cm^{-1})†, *J. Phys. Chem. A*, **2010**, 114, 1569–1580.

49 J. Du, L. Yuan, S. Hsieh, F. Lin and A. S. Mullin, Dynamics of Weak and Strong Collisions: Highly Vibrationally Excited Pyrazine (E=37900 cm^{-1}) with DCl†, *J. Phys. Chem. A*, **2008**, 112, 9396–9404.

50 J. Du, N. A. Sassin, D. K. Havey, K. Hsu and A. S. Mullin, Full State-Resolved Energy Gain Profiles of CO_2 from Collisions with Highly Vibrationally Excited Molecules. II. Energy-Dependent Pyrazine (E=32700 and 37900 cm^{-1}) Relaxation, *J. Phys. Chem. A*, **2013**, 117, 12104–12115.

51 M. S. Elioff, R. L. Sansom and A. S. Mullin, Vibrational Energy Gain in the ν

$_2$ Bending Mode of Water via Collisions with Hot Pyrazine (E_{vib}=37900 cm^{-1}): Insights into the Dynamics of Energy Flow†, *J. Phys. Chem. A*, **2000**, 104, 10304–10311.

52 T. Lenzer, K. Luther, K. Reihs and A. C. Symonds, Collisional energy transfer probabilities of highly excited molecules from kinetically controlled selective ionization (KCSI). II. The collisional relaxation of toluene: P(E′,E) and moments of energy transfer for energies up to 50000 cm−1, *J. Chem. Phys.*, **2000**, 112, 4090-4110.

53 J. Park, S. Y. Bae and J. A. Lee, Collisional quenching of vibrationally excited azabenzenes by unexcited azabenzenes, *Chem. Phys. Lett.*, **1999**, 303, 505–512.

54 J. Park, L. Shum, A. S. Lemoff, K. Werner and A. S. Mullin, Methylation effects in state-resolved quenching of highly vibrationally excited azabenzenes (Evib∼38500 cm−1). II. Collisions with carbon dioxide, *J. Chem. Phys.*, **2002**, 117, 5221-5233.

55 B. Abulimiti, R. Zhu, J. Long, Y. Xu, Y. Liu, A. Y. Ghazal, M. Yang and B. Zhang, Study of ultrafast dynamics of 2-picoline by time-resolved photoelectron imaging, *J. Chem. Phys.*, **2011**, 134, 234301-1-234301-6

56 M.-F. Lin, Y. A. Dyakov, C.-M. Tseng, A. M. Mebel, S. Hsien Lin, Y. T. Lee and C.-K. Ni, Photodissociation dynamics of pyridine, *J. Chem. Phys.*, **2005**, 123, 054309-1.-504309-11

57 V. A. Lobastov, R. Srinivasan, B. M. Goodson, C. Y. Ruan, J. S. Feenstra and A. H. Zewail, Ultrafast Diffraction of Transient Molecular Structures in Radiationless Transitions. *J. Phys. Chem. A*, **2001**, *105*, 11159-11164

58 J. Park, Z. Li, A. S. Lemoff, C. Rossi, M. S. Elioff and A. S. Mullin, Energy-dependent quantum-state-resolved relaxation of highly vibrationally excited pyridine (E_{vib}=36990-40200 cm^{-1}) through collisions with CO_2, *J. Phys. Chem. A*, **2002**, 106, 3642–3650.

59 J. Park, L. Shum, A. S. Lemoff, K. Werner and A. S. Mullin, Methylation effects in state-resolved quenching of highly vibrationally excited azabenzenes (Evib∼38500 cm-1) - II. Collisions with carbon dioxide, *J. Chem. Phys.*, **2002**, 117, 5221–5233.

60 W. Roebke, Gas-phase photolysis of 2-picoline, *J. Phys. Chem.*, **1970**, 74, 4198–4203.

61 R. Srinivasan, J. S. Feenstra, S. T. Park, S. Xu and A. H. Zewail, Dark structures in molecular radiationless transitions determined by ultrafast diffraction, *Science*, **2005**, 307, 558–563.

62 K. Sushida, M. Fujita, T. Takemura and H. Baba, Phosphorescence from pyridine vapor, *J. Chem. Phys.*, **1983**, 78, 588–589.

63 M. Suzuki, M. Fujita, T. Takemura and H. Baba, Phosphorescence Properties of Pyridine and Its Methyl Derivatives in the Vapor Phase, *Bull. Chem. Soc. Jpn.*, **1988**, 61, 3461–3466.

64 C.-M. Tseng, Y. A. Dyakov, C.-L. Huang, A. M. Mebel, S. Hsien Lin, Y. T. Lee and C.-K. Ni, Photoisomerization and Photodissociation of Aniline and 4-Methylpyridine, *J. Am. Chem. Soc.*, **2004**, 126, 8760-8768

65 B. Wang, B. Liu, Y. Wang and L. Wang, Ultrafast dynamics of pyridine in

'channel three' region, *Int. J. Mass Spectrom.*, **2010**, 289, 92–97.
66 I. Yamazaki, K. Sushida and H. Baba, Fluorescence emissions and non-radiative processes in pyridine and its methyl derivatives, *J. Lumin.*, **1979**, 18, 425–428.
67 I. Yamazaki, K. Sushida and H. Baba, Vapor-phase fluorescence emissions of pyridine and its methyl derivatives: Excitation-energy dependence of nonradiative electronic relaxation, *J. Chem. Phys.*, **1979**, 71, 381–387.
68 A. Linhananta and K. F. Lim, Quasiclassical trajectory calculations of collisional energy transfer : the methyl internal rotor in ethane, *Phys. Chem. Chem. Phys.*, **1999**, 1, 3467-3471.
69 B. M. Toselli and J. R. Barker, Excitation of CO_2 by energy transfer from highly vibrationally excited benzene derivatives, *J. Chem. Phys.*, **1998**, 95, 8108-8119.
70 T. Beyer and D. F. Swinehart, Algorithm 448: Number of multiply-restricted partitions, *Commun. ACM*, **1973**, 16, 379-379.
71 J. R. Lyons, Mass-independent fractionation of sulfur isotopes by isotope-selective photodissociation of SO_2, *Geophys. Res. Lett.*, **2007**, 34, L22811-1-L22811-5.
72 J. R. Lyons, Chapter 5 Photolysis of Long-Lived Predissociative Molecules as a Source of Mass-Independent Isotope Fractionation: The Example of SO_2, *Adv. Quantum Chem.*, 2008, 55, 57–74.
73 S. Ono, A. R. Whitehill and J. R. Lyons, Contribution of isotopologue self-shielding to sulfur mass-independent fractionation during sulfur dioxide photolysis, *J. Geophys. Res. Atmos.*, **2013**, 118, 2444–2454.
74 B. Jiang, P. Kumar, J. Klos, M. H. Alexander, B. Poirier and H. Guo, First-principles C band absorption spectra of SO2 and its isotopologues, *J. Chem. Phys.*, **2017**, 146, 154305-1-154305-7.
75 P. Kumar, B. Jiang, H. Guo, J. Kłos, M. H. Alexander and B. Poirier, Photoabsorption Assignments for the $\tilde{C}^1B_2 \leftarrow \tilde{X}^1A_1$ Vibronic Transitions of SO_2, Using New Ab Initio Potential Energy and Transition Dipole Surfaces, *J. Phys. Chem. A*, **2017**, 121, 1012–1021..
76 B. R. Cosofret, S. M. Dylewski and P. L. Houston, Changes in the vibrational population of SO($^3\Sigma^-$) from the photodissociation of SO_2 between 202 and 207 nm, *J. Phys. Chem. A*, **2000**, 104, 10240–10246
77 H. Kanamori, J. E. Butler, K. Kawaguchi, C. Yamada and E. Hirota, Spin polarization in SO photochemically generated from SO_2, *J. Chem. Phys.*, **1985**, 83, 611–615.
78 P. Felder, C. S. Effenhauser, B. M. Haas and J. R. Huber, Photodissociation of sulfur dioxide at 193 nm, *Chem. Phys. Lett.*, **1988**, 148, 417–422.
79 J. Q. Ma, M. J. Wilhelm, J. M. Smith and H. L. Dai, Photolysis (193 nm) of SO2: Nascent Product Energy Distribution Examined through IR Emission, *J. Phys. Chem. A*, **2012**, 116, 166–173.
80 S. Becker, C. Braatz, J. Lindner and E. Tiemann, Investigation of the predissociation of SO_2 - state-selective detection of the SO-fragment and O-fragment, *Chem. Phys.*, **1995**, 196, 275–291.
81 H. Kanamori, J. E. Butler, K. Kawaguchi, C. Yamada and E. Hirota, Infrared

diode-laser kinetic spectroscopy of transient molecules produced by excimer laser photolysis - application to the SO radical, *J. Mol. Spectrosc.*, **1985**, 113, 262–268.

82 Y. L. Huang and R. J. Gordon, The Multiplet State Distribution of $O(^3P_J)$ Produced in the 193 nm Photodissociation of SO_2, *J. Chem. Phys.*, **1990**, 93, 868–869.

83 M. Brouard, R. Cireasa, A. P. Clark, T. J. Preston, C. Vallance, G. C. Groenenboorn and O. S. Vasyutinskii, $O(^3P_J)$ alignment from the photodissociation of SO_2 at 193 nm, *J. Phys. Chem. A*, **2004**, 108, 7965–7976.

84 A. Freedman, S. C. Yang and R. Bersohn, Translational energy distribution of the photofragments of SO_2 at 193 nm, *J. Chem. Phys.*, **1979**, 70, 5313–5314.

85 M. Kawasaki and H. Sato, Photodissociation of molecular-beams of SO_2 at 193 nm, *Chem. Phys. Lett.*, **1987**, 139, 585–588.

86 G. B. Park, J. Jiang, C. A. Saladrigas and R. W. Field, Observation of b_2 symmetry vibrational levels of the SO_2 $\tilde{C}^1B_2$ state: Vibrational level staggering, Coriolis interactions, and rotation-vibration constants, *J. Chem. Phys.*, **2016**, 144, 144311-1-144311-13.

87 J. Jiang, G. B. Park and R. W. Field, The rotation-vibration structure of the SO2 $\tilde{C}^1B_2$ state explained by a new internal coordinate force field, *J. Chem. Phys.*, **2016**, 144, 144312-1144312-20.

88 G. B. Park, C. C. Womack, A. R. Whitehill, J. Jiang, S. Ono and R. W. Field, Millimeter-wave optical double resonance schemes for rapid assignment of perturbed spectra, with applications to the $\tilde{C}^1B_2$ state of SO_2, *J. Chem. Phys.*, **2015**, 142, 144201-1-144201-12.

89 P. C. Ray, M. F. Arendt and L. J. Butler, Resonance emission spectroscopy of predissociating SO_2 $\tilde{C}^1B_2$: Coupling with a repulsive $^1A_1$ state near 200 nm, *J. Chem. Phys.*, **1998**, 109, 5221–5230.

90 R. Schinke, *Photodissociation dynamics : spectroscopy and fragmentation of small polyatomic molecules*, Cambridge University Press, 1993.

91 S. O. Danielache, C. Eskebjerg, M. S. Johnson, Y. Ueno and N. Yoshida, High-precision spectroscopy of ^{32}S, ^{33}S, and ^{34}S sulfur dioxide: Ultraviolet absorption cross sections and isotope effects, *J. Geophys. Res.*, **2008**, 113, D17314-1-D17314-14.

92 J. B. Burkholder, E. R. Lovejoy, P. D. Hammer, C. J. Howard and M. Mizushima, High-resolution infrared Fourier-transform spectroscopy of SO in the $^3\Sigma^-$ and a $^1\Delta$ electronic states, *J. Mol. Spectrosc.*, **1987**, 124, 379–392.

93 C. E. Moore, *CRC series in Evaluated Data in Atomic Physics*, CRC Press, 1993.

94 C. H. Greene and R. N. Zare, Photofragment Alignment and Orientation, *Annu. Rev. Phys. Chem.*, **1982**, 33, 119–150.

95 R. N. Zare and D. R. Herschbach, Doppler line shape of atomic fluorescence excited by molecular photodissociation, *Proc. Ieee*, **1963**, 51, 173-182.

96 J. L. Kinsey, Fourier transform Doppler spectroscopy: A new means of obtaining velocity-angle distributions in scattering experiments, *J. Chem. Phys.*, **1977**, 66, 2560–2565.

97 I. Nadler, D. Mahgerefteh, H. Reisler and C. Wittig, The 266 nm Photolysis of

ICN$^-$ Recoil Velocity Anisotropies And Nascent E,V,R,T Excitations For The CN + I($^2P_{3/2}$) And CN + I($^2P^{1/2}$) Channels, *J. Chem. Phys.*, 1985, **82**, 3885–3893.

98 W.-J. Ting, C.-H. Chang, S.-E. Chen, H.-C. Chen, J.-T. Shy, B. J. Drouin and A. M. Daly, Precision frequency measurement of N_2O transitions near 45 μm and above 150 μm, *J. Opt. Soc. Am. B*, **2014**, 31, 1954-1963.

99 H. M. Ogden, T. J. Michael, M. J. Murray and A. S. Mullin, Transient IR (00^01–00^00) absorption spectroscopy of optically centrifuged N_2O with extreme rotation up to J=205, *J. Quant. Spectrosc. Radiat. Transf.*, 2020, **246**, 106867-1-106867-7

100 R. A. Toth, *Line-frequency measurements and analysis of N 2 0 between 900 and 4700 cm-1*, *Applied* Optics, **1991**, 30, 5289-5319.

101 B. E. K Plyler and E. F. Barker, The Infrared Spectrum and the Molecular Configuration Of N_2O, *Snow, Proc. Roy. Soc*, **1931**, 15, 17088

102 C. Amiot and G. Guelachvili, Extension of the 106 samples Fourier spectrometry to the Indium Antimonide region: Vibration-rotation bands of $^{14}N_2{}^{16}O$: 3.3–5.5 μm region, *J. Mol. Spectrosc.*, **1976**, 59, 171–190.

103 L. Yuan, C. Toro, M. Bell and A. S. Mullin, Spectroscopy of molecules in very high rotational states using an optical centrifuge, *Faraday Discuss.*, **2011**, 150, 101-111.

104 S. A. Tashkun, V. I. Perevalov and N. N. Lavrentieva, NOSD-1000, the high-temperature nitrous oxide spectroscopic databank, *J. Quant. Spectrosc. Radiat. Transf.*, **2016**, 177, 43–48.

105 S. A. Tashkun, Global modeling of the $^{14}N_2{}^{16}O$ line positions within the framework of the non-polyad model of effective Hamiltonian, *J. Quant. Spectrosc. Radiat. Transf.*, **2019**, 231, 88–101.

106 R. J. Hargreaves, I. E. Gordon, L. S. Rothman, S. A. Tashkun, V. I. Perevalov, A. A. Lukashevskaya, S. N. Yurchenko, J. Tennyson and H. S. P. Müller, Spectroscopic line parameters of NO, NO_2, and N_2O for the HITEMP database, *J. Quant. Spectrosc. Radiat. Transf.*, **2019**, 232, 35–53.

107 C. A. Taatjes and S. R. Leone, Laser double-resonance mesurements of rotational relaxation rates of HF(J=13) with rare gases, H_2, and D_2, *J. Chem. Phys.*, **1998**, 89, 302-308.

108 K. Nie, J. Liu, J. Xing and A. Alghazi, Experimental investigations on rotation–vibration energy transfer in H_2–N_2 collisions, *J. Phys. B At. Mol. Opt. Phys.*, 2022, **54**, 235201-1-235201-11.

109 J. Z. Chou, S. A. Hewitt, J. F. Hershberger, B. B. Brady, G. B. Spector, L. Chia and G. W. Flynn, Diode laser probing of the high-frequency vibrational modes of baths of CO_2, N_2O, and CO excited by relaxation of highly excited NO_2, *J. Chem. Phys.*, **1998**, 91, 5392-5401.

110 M. H. Alexander and D. C. Clary, Propensity rules in rotationally inelastic collisions of CO2, *Chem. Phys. Lett.*, **1983**, 98, 319–323.

111 K. Nauta and R. E. Miller, Rotational and vibrational dynamics of CO_2 and N2O in helium nanodroplets, *J. Chem. Phys.*, **2001**, 115, 10254-10260.

112 M. R. Laskowski, T. J. Michael, H. M. Ogden, M. H. Alexander and A. S. Mullin, Rotational energy transfer kinetics of optically centrifuged CO

molecules investigated through transient IR spectroscopy and master equation simulations, *Faraday Discuss.*, **2022**, 238, 87–102.
113 S. P. Phipps, T. C. Smith, G. D. Hager, M. C. Heaven, J. K. McIver and W. G. Rudolph, Investigation of the state-to-state rotational relaxation rate constants for carbon monoxide (CO) using infrared double resonance, *J. Chem. Phys.*, **2002**, 116, 9281-9292.
114 H. Ogden, PhD Dissertation University of Maryland, 2020.
115 T. J. Michael, H. M. Ogden and A. S. Mullin, State-resolved rotational distributions and collision dynamics of CO molecules made in a tunable optical centrifuge, *J. Chem. Phys.*, **2021**, 154, 134307.
116 D. T. Colbert and W. H. Miller, A novel discrete variable representation for quantum mechanical reactive scattering via the S-matrix Kohn method, *J. Chem. Phys*, **1992**, 96, 1982-1991.
117 T. Shiozaki and H. J. Werner, Multireference explicitly correlated F12 theories, *Mol. Phys.*, 2013, **111**, 607–630.
118 T. Shiozaki, G. Knizia and H.-J. Werner, Explicitly correlated multireference configuration interaction: MRCI-F12, *J. Chem. Phys*, **2011**, 134, 034113-1-034113-12.
119 S. R. Langhoff and E. R. Davidson, Configuration interaction calculations on the nitrogen molecule, *Int. J. Quantum Chem.*, **1974**, 8, 61–72.
120 T. H. Dunning, Gaussian basis sets for use in correlated molecular calculations. I. The atoms boron through neon and hydrogen, *J. Chem. Phys.*, **1998**, 90, 1007-1023.
121 D. E. Woon and T. H. Dunning, Gaussian basis sets for use in correlated molecular calculations. III. The atoms aluminum through argon, *J. Chem. Phys.*, **1998**, 98, 1358-1371.
122 P. J. Knowles and H. J. Werner, An efficient second-order MC SCF method for long configuration expansions, *Chem. Phys. Lett.*, **1985**, 115, 259–267.
123 H. J. Werner and P. J. Knowles, A second order multiconfiguration SCF procedure with optimum convergence, *J. Chem. Phys.*, **1998**, 82, 5053-5063.
124 H. K. P., Constants of Diatomic molecules, *Mol. Spectra Mol. Struct.*, **1979**, **4**, 146–291.
125 M. A. A. Clyne and I. S. McDermid, $A^3\Pi$ and $B^3\Sigma^-$ excited states of the SO radical. Part 1.—Laser-induced fluorescence study of the A – X system; excitation spectra and lifetimes, *J. Chem. Soc. Faraday Trans. 2 Mol. Chem. Phys.*, **1979**, 75, 905–922.
126 J. R. Reisel, C. D. Carter and N. M. Laurendeau, Einstein coefficients for rotational lines of the (0, 0) band of the NO $A^2\Sigma^+$-$X^2\pi$ system, *J. Quant. Spectrosc. Radiat. Transf.*, **1992**, 47, 43–54.
127 F. X. Powell and D. R. Lide, Microwave Spectrum of the SO Radical, *J. Chem. Phys.*, **1964**, 41, 1413–1419.
128 T. Amano, E. Hirota and Y. Morino, Microwave Spectrum of the SO Radical. Equilibrium S-O Distance, Electric Quadrupole Coupling Constant and Magnetic Hyperfine Structure Constants, *J. Phys. Soc. Japan*, **1967**, 22, 399–412.